



الجمهورية الجزائرية الديمقراطية الشعبية

Ministry of Higher Education and Scientific Research

Akli Mohand Oulhadj University – Bouira

Faculty of Applied Sciences

DEPARTMENT OF MECHANICAL ENGINEERING



## FINAL YEAR PROJECT

In fulfillment of the academic requirements for the Master's degree

**Major:** Mechanical Engineering    **Specialization:** Energy Engineering

Presented by:

**BOUZIR MOHAMED KAMEL EDDINE**

Project Title:

Analysis of Blade Angle Variations and Their Impact on  
Turbine Efficiency: A Numerical Simulation

Defended on: / 06 / 2025

Before the jury composed of:

Mr. Mahfoud.B

University of Bouira – Chairperson

Mr. Messai.T

University of Bouira – Supervisor

Mr. Moussaoui.M

University of Bouira – Co-Supervisor

Ms. Baghdadi.F

University of Bouira – Examiner

Academic Year: **2024/2025**



## نموذج التصريح الشرفي الخاص بالالتزام بقواعد النزاهة العلمية لإنجاز بحث.

انا الممضي اسفله،

السيد(ة) بوزيوس محمد كمال الدين الصفة: طالب، استاذ، باحث ..... طالب  
الحامل(ة) لبطاقة التعريف الوطنية: ..... 107141652 والصادرة بتاريخ: 2017/12/30  
المسجل(ة) بكلية / معهد ..... العلوم الفيزيائية قسم ..... الهندسة الميكانيكية  
والمكلف(ة) بإنجاز اعمال بحث (مذكرة، التخرج، مذكرة ماستر، مذكرة ماجستير، اطروحة دكتوراه).  
عنوانها: ..... Analysis of blade angle variations and their  
..... impact on turbine efficiency - A numerical simulation  
تحت إشراف الأستاذ(ة): ..... صبيح خارقة وهو/ساوي: محمد  
أصرح بشرفي اني ألتزم بمراعاة المعايير العلمية والمنهجية الاخلاقيات المهنية والنزاهة الاكاديمية المطلوبة  
في انجاز البحث المذكور أعلاه.

التاريخ: 16/06/2025

توقيع المعني(ة)

رأي هيئة مراقبة السرقة العلمية:

النسبة:

% 11

الامضاء:





## DEDICATION

With deep gratitude for the love, strength, and encouragement that have shaped my path. I dedicate this work to:

**My** late grandmother, whose memory continues to inspire me every day.

**My** mother, for her unconditional love, endless patience, and unwavering belief in me.

**A** special soul whose support and kindness never went unnoticed.

**My** siblings, for their constant support and motivation.

**My** dearest friends, whose voices and laughter on late-night Discord calls turned stress into support and loneliness into companionship. Your presence made the journey lighter and the memories sweeter.

**All** those who stood by me in silence or in action — your support has meant everything.





## Acknowledgments

Above all, I am profoundly thankful to **Allah Almighty**, whose boundless mercy, guidance, and blessings have accompanied me at every step of this academic and personal journey. In moments of difficulty, faith gave me strength; in moments of success, it reminded me to remain humble. Without **Allah**, none of this would have been possible.

I wish to express my sincere and heartfelt gratitude to my supervisor, **Dr. Tarek Messai**, for his exceptional mentorship, scientific insight, and constant support throughout the course of this work. His clarity of vision, constructive criticism, and generous availability made a significant difference in the direction and depth of this research. I am especially grateful for the trust he placed in me, which allowed me to grow both as a student and as a researcher.

My deep appreciation also goes to my co-supervisor, **Dr. Mohamed Moussaoui**, whose valuable contributions, sharp expertise, and technical guidance were essential at every phase of this thesis. His thoughtful suggestions and careful review helped refine both my methodology and interpretation, and his support never wavered, even in the most demanding moments of this project.

I also wish to sincerely thank all the professors and staff of the **Department of Mechanical Engineering** for their guidance and dedication throughout my academic journey. Lastly, I would like to acknowledge with deep appreciation **everyone who supported me along this path**. Your support was a silent force that carried me through the long hours and difficult chapters, and for that, I am truly grateful.



## الملخص

تركّز هذه الأطروحة على تعزيز الكفاءة الكلية من المدخل إلى المخرج في توربين غازي محوري، وذلك من خلال إدخال تحسينات هندسية مدروسة وتحليل مفصّل لسلوك الجريان باستخدام أدوات عددية متقدمة. تم وضع الأساس النظري بالاعتماد على مبادئ التوربوماشين والمعاملات اللابعدية الخاصة بالأداء. تم تصميم الشكل الهندسي للتوربين باستخدام برنامج CFturbo، وأُجريت محاكاة الجريان عبر برنامج أنسيس CFX لتحليل تأثير التعديلات المختلفة على الأداء الديناميكي الهوائي. بالتوازي مع ذلك، تم تطوير نموذج تنبؤي باستخدام الشبكات العصبية الاصطناعية ضمن بيئة ماثلاب لتقدير الكفاءة في مجموعة متنوعة من السيناريوهات التصميمية. وقد أظهرت النتائج أن تعديلات معينة على زوايا شفرات الريش تُساهم بفعالية في التحكم في الاضطرابات الجريانية وتعزيز الكفاءة العامة، مما يؤكد أهمية الجمع بين تقنيات المحاكاة العددية والذكاء الاصطناعي في تحسين تصميم التوربينات.

## Tazwart

Tameslayt-a tettwad i usenfu n tzemredt tamettut n turbin gaz i yefka-d seg yidammen, s wahric n tgejdit n tgeryant akked usenqed n tamsaht n udfar s yifecka n tallunt n umyug. Ttazzan aselkim n tyuri s yisefka n tura n turbomachines akked yixeddamen ur n gmawen. Ttwagren tgeryant n turbin s CFturbo, ttwakren tamsaht n udfar s ANSYS CFX ad d-ttzer wayen id-yennes umgarraden yef tzerfa n tmura. Deg waggaz, ttwagren udrig n ANN deg MATLAB ad ihšen tzemredt deg kra n tzerfa. Isedhuden n tikti d-k ad yili kra n tmura n yizzaren n yirisen i yezmer-d ad isefru lmeslay akked tzemredt tamettut, ad d-yerr lheqq n tmerna n CFD d AI i ukellex n usnifel n turbin.

## Abstract

This thesis focuses on improving the total-to-total efficiency of an axial gas turbine through strategic geometric refinements and detailed flow analysis using advanced computational tools. A theoretical foundation is first established, grounded in turbomachinery principles and relevant non-dimensional performance parameters. The turbine geometry was developed using CFturbo, while flow simulations were carried out in ANSYS CFX to evaluate the aerodynamic effects of various design configurations. Simultaneously, a predictive Artificial Neural Network (ANN) model was

constructed in MATLAB to estimate efficiency across a broad design space. The results demonstrate that specific blade angle modifications can effectively control flow irregularities and enhance overall efficiency, highlighting the potential of combining CFD simulations with machine learning for robust turbine optimization.

## **Résumé**

Ce mémoire porte sur l'amélioration de l'efficacité totale d'un turbomoteur axial à gaz grâce à des modifications géométriques stratégiques et une analyse approfondie de l'écoulement en utilisant des outils numériques avancés. Une base théorique a été établie en s'appuyant sur les principes des turbomachines et sur les paramètres de performance adimensionnels pertinents. La géométrie du turbomoteur a été conçue via le logiciel CFturbo, tandis que les simulations d'écoulement ont été réalisées avec ANSYS CFX afin d'évaluer l'impact aérodynamique des différentes configurations. Parallèlement, un modèle prédictif de réseau de neurones artificiels (ANN) a été développé sous MATLAB pour estimer l'efficacité sur un large éventail de scénarios de conception. Les résultats ont révélé que certaines modifications des angles de pales permettent de maîtriser les irrégularités d'écoulement et d'optimiser significativement la performance globale, soulignant ainsi l'intérêt d'associer la simulation numérique à l'intelligence artificielle pour une conception efficace des turbines.

# Tables of contents

Acknowledgments .....	I
Abstract .....	II
Table of contents .....	IV
List of figures .....	X
List of tables .....	XII
Nomenclature .....	XIII
<b>General Introduction</b> .....	<b>1</b>
<b>Chapter I: Introduction to Axial Turbines and Fundamental Turbomachinery</b>	
<b>Concepts</b>	
I. Introduction .....	3
II. Fundamentals of Turbomachinery .....	3
II.1 Definition of turbomachinery .....	3
II.1.1 Classification of Turbomachinery .....	4
III. Axial flow turbines .....	6
IV. Definitions of axial flow turbine components: .....	6
IV.1 Stator .....	6
IV.2 Rotor .....	7
IV.3 Hub .....	7
IV.4 Shroud .....	7
IV.5 Stage structure and reaction .....	8
IV.6 Pressure profile and energy extraction .....	9
IV.7 Aerodynamic design and flow regulation in turbine stages .....	10

V. Blade angles .....	10
V.1 Inlet blade angle ( $\beta\beta1$ ) .....	11
V.2 outlet blade angle ( $\beta\beta2$ ) .....	11
V.3 angle of attack (i) .....	11
V.4 deviation angle $\delta$ .....	11
V.5 flow camber $\Delta\beta$ .....	11
V.6 cascade width (b) .....	11
V.7 inlet and outlet velocities ( <b>W1 and W2</b> ) .....	11
V.8 Mean aerodynamic velocity <b>Wm</b> and mean angle of attack <b>im</b> .....	11
VI. Axial gas turbines.....	12
VI.1 Primary components .....	12
VI.1.1 Compressor.....	12
VI.1.2 Combustion chamber.....	12
VI.1.3 Turbine .....	12
VI.2 Operational mechanism .....	13
VII. Advances in axial turbine technology: a review of past studies and researches.....	14
VIII. conclusion.....	18

## Chapter II: The modeling and analysis of axial turbines

Introduction .....	19
I. Study system Overview .....	19
II. Velocity triangles of axial turbines .....	20
III. Governing equations of turbomachinery .....	23
III.1 Mass-conservation equation: .....	23
III.2 Linear Momentum equations:.....	24
III.3 Energy equation .....	25



III.4	The angular momentum equation .....	28
III.5	Turbine design parameters.....	31
III.6	The flow coefficient.....	31
III.7	The stage loading coefficient.....	32
III.8	The reaction degree .....	32
III.9	Smith chart.....	33
IV.	Thermodynamic recap and Efficiency .....	34
IV.1	Gas properties: .....	35
IV.2	Efficiency formulations .....	36
IV.2.1	Total-to-total efficiency.....	36
IV.3	Entropy .....	38
IV.4	Boundary layers .....	39
V.	Turbulence .....	40
V.1	Historical and theoretical perspectives on turbulence .....	40
V.2	Statistical and structural definitions of turbulence .....	41
V.3	Characteristics of turbulence .....	42
V.4	Turbulence applications.....	42
V.5	Turbulence approaches .....	42
VI.	Reynolds Averaging .....	43
VII.	Favre mass averaging .....	44
VIII.	Averaged equations .....	44
IX.	The Boussinesq Approach.....	45
X.	The closure models .....	45
X.1	Spalart-Allmaras Model .....	45
X.2	Two-equation models .....	46

X.2.1	Standard k-epsilon model.....	46
X.2.2	RNG k-epsilon model.....	47
X.2.3	Realizable K-epsilon model .....	48
X.2.4	Standard k-omega model.....	49
X.2.5	Shear stress transport k-omega model.....	50
XI.	Conclusion:.....	52
V.2	Statistical and structural definitions of turbulence .....	41
V.3	Characteristics of turbulence .....	42
V.4	Turbulence applications.....	42
V.5	Turbulence approaches .....	42
VI.	Reynolds Averaging .....	43
VII.	Favre mass averaging .....	44
VIII.	Averaged equations .....	44
IX.	The Boussinesq Approach.....	45
X.	The closure models .....	45
X.1	Spalart-Allmaras Model .....	45
X.2	Two-equation models .....	46
X.2.1	Standard k-epsilon model.....	46
X.2.2	RNG k-epsilon model.....	47
X.2.3	Realizable K-epsilon model .....	48
X.2.4	Standard k-omega model.....	49
X.2.5	Shear stress transport k-omega model.....	50
XI.	Conclusion:.....	52

### **Chapter III: Numerical Methods and CFD implementation**

I	Introduction.....	53
---	-------------------	----

II	Numerical Discretization Approaches .....	53
III	The fundamentals of mesh generation .....	55
III.1	Types of meshes .....	56
IV	Numerical discretization by finite volume method.....	58
V	ANSYS CFX numerical schemes .....	61
VI	Pressure-velocity coupling in ANSYS CFX.....	63
VII	Solution strategy in CFX.....	64
VII.1	The solution processes.....	65
VII.2	The algebraic multigrid .....	65
VIII	CFturbo software.....	67
VIII.1	Cascade geometry creation .....	67
VIII.2	Meshing.....	72
IX	Artificial Neural Network .....	74
IX.1	Linear combination:.....	75
IX.2	Error Calculation in ANNs .....	76
X	Conclusion .....	77

## **Chapter IV: Results and Discussion**

I	Introduction.....	78
II	CFX parameterization .....	78
III	Grid convergence study .....	80
III.1	Mathematical formulations:.....	81
III.2	Grid study table and GCI results .....	81
IV	Naca-4412 case validation .....	83
IV.1	The setup.....	83
V	Core simulation results and discussion .....	86

VI	Simulation Contours .....	88
VI.1	Temperature evolution.....	89
VI.2	Pressure Contours .....	93
VI.3	Velocity, vortices and Mach contours .....	98
VII	Micro to large turbine scaling .....	101
VII.1	Turbine theoretical scaling .....	103
VIII	Artificial Neural Network Results.....	104
IX	Conclusion .....	111
	<b>General Conclusion .....</b>	<b>112</b>

# List of figures

## Chapter I: Introduction to Axial Turbines and Fundamental Turbomachinery

### Concepts

Figure I.1: cross-sectional view of the parts of a turbomachine. ....	4
Figure I.2: classification of turbomachines based on flow direction. ....	6
Figure I.3: 3D Stator Example generated using CFturbo. ....	6
Figure I.4: A simple 3d representation of a rotor blade. ....	7
Figure I.5: 3D Rotor generated using CFturbo. ....	7
Figure I.6: Hub and Shroud 3D examples generated CFturbo. ....	8
Figure I.7: 2 stage axial turbine design. ....	8
Figure I.8: Full Stage 3D representation using CFturbo. ....	9
Figure I.9: diagram of flow through a passage. ....	10
Figure I.10: general angles of a profile cascade. ....	10
Figure I.11: detailed schematic of a Turbo-reactor. ....	12
Figure I.12: cross-section of an industrial gas turbine. ....	13
Figure I.13: thermodynamic cycles of the Brayton cycle. ....	13
Figure I.14: Snippet example of pressure contours. ....	14
Figure I.15: Snippet example of pressure contours. ....	15
Figure I.16: snippet example of Mach contours. ....	15
Figure I.17: Static pressure distribution ....	16
Figure I.18: Original (left) and optimized (right) turbine Stator. ....	17
Figure I.19: turbine performance as a function of pressure-ratio. ....	18
Figure I.20: Flow streamlines. ....	18

## Chapter II: The modeling and analysis of axial turbines

Figure II.1: Axial turbine system with boundary conditions. ....	20
Figure II.2: velocity triangles for a single turbine stage . ....	21
Figure II.3: A normal velocity triangle for an axial turbine ....	22
Figure II.4: Cylindrical illustration of a control volume ....	23
Figure II.5: Representation of vector forces ....	29

Figure II.6: Rotor schematic and Euler equation. ....	30
Figure II.7: left-Impulse turbine cascade, right-Reaction turbine cascade velocity triangles .....	33
Figure II.8: The Smith chart for turbomachinery. ....	34
Figure II.9: h-s diagram of a turbine stage . ....	39
Figure II.10: flow regime and layer thickness . ....	40

### **Chapter III: Numerical Methods and CFD implementation**

Figure III.1: An FDM grid representation. ....	54
Figure III.2: Control volume illustration .....	55
Figure III.3: representation of a structured mesh. ....	56
Figure III.4: Body-fitted mesh representation . ....	56
Figure III.5: Representation of a double unstructured mesh. ....	57
Figure III.6: Geometrical shapes representation. ....	57
Figure III.7: Control volume representation in cylindrical coordinates. ....	59
Figure III.8: a turbomachine simulation example. ....	61
Figure III.9: Multigrid method. ....	65
Figure III.10: CFX Algorithm .....	66
Figure III.11: CFturbo Interface + Global setup. ....	68
Figure III.12: The 3D representation of the default model .....	69
Figure III.13: Blade setup and span number panels in CFturbo. ....	70
Figure III.14: Stator Blade angles spanwise. ....	71
Figure III.15: Cascade 3D illustration. ....	72
Figure III.16: Step-by-step process illustration .....	72
Figure III.17: Preview of the study mesh. ....	73
Figure III.18: Neural Network Layers .....	74
Figure III.19: Neural network unit data process schematic . ....	75

### **Chapter IV: Results and Discussion**

Figure IV.1: Size Factor vs Efficiency CFD results. ....	83
Figure IV.2: Domain meshing and a zoom-in of the profile perimeter body-fitted mesh. ....	84
Figure IV.3: Pressure coefficient vs x/c plots, Bottom (Thesis) and Top (NASA-report) . ....	86
Figure IV.4: Inlet angle vs efficiency chart. ....	88

Figure IV.5: Rotor turbulent kinetic energy contour with the high intensity zone encircled. ....	89
Figure IV.6: Temperature Contours. ....	91
Figure 7: Temperature Contours. ....	91
Figure IV.8: Temperature distribution across both blades. ....	92
Figure IV.9: Density contours between a mild outlet angle ( $-60^\circ$ ) and an intense outlet angle ( $-75^\circ$ ). ....	93
Figure IV.10: Entropy generation streamwise, the absence of losses in the wake-like zones, with higher value at the trailing edge outlet. ....	94
Figure IV.11: Pressure distribution for all cases. ....	94
Figure IV.12: Pressure Contours. ....	96
Figure 13: Blade pressure loading. ....	97
Figure IV.14: Blade pressure loading. ....	97
Figure IV.15: Velocity vertex samples to show the discussed properties. ....	99
Figure IV.16: Mach number contours. ....	100
Figure IV.17: Neural Network diagram. ....	104
Figure IV.18: Regression Training graph. ....	105
Figure IV.19: Regression validation graph. ....	106
Figure IV.20: Regression Testing graph. ....	107
Figure IV.21: Global Graph. ....	108
Figure IV.22: Prediction vs reality results. ....	110

## List of tables

Table III.1: Cylindrical coordinates system .....	58
Table III.2: General stator parameters. ....	70
Table III.3: General rotor parameters. ....	71
Table III.4: Meshing Results. ....	73
Table IV.1:CFX parameters types and values. ....	80
Table IV.2: CFD grid convergence study table. ....	82
Table IV.3: GCI values. ....	82
Table IV.4: Results Comparison. ....	85
Table IV.5: Simulation Results Values. ....	87

# Nomenclature

Symbol	Definition	Unit
A	Cross-sectional flow area	m <sup>2</sup>
b	Blade height (cascade width)	m
b <sub>i</sub>	Bias of neuron i	—
C	Absolute velocity	m/s
C <sub>p</sub> , C <sub>v</sub>	Specific heats at constant pressure / volume	J/kg·K
D, d <sub>h</sub>	Diameter (overall, hub or tip)	m
e	Specific energy	J/kg
F <sub>S</sub>	Safety factor	—
h, h <sub>0</sub>	Static and total enthalpy	J/kg
i	Angle of attack	°
IV	Interpolation Variable	—
k	Turbulent kinetic energy	m <sup>2</sup> /s <sup>2</sup>
L	Momentum factor	—
mw <sub>ij(old)</sub>	Previous weight (momentum update)	—
$\dot{m}$	Mass flow rate	kg/s
P, P <sub>0</sub>	Static and total pressure	Pa
P, W, E, N, S, B, T	Volume centers in FVM	—
q	Fourier's law of heat conduction	W/m <sup>2</sup>
$\dot{Q}$	Heat transfer rate	W
$\dot{Q}_V$	Volumetric flow rate	m <sup>3</sup> /s
r	Radius (cylindrical coordinate)	m
R <sub>cst</sub>	Universal specific gas constant	J/mol·K
T, T <sub>0</sub>	Static and total temperature	K
U	Blade peripheral speed	m/s
V <sub>r</sub>	Radial component of velocity	m/s
V <sub>θ</sub>	Tangential component of velocity (θ-direction)	m/s
V <sub>z</sub>	Axial component of velocity (z-direction)	m/s



$w_{ij}$	Weight from neuron j to neuron i	—
$W$	Relative velocity	m/s
$\dot{W}$	Power (shaft, viscous, aerodynamic)	W
$x_j$	Input from neuron j	—
$x_{pi}$	Activation of neuron i for pattern p	—
$X$	Input matrix	—
$Y$	Output variable (efficiency)	—
$Z$	Number of blades	—
$z$	Axial coordinate	m

## Greek Symbols

Symbol	Definition	Unit
$\alpha_{1, 2}$	Absolute flow angles	°
$\beta_{1, 2}$	Relative flow angles	°
$\beta_{B1,2}$	Blade metal angles at inlet/outlet	°
$\delta$	Deviation angle	°
$\delta^*$	Displacement boundary layer thickness	m
$\varepsilon$	Turbulent dissipation rate	m <sup>2</sup> /s <sup>3</sup>
$\epsilon$	Relative error or residual	—
$\gamma$	Ratio of specific heats $C_p/C_v$	—
$\eta_{tt}$	Total-to-total efficiency	—
$\phi$	Transport variable (e.g., u, T, k, $\varepsilon$ , ...)	—
$\varphi$	Flow coefficient ( $C_x/U$ )	—
$\varrho$	Dissipation function	—
$\theta$	Cumferential angle	rad / °
$\vartheta_r, \vartheta_z$	Control volume sizes (r and z directions)	—
$\tau$	Shear stress	Pa
$\omega$	Angular velocity / Specific dissipation rate	rad/s

$\delta_{pj}$	Error gradient for neuron j	—
$\psi$	Stage work coefficient	—
$\psi^*$	Stage loading coefficient	—

## Abbreviations

Abbreviation	Definition
ANN	Artificial Neural Network
CFD	Computational Fluid Dynamics
CFX	Computational Fluid eXpert (ANSYS)
FDM	Finite Difference Method
FEM	Finite Elements Method
FVM	Finite Volume Method
GCI	Grid Convergence Index
IV	Interpolation Variable
OA	Order of Accuracy
RANS	Reynolds-Averaged Navier–Stokes
RNG	Renormalization Group
RPM	Revolutions Per Minute
RSM	Reynolds Stress Model
SST	Shear Stress Transport

## General Introduction

# General Introduction

The growing need for efficient, clean, and sustainable energy technologies has accelerated research in thermal engineering and placed turbomachinery at the heart of innovation in energy conversion systems, specifically the axial gas turbines. This branch has been under consistent development due its vital role in efficient energy conversion, high power output compared to its size, easiness of integration and adaptability into diverse systems across major industries such as aerospace propulsion and power generation as their design not only impacts the general performance of such technologies but also affect the environment and economy. For an efficient functioning of such complex machinery, the aerodynamic and thermodynamic behavior across the blade cascade passage must be really controlled to avoid unwanted losses that lead to the degradation of its overall efficiency.

In this context, the present thesis focuses on the 3D design and computational analysis of a small-scale, purely axial gas turbine cascades, with the primary goal of optimizing and enhancing its total-to-total efficiency. The turbine cascade features a fixed stator geometry, where both the inlet and outlet blade metal angles are held constant, while the rotor geometry is systematically modified across 40 different configurations. Air, treated as an ideal gas, is used as the working fluid to simplify the modeling while preserving realistic flow behavior. To achieve the set objectives, advanced Computational Fluid Dynamics (CFD) simulations are conducted to analyze the internal flow characteristics, capturing velocity fields, temperature and pressure gradients, and aerodynamic loss mechanisms. Additionally, a scaling approach is implemented to transition from the small-scale model to an industrial-sized turbine. Artificial Neural Networks (ANNs) are also employed to predict performance metrics and compare them with CFD results across various design scenarios. This hybrid approach provides valuable insights and design flexibility in the field of turbomachinery optimization.

Also, the working methodology is based on 3 powerful platforms. CFturbo is used to generate the axial turbine stator-rotor 3D cascade and passage. Then, ANSYS CFX is used to simulate the flow field and to determine the boundary conditions such as the inlet and outlet with the separating passage between the two blades, thermodynamic parameters, solve the governing

equations for mass conservation, momentum, and energy. At last, MATHWORKS MATLAB is used to develop and train an ANN model using an expanded data-set (up to 108 simulations) to capture patterns and make precise predictions for a vast design space.

Using these combinations, this thesis contributes to the continuous efforts to optimize axial turbines with its practical work frame that could be up-scaled to an industrial turbine design with the same properties even with more complex conditions. This thesis is organized into 4 essential chapters with each one serving as a critical step in the development of this study:

- ✓ Chapter I: outlines the basic concepts and definitions on turbomachinery with a focus on axial flow turbines. Covering its main components, the definition and the role of each blade angle, and ending with a literature review on previous research papers which held the motivations behind this study.
- ✓ Chapter II: covers the theoretical background of the governing equations and turbomachinery equations, from the velocity triangles and conservation laws up to the simplification of the flow cylindrical equations based on well-chosen hypothesis. Also, non-dimensional and thermodynamic parameters are introduced along with multiple detailed turbulence models to clarify the choices made in the following chapters.
- ✓ Chapter III: holds the detailed explanation of the major numerical approaches used in simulations, mesh generation, and discretization methods. CFturbo geometry creation process is further detailed in this chapter with all the chosen variable values and parameters along with CFX simulation setup and general algorithm. It also details the ANNs phases explanation and step to model it in MATLAB.
- ✓ Chapter IV: considered the most important part of this entire study, since it presents the final results and comparisons across all the configurations. The small to large geometry scaling. The ANN results are evaluated to determine its capability. But all these results are extracted after doing validation tests on the NACA-4412 profile using the chosen simulation model (turbulence model and the thermodynamic parameters) and the implementation of the GCI (Grid convergence index) to help choose the proper grid for our geometry since the grid independence study never fully converged. This thesis concludes with a general conclusion and perspectives for future studies to take this field of research into a whole new level

# CHAPTER I

# **Introduction to Axial Turbines and Fundamental Turbomachinery Concepts**

## **I. Introduction**

This chapter explores the fundamental role of turbomachinery in modern energy conversion, with a particular emphasis on the design and application of axial turbines in power systems and engineering. It begins by defining turbomachinery and reviewing the primary classification of turbines, while highlighting the significance of axial turbines.

The discussion then focuses on the main components specifically the stator and the rotor that regulate the fluid flow and enhance energy extraction. Additionally, the chapter introduces all the important parameters and concepts and concludes with a concise literature review that outlines previous research and identifies existing gaps to be addressed in this study.

## **II. Fundamentals of Turbomachinery**

### **II.1 Definition of turbomachinery**

Although definitions vary among experts, there is a general consensus that turbomachines are devices that facilitate energy exchange between a moving fluid and rotating components. This exchange occurs through dynamic interactions that modify the fluid's pressure and momentum, usually under steady-flow conditions. As a result, the term includes not only large-scale power generators but also machines designed to create pressure differentials, such as centrifugal pumps and compressors [1].

Turbomachinery is essential across various sectors, including power generation, aerospace, and transportation for both civilian and military applications. In power plants, turbines powered by steam, gas, or hydraulic energy are used across a wide capacity range, from a few kilowatts to several thousand megawatts to drive generators that produce electricity at the necessary frequency. In aviation and heavy military vehicles, gas turbines are typically the preferred propulsion systems.

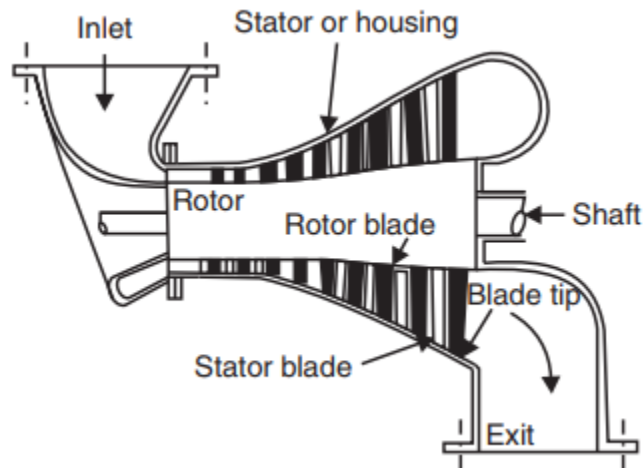


**Figure I.1:** cross-sectional view of the parts of a turbomachine [1].

### II.1.1 Classification of Turbomachinery

#### II.1.1.1 Classification by energy interaction

➤ **Energy-augmenting machines:**

These instruments are designed to inject energy into the fluid. Typical examples include various types of pumps and compressors that elevate the fluid's energy level as it flows through the system.

➤ **Energy extracting machines:**

These devices are engineered to withdraw energy from the fluid. Prime instances are turbines operating on steam, gas or water, which convert fluid's energy into mechanical work

➤ **Dual function machines:**

Certain equipment performs both energy adding and extraction, such as torque converters or energy transmitters that simultaneously supply and harness energy from the fluid stream.



### II.1.1.2 Classification based on pressure alteration

#### ➤ Pressure enhancing machines:

Adds energy to a fluid, thereby elevating its pressure by compressing or accelerating the flow. Examples include rotary and reciprocating pumps, compressors. [1][2]

#### ➤ pressure reducing machines:

These machines extract energy from the fluid, allowing it to expand and resulting in a reduction in pressure. Notable examples are turbines whether driven by water, steam, or gas as well as wind driven systems. [1][2]

### II.1.1.3 Classification based on flow orientation

#### Linear flow machines:

The fluid flows in a straight and uninterrupted path. A perfect example is the reciprocating pump, where the fluid is moved directly in a linear manner by the oscillating mechanism. [1][2]

#### Radial flow machines

The fluid is directed outward from a central hub. Centrifugal pumps are the prime representatives of this design, as they force the fluid perpendicularly away from the center to the impeller, thereby accelerating it radially for efficient energy transfer. [1][2]

#### Axial flow machines:

The working fluid is directed to flow parallel to the axis of rotation, axial turbines which are the primary example are designed to maintain this alignment with the rotor's axis to optimize energy conversion and performance. [1][2]

#### Mixed flow machines:

Also called diagonal flow machines, oblique flow machines, these late merge elements of both axial and radial flow by channeling the fluid along a trajectory that contains both parallel and perpendicular directions relative to the rotation axis. [1][2]

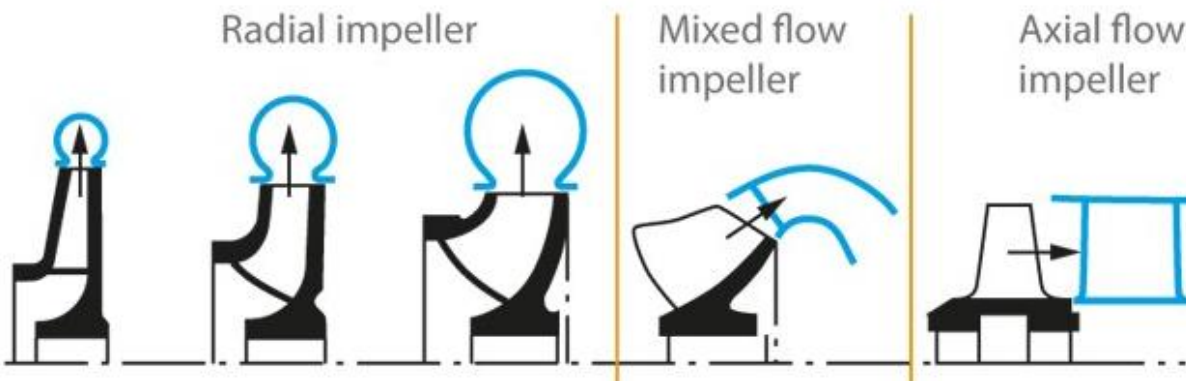


**Figure I.2:** classification of turbomachines based on flow direction. [3]

### III. Axial flow turbines

Axial flow turbines are the cornerstone of power generation, offering superior efficiency compared to other designs, these turbines are extensively applied in aerospace propulsion as well as in industrial and marine power systems. Their evolution has been primarily driven by the imperative of achieving higher mass flow rates and optimal compression ratios.

### IV. Definitions of axial flow turbine components:

#### IV.1 Stator

A stationary component that channels the fluid flow to enhance its interactions with the rotor, this component is critical in multistage turbines such as the ones used in jet engines where it straightens out the turbulent airflow so the rotor can work efficiently. [2][4]

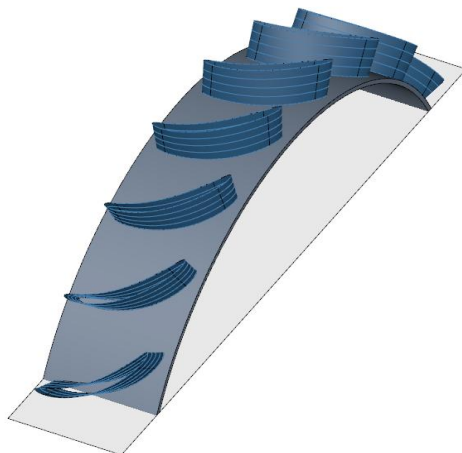


**Figure I.3:** 3D Stator Example generated [5] using CFTurbo [6].

### IV.2 Rotor

The rotating component of turbomachines, comprising blades fixed to a rotating axis, its terminology varies depending on the type of application:

- Impeller: in centrifugal pumps/compressors, where it radially accelerates the fluid.
- Runner: used in radial hydraulic turbines and pumps, it facilitates the fluid's circular motion.
- Rotor: generally applied in axial flow systems. [2][8]

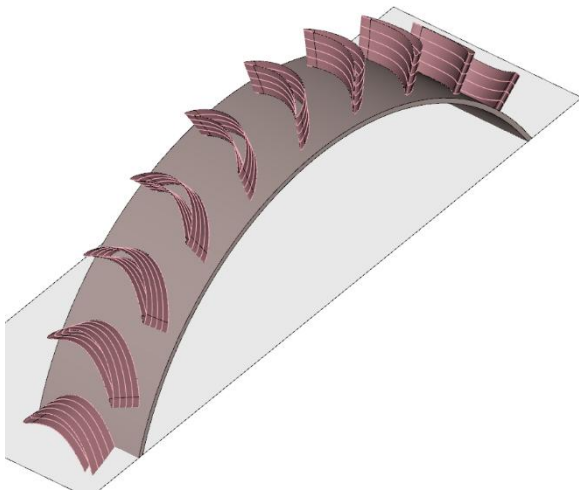


**Figure I.5:** 3D Rotor generated [5] using CFturbo [6].

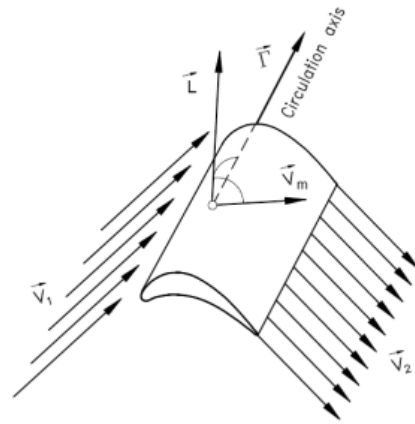


**Figure I.4:** A simple 3d representation of a rotor blade [10].

### IV.3 Hub

The hub serves as the primary pivoting structure that anchors blades to the shaft. It plays a vital role in keeping up the structural durability against centrifugal forces at elevated RPM which maximizes energy extraction. [2][8][9]

### IV.4 Shroud

It is a covering that encases the tips of blades to lessen leakage losses. In gas turbines, shrouded blades are the main cause to enhance efficiency [11].

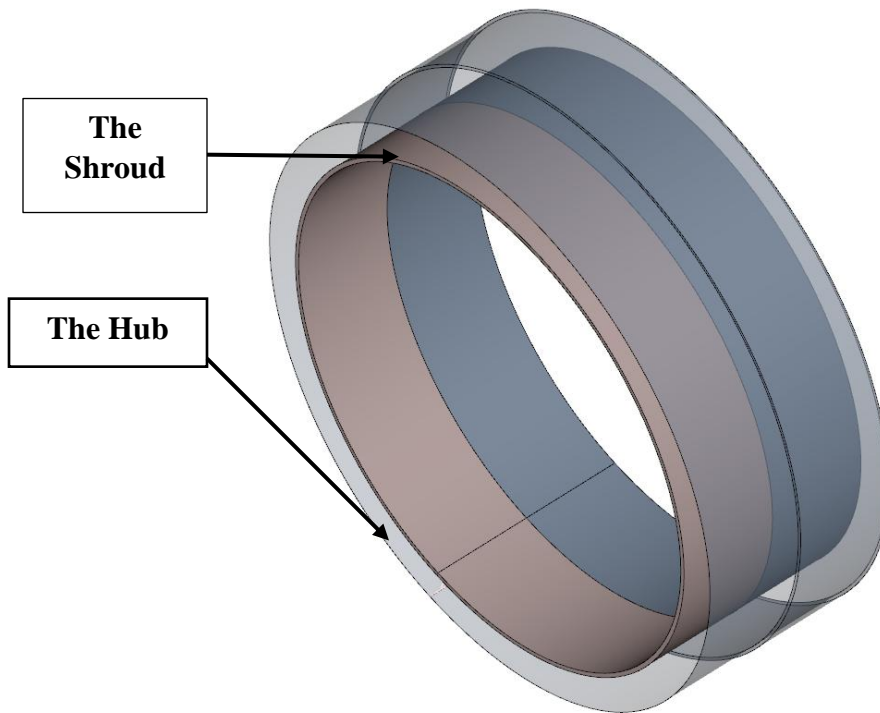


**Figure I.6:** Hub and Shroud 3D examples generated [5] CFturbo [6].

#### IV.5 Stage structure and reaction

Axial turbines stages comprise sequential stator or the nozzle-rotor blade pairs that collectively govern the conversion of fluid enthalpy into mechanical work. The degree of reaction ‘R’ quantifies the proportion of total stage static pressure drop occurring across the two blades [12] specifically:

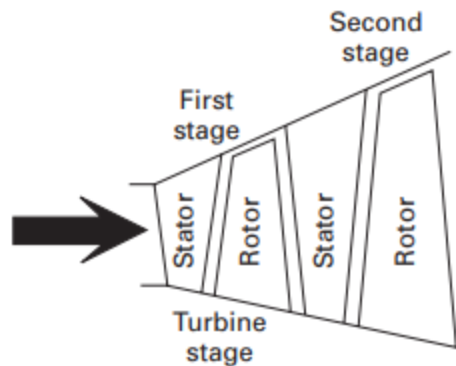


**Figure I.7:** 2 stage axial turbine design [12].

- $R=0$  (impulse stage): entire enthalpy drop occurs in the stator(nozzle).
- $R=1$  (pure reaction stage): entire enthalpy drop occurs in the rotor.
- $R=0.5$  (50% reaction stage): enthalpy drop is equally distributed between the stator-rotor pair [12].

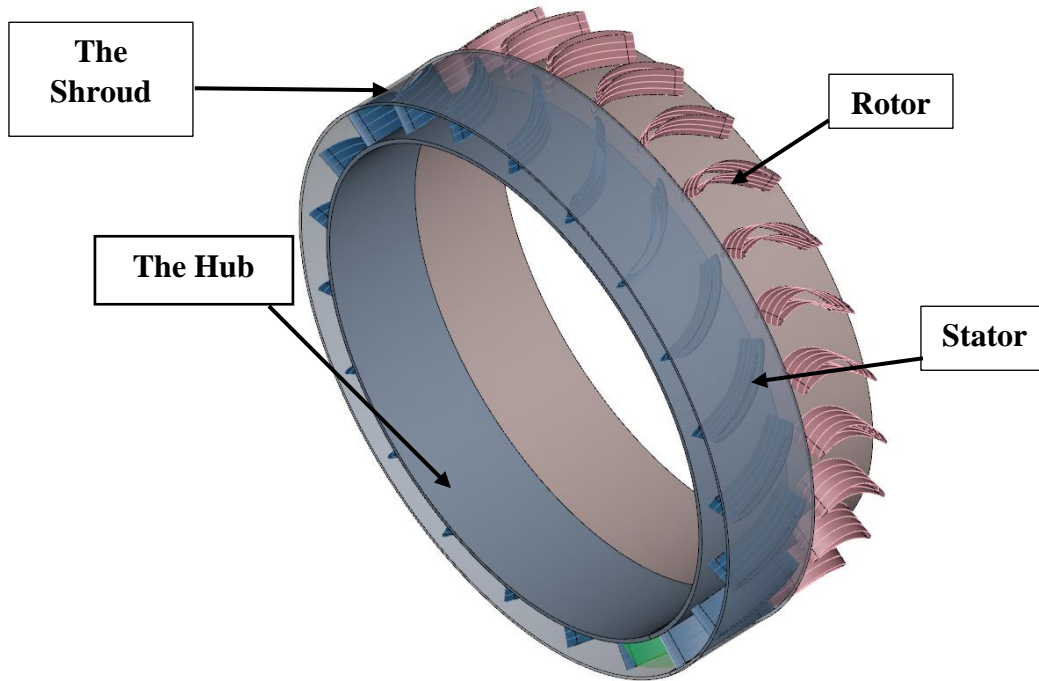


**Figure I.8:** Full Stage 3D representation using CFTurbo [6].

### IV.6 Pressure profile and energy extraction

The progression of fluid through successive turbine stages induces a progressive reduction in static pressure, establishing a favorable pressure gradient along the flow path. This gradient inherently mitigates surge potential by maintaining boundary layer stability, in contrast to the adverse gradients typical of compression systems. The thermodynamic asymmetry between expansion and compression processes enables turbine stages to achieve substantially higher specific output compared to compressor stages. Consequently, this work differential permits a single turbine stage to provide sufficient shaft power to drive multiple compressor stages in typical configurations, a critical consideration for maintaining energy balance in gas turbine engines [2] [12].

## IV.7 Aerodynamic design and flow regulation in turbine stages

The aerodynamic efficiency and stage pressure ratio in axial turbines are governed by the blade profile geometry and flow path management. Upon entering the stator cascade, the working fluid is accelerated through blade passages, which minimize incidence losses and direct flow at a controlled angle of attack. Subsequent expansion occurs through both blades rows with the rotor extracting mechanical energy via angular momentum alteration [2] [12].

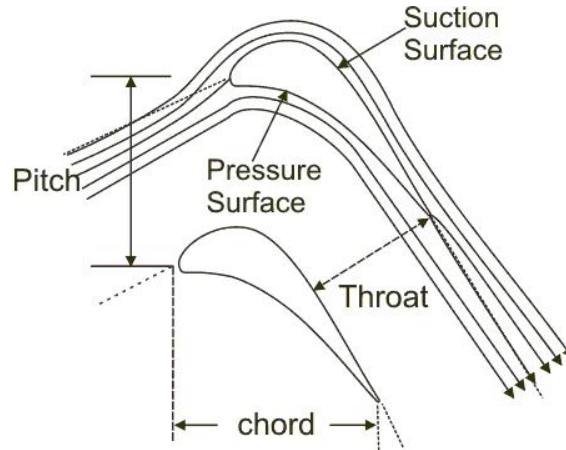


Figure I.9: diagram of flow through a passage [13].

## V. Blade angles

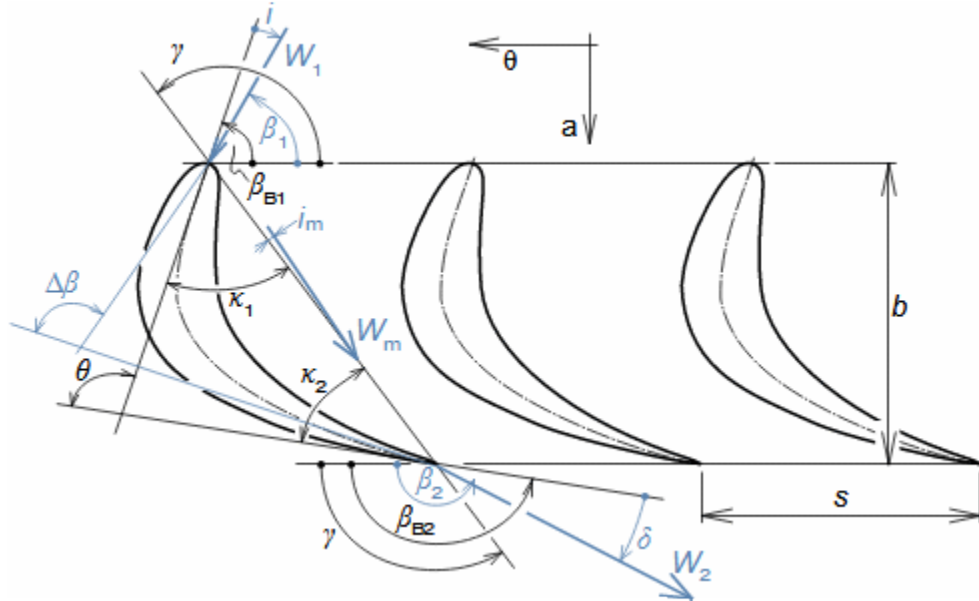


Figure I.10: general angles of a profile cascade.[14].

### V.1 Inlet blade metal angle ( $\beta_{B_1}$ )

This angle defines the blade's orientation where the fluid first enters the cascade. It is vital for directing the flow at an optimal incidence, thus minimizing the angular mismatch between incoming flow and blade [16][18].

### V.2 outlet blade metal angle ( $\beta_{B_2}$ )

this angle determines the direction in which the fluid exits the cascade. A well-chosen outlet angle helps prevent flow separation and energy losses [17].

### V.3 angle of attack ( $i$ )

defined as the angles between the incoming fluid velocity and the blade's chord (camber line). It is essential for generating effective lift and lower flow disruption [15].

### V.4 deviation angle ( $\delta$ )

measures the difference between the blade's designed camber and the exit flow direction. Essential for preserving aerodynamic efficiency [16].

### V.5 flow camber ( $\Delta\beta$ )

denotes the overall change in the fluid's direction across the cascade which directly impacts energy transfer [18].

### V.6 cascade width ( $b$ )

represents the effective flow passage between blades, affects the fluid's velocity and mass flow rate [17].

### V.7 inlet and outlet velocities ( $W_1$ and $W_2$ )

the velocities shaped by the cascade geometry at the inlet  $W_1$  and outlet  $W_2$  are fundamental in determining the kinetic energy available for the conversion [16].

### V.8 Mean aerodynamic velocity $W_m$ and mean angle of attack $i_m$

the  $W_m$  is an averaged value that simplifies flow analysis through the cascade. Similarly,  $i_m$  serves as a benchmark for assessing the overall aerodynamic performance [15].

### VI. Axial gas turbines

A gas turbine is a turbomachine Operating on the Brayton thermodynamic cycle that transforms the energy from fuel combustion into mechanical work through three essential components: an air compressor, a combustion chamber, and a turbine [19].

Originating from early 20th century aviation engines, modern gas turbines are now widely used in power generation and propulsion applications due to their fast operational readiness, compact design, and high power to weight ratios [1].

#### VI.1 Primary components

##### VI.1.1 Compressor

- Draws in and compresses ambient air, achieving pressure ratios of 15:1 to 30:1 using multi-stage axial or radial designs [19].
- Consumes 30-50% of total turbine output, operating at approximately 87% efficiency via precision-engineered blade aerodynamics [1].

##### VI.1.2 Combustion chamber

- Enclosed chamber blending fuel and compressed air, igniting mixtures at 1600 to 1900 °C.
- Integrates air distribution phases to limit emissions and protect the chamber durability [1].

##### VI.1.3 Turbine

Converts thermal energy into rotation via stator guided gas expansion across rotor blades. High-pressure stages withstand extreme heat via advanced Nickel-based alloys and air film cooling [19].

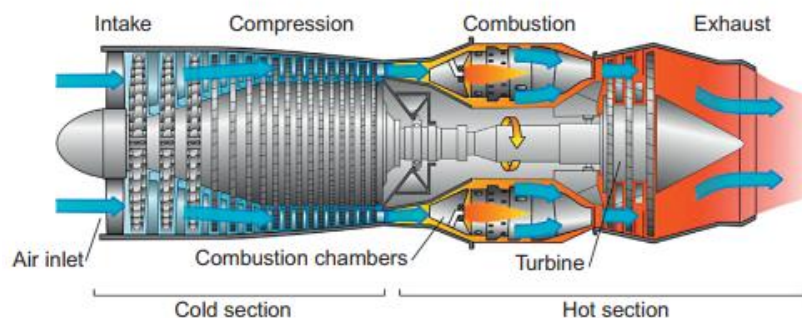


**Figure I.11:** detailed schematic of a Turbo-reactor [20].



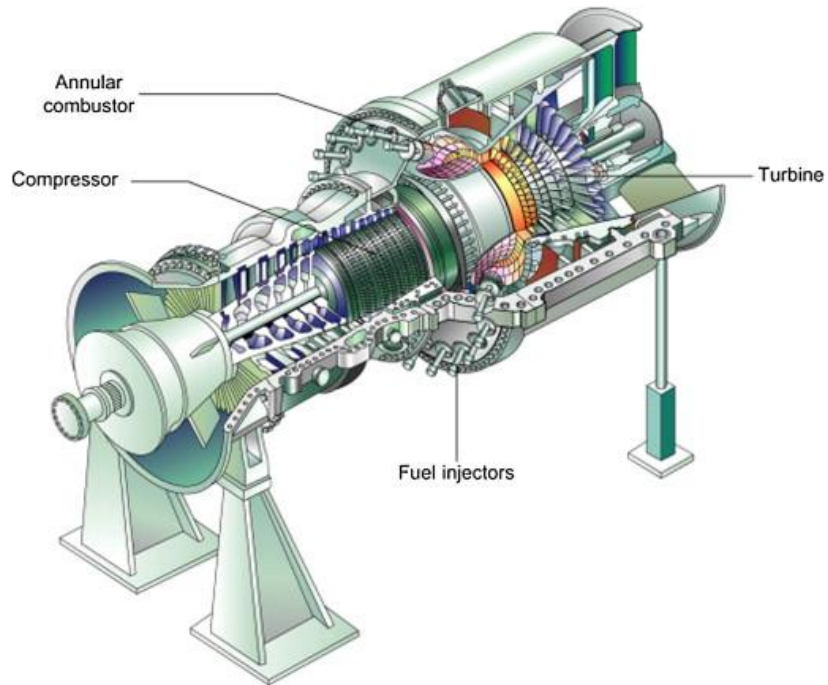


Figure I.12: cross-section of an industrial gas turbine [21].

## VI.2 Operational mechanism

The Brayton cycle comprise four sequential stages:

- ✓ **Adiabatic compression:** air density increases via mechanical compression.
- ✓ **Constant-pressure combustion:** fuel burns steadily, elevating gas enthalpy
- ✓ **Adiabatic expansion:** high-pressure gas drives turbine blades, rotating the shaft.
- ✓ **Exhaust discharge:** residual heat exits or feed secondary systems (steam turbines) [19].

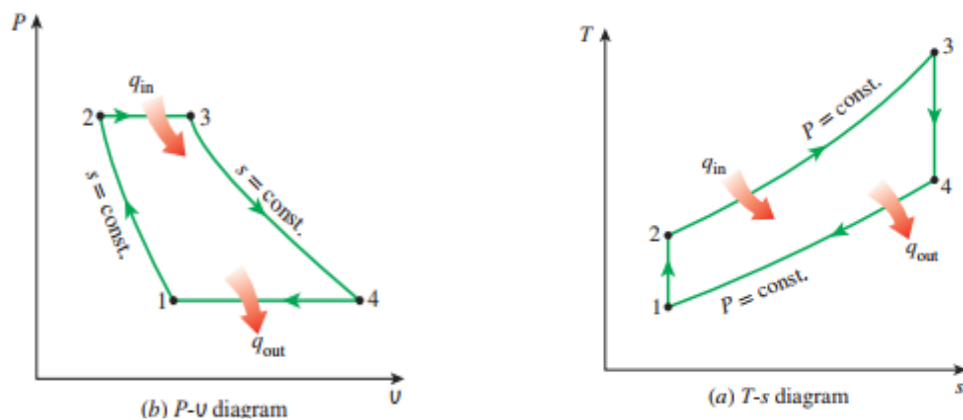


Figure I.13: thermodynamic cycles of the Brayton cycle [8].

## VII. Advances in axial turbine technology: a review of past studies and researches

Recent advances in axial turbine technology have profoundly impacted the design of gas turbines, resulting in notable improvements in efficiency, performance, and reliability. These developments have been supported by a rich body of research that encompasses both classical aerodynamic principles and current CFD analysis and optimization techniques.

This section critically examines these seminal studies, demonstrating how each has contributed to the progressive refinement of turbine technology and providing a foundation for the ensuing literature review, down below some of the most recent studies in this field:

Taghavi Zenouz and Abiri (2024) present a pioneering investigation that merges traditional aerodynamic techniques with contemporary computational fluid dynamics methodologies to develop a highly efficient two-stage axial turbine. Their research is structured in two distinct phases: initially, they employ streamline curvature and free vortex methods to create intricate three-dimensional blade geometries and to forecast flow characteristics, which, while exhibiting slight variations when compared to 3D-CFD results, provide a solid foundation [22].

In the subsequent phase, they enhance turbine performance through meticulous clocking of the low-pressure turbine LPT stator blades which resulted in a modest yet a meaningful enhancement in both inlet total pressure and output power, ultimately achieving an overall efficiency of 91.83%. the findings of this study contribute significantly to understanding the dynamics of wake interactions and blade loading [22].

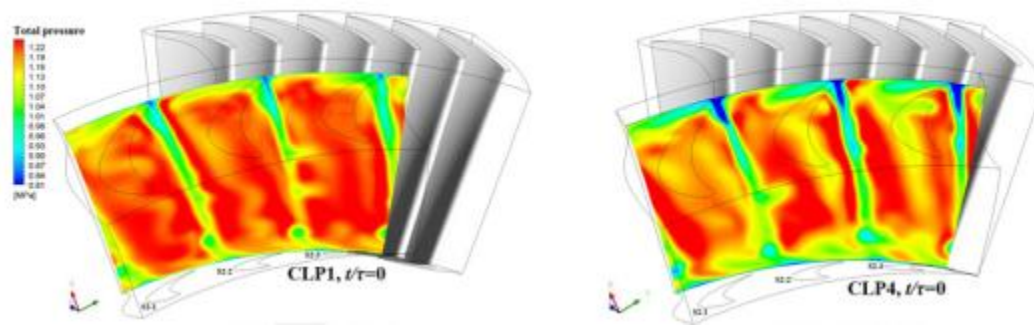


**Figure I.14:** Snippet example of pressure contours [22].

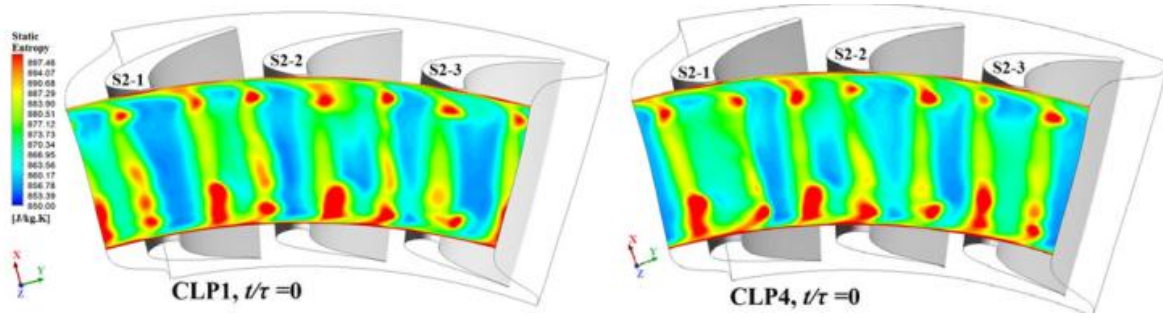


**Figure I.15:** Snippet example of pressure contours [22].

Souverein & al. (2017) conduct a systematic analysis utilizing the Baljé-diagram to assess how variation in rotor blade design influence turbine efficiency of axial turbines. The study employs four distinct blade profiling techniques, which include three parametric design methods alongside a configuration based on a reference catalogue. The authors investigate the interplay between blade geometry, rotor loss coefficients, and the overall performance of the turbine. Through CFD simulations, it is revealed that a circular arc blade designs closely align with the original Baljé correlation, whereas alternative configurations, such as those utilizing Bézier curves and profiles derived from catalogues, can enhance efficiency by as much as 10% relative to traditional predictions [23].

Additionally, the research suggests that adjustments to specific geometric parameters, including blade aspect ratio and quantity, may facilitate improved flow redirection and optimize energy extraction. These findings provide valuable insights for the preliminary design of turbomachinery, highlighting the importance of tailored blade profiling techniques to enhance aerodynamic efficiency and improve the predictive reliability of semi-empirical design models like the Baljé-diagram [23].

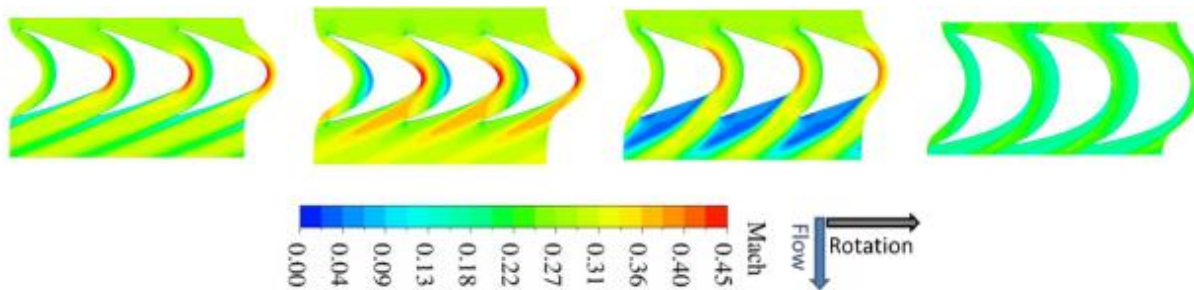


**Figure I.16:** snippet example of Mach contours [23].

Zhang and Janeway (2022) introduce an innovative optimization framework that combines high-fidelity computational fluid dynamics (CFD) simulations with Artificial Neural Network (ANN) surrogate models to enhance the aerodynamic performance of turbine blades. The methodology initiates with the training of ANN models using a comprehensive dataset obtained from over 3000 two-dimensional CFD simulations of various turbine blade profiles.

These surrogate models facilitate a nested optimization approach, which strategically directs a limited number of three-dimensional CFD analyses to pinpoint superior design options. This strategy achieves a reduction in computational expenses by approximately five times when compared to traditional CFD only techniques [24].

When applied to the high-pressure turbine blade of the NASA/General Electric Energy Efficient Engine, the framework produces Pareto-optimal blade geometries that demonstrate improved efficiency and power output. Significant findings indicate that the lean angle and tip scaling factor are pivotal optimization parameters, while optimized designs show reduced trailing-edge negative pressure coefficients and improved shockwave interactions, both of which contribute to enhanced aerodynamic performance [24].

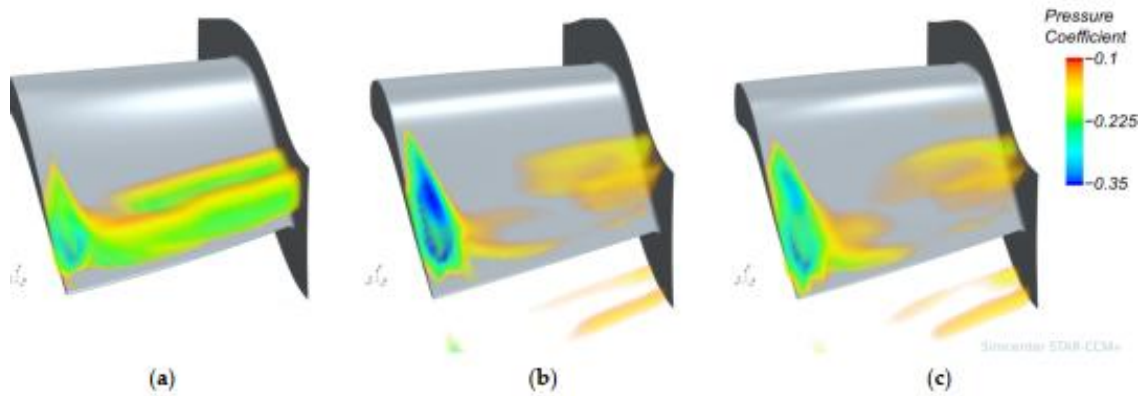


**Figure I.17:** Static pressure distribution [24].

Asgarshamsi & al. (2014) performed a numerical optimization analysis on the rear section of a single-stage axial turbine to optimize its total-to-total efficiency and pressure ratio. The study implemented a genetic algorithm (GA) paired with CFD simulations, they optimized stator and rotor lean/sweep angles across multiple operating points.

Compressible Navier-Stokes simulations validated with experimental data revealed a 1.31% efficiency gain at design conditions and 1.17% at off-design, alongside a 2.40% rise in choked mass flow. The study highlights the critical role of 3D blade adjustments in minimizing flow losses and enhancing turbine performance, demonstrating the value of integrating evolutionary algorithms with aerodynamic modeling for turbomachinery design. This approach demonstrates significant potential for advancing axial turbine design methodologies, particularly in balancing efficiency, pressure ratio, and operational flexibility [25].

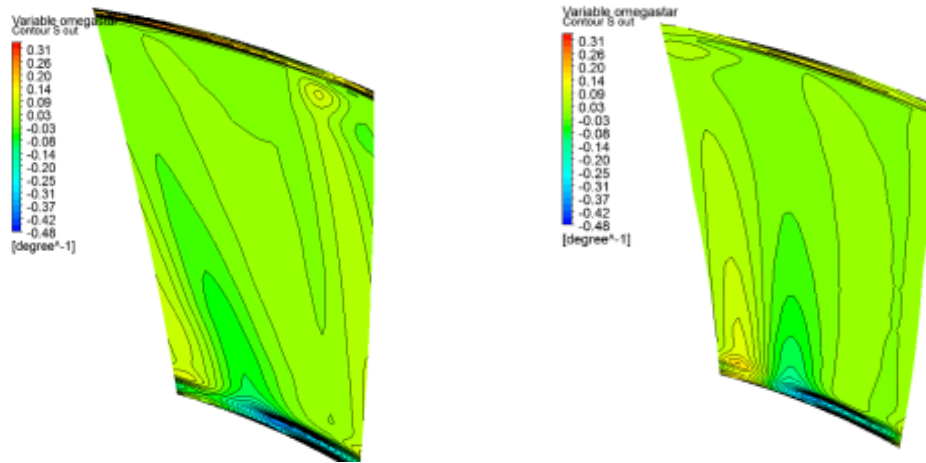


**Figure I.18:** Original (left) and optimized (right) turbine Stator [25].

Kladovasilakis & al. (2017) introduced a new method for designing supersonic rotor blades in organic Rankine cycle (ORC) axial turbines, focusing on non-ideal gas effects in low real-flow settings. Their approach mixed vortex flow theory and the method of characteristics to generate 2D blade geometries optimized for specific working fluids (isobutane, R134a, and an isobutane-isopentane blend). Main results showed that the fluid properties precisely influence blade geometry as follows: lower polytropic indices increased blade pitch and reduced durability, while denser fluids minimized losses from oblique inlet/outlet shockwaves [26].

The degree of reaction augmented with decreasing polytropic index, and the designed blades achieved 92% isentropic efficiency. This work marks the importance of fluid-specific blade optimization to enhance ORC's axial turbine performance in small-scale energy recuperating systems [26].

Monteiro & al. (2012) graded the aerodynamic performance of an axial turbine's 1<sup>st</sup> stage under design and off-design aspects using CFD. To overwhelm the constraints of experimental techniques, steady-state Reynolds-Averaged Navier-Stokes (RANS) simulations with the Spalart Allmaras turbulence model were integrated for 2D and 3D viscous flow analysis.

Results were validated for Denton's mean-line loss model, indicating strong accord and affirming CFD's predictive veracity. The article demonstrated that the 3D simulations outperformed 2D ones by resolving complex flow phenomena, which are essential for loss amplitude. CFD also facilitate detailed flow perception and broader performance analysis, surpassing traditional models. The findings indicate CFD's adequacy in turbine design, offering high-fidelity insights into aerodynamic behavior and fusing gaps between simplified analytical models and real-world flow complication [27].

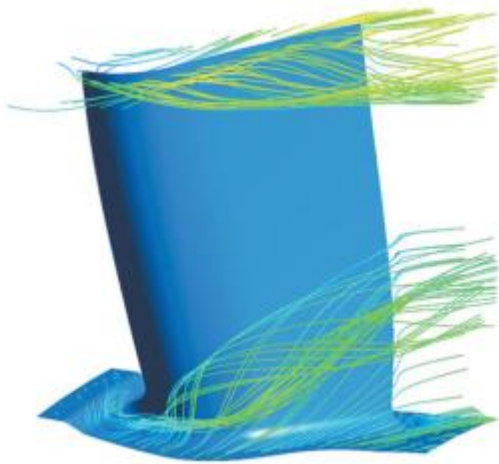


**Figure I.20:** Flow streamlines [27].

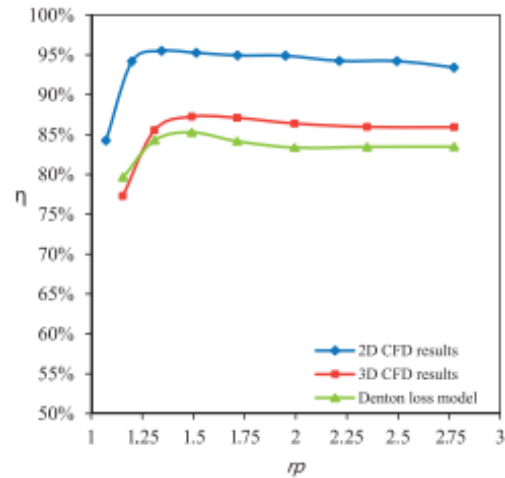


**Figure I.19:** turbine performance as a function of pressure-ratio [27].

## VIII. conclusion

This chapter has delved into the main mechanism governing turbomachinery, with a special focus on the contributions of axial turbines to modern energy systems. Beginning with definitions and classifications and by dissecting critical elements such as the stator, rotor, hub, and the shroud, the analysis highlighted how the blade geometry, stage reaction degree, and pressure govern aerodynamic performance and energy extraction. Furthermore, the operational principle rooted in the Brayton cycle, underscores the importance of these design parameters in optimizing overall performance.

## CHAPTER II



# **The modeling and analysis of axial turbines**

## **Introduction**

This chapter delves into the theoretical modeling and foundational analysis of an axial turbine cascades through fluid mechanics principles and advanced analytical methods. The chapter starts with the governing equations named the conservation of mass, momentum (the Navier-Stokes equations), and energy equations which describe the variation of these principles within the flow. These equations, whether expressed in their conservative or simplified forms serve as the foundation for analyzing the complexity of fluid behavior. The focus then shifts towards some specific metrics of turbomachinery such as non-dimensional parameters including the loss coefficients and the degree of reaction that are introduced to provide means for characterizing the performance across multiple turbine sizes which facilitates the comparisons that leads to optimizing efficiency trends for scale-dependent variables.

Attention is then directed to the role of velocity diagram in the analysis of turbines. These diagrams map the interplay between different velocity components as much as it reveals how blade entry and exit angles points the sharpness of energy extraction or in other words, these diagrams allow the translation of equation into graphical blueprints. Also, the chapter examines turbulence by presenting its fundamental equations and key CFD models, then outlining the system representation such as the details of inlet and boundary conditions along with numerical assumptions to set up a solid ground for simulations and evaluations.

## **I. Study system Overview**

The illustration down below provides a general overview of the main axial turbine system used in this study which connects the theoretical principles with practical design parameters. It identifies the 2 principal components which are the stator and the rotor. Key inlet boundary conditions such as pressure, temperature and mass flow rate as well as the critical blade metal angles knowing that their numerical values will be further illustrated and discussed in the upcoming chapter, are highlighted to illustrate how the ideal air gas is transformed as it passes through the cascade.



This schematic forms the basis for the detailed numerical simulations and analysis discussed in the subsequent chapters, for the next step, is to transition from the conceptual model framework. The following chapter mainly focuses on the numerical methods implemented in this study. Furthermore, it will cover the process of geometry creation and meshing, which are fundamental for the analysis of the turbine models.

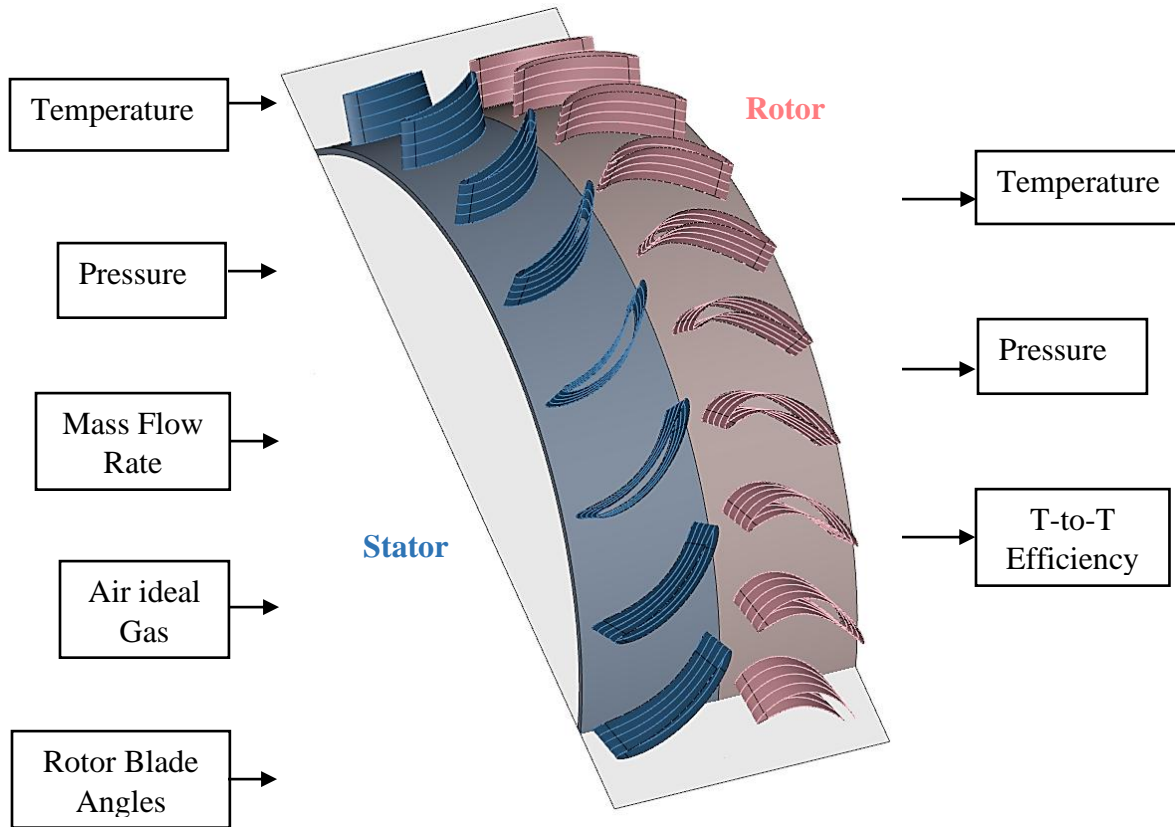


**Figure II.1:** Axial turbine system with boundary conditions [5][6].

## II. Velocity triangles of axial turbines

Velocity triangles graphically represent the flow at a turbomachine stage by using mean values for velocity vectors across the finite cross-section. They combine the peripheral velocity ( $U$ ), absolute velocity ( $C$ ), and the relative velocity ( $W$ ) according to the mathematical relation down below, noting that for axial systems, ( $U$ ) is constant across the stage simplifying the analysis:

$$C = U + W \quad (\text{II. 1})$$

A detailed velocity diagram for an axial turbine is shown in the next page alongside important laws that explains and simplifies its understanding [28]:

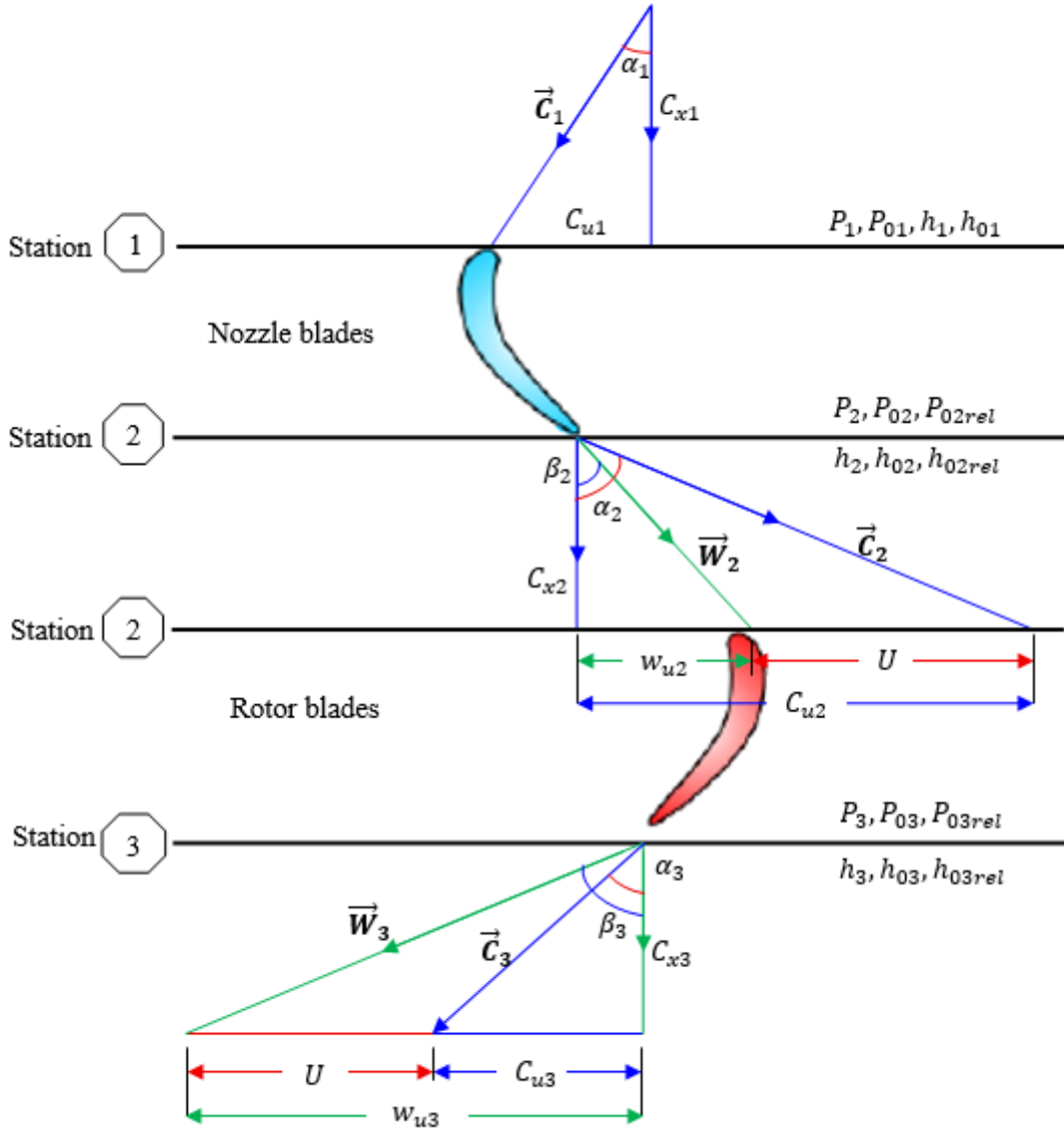


**Figure II.2:** Velocity triangles for a single turbine stage [29].

The fluid enters the stator with an absolute velocity  $C_1$  at an angle  $\alpha_1$  and accelerates to an absolute velocity  $C_2$  at an angle  $\alpha_2$ . At the rotor inlet subtracting the blade speed  $U$  from  $C_2$  yields the rotor's relative velocity  $W_2$  at an angle  $\beta_2$ . After further acceleration to  $W_3$  at an angle  $\beta_3$  within the rotor.

By adding  $U$  to  $W_3$ , the exit absolute velocity  $C_3$  at an angle  $\alpha_3$  is determined. The diagrams reveal that absolute velocities correspond to nozzle angles while the relative ones

correspond to the rotor angles [2]. Also, it is often assumed that the following components are constant throughout the stage [29] [7]:

$$C_x = C_{x1} = C_{x2} = C_{x3} = \text{constant} \quad (\text{II. 2})$$

And

$$C_x = C_1 \cos \alpha_1 = C_2 \cos \alpha_2 = C_3 \cos \alpha_3 = W_2 \cos \beta_2 = W_3 \cos \beta_3 \quad (\text{II. 3})$$

Also

$$U = \text{constant}$$

These assumptions relate to the ‘Normal Velocity Triangle’. Which helps explain the connection between all velocities. Furthermore, a repetitive stage has the following properties [10]:

$$C_1 = C_3 \text{ and } \alpha_1 = \alpha_3$$

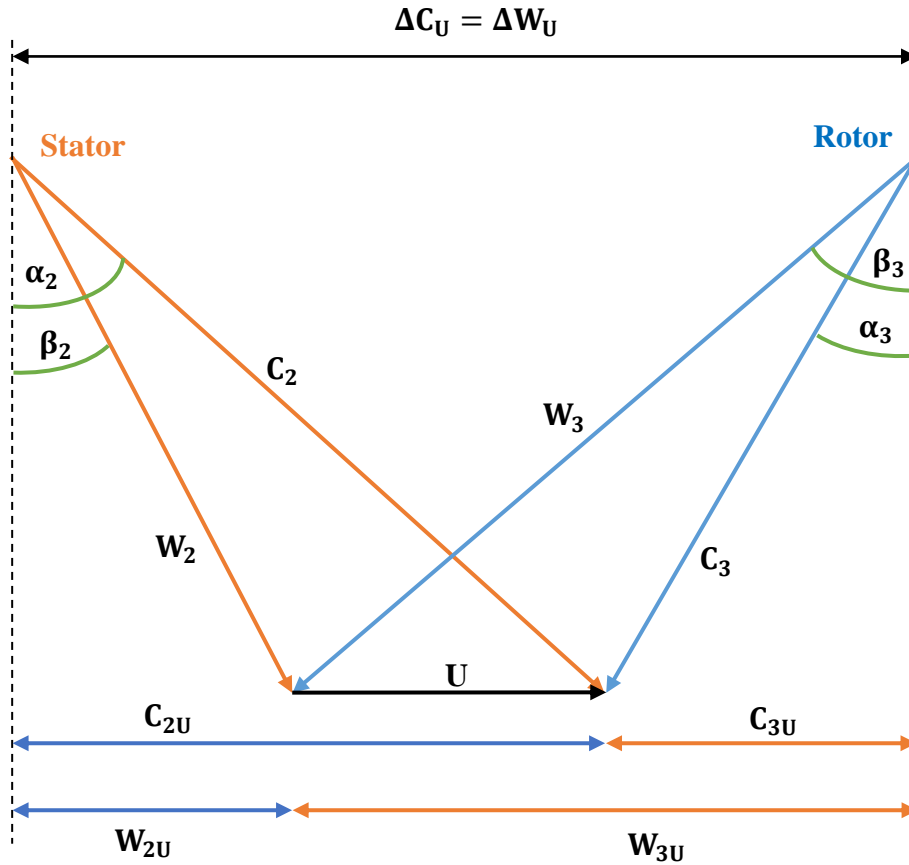


**Figure II.3:** A normal velocity triangle for an axial turbine [30].

### III. Governing equations of turbomachinery

the conservation equations that dictate mass, linear, and angular momentum form core principles essential for the analysis and design of turbomachinery structures. This section offers an abbreviated derivation of these equation, integrating both physical and mathematical concepts.

#### III.1 Mass-conservation equation:

Also widely known as the continuity equation, this principle states that the rate of accumulation of mass within a control volume is equal to the sum of the mass fluxes crossing in and out of its boundaries. Numerically, this can be expressed as [32] [33][34]:

$$\int_{Cv} \frac{\partial m}{\partial t} dV + m_{out,net} = 0 \quad (II. 4)$$

Considering that the control volume shown in figure 5 is simply so small to consider that:

$$\int_{Cv} \frac{\partial m}{\partial t} dV \approx \frac{\partial \rho}{\partial t} (rdr d\theta dz) \quad (II. 5)$$

Also, knowing that the mass flux through each side of the control volume (figure.5) is illustrated:

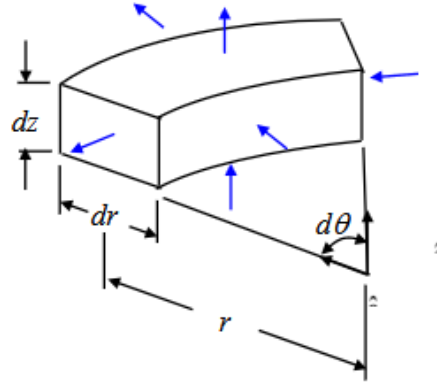


**Figure II.4:** Cylindrical illustration of a control volume [33].

Each side mathematical equation is formulated as:

$$\dot{m}_{in,bottom} = \left[ (\rho V_z) + \frac{\partial}{\partial z} (\rho V_z) \left( -\frac{1}{2} dz \right) \right] (rdr d\theta dz) \quad (II. 6)$$

$$\dot{m}_{\text{out,top}} = \left[ (\rho V_z) + \frac{\partial}{\partial z} (\rho V_z) \left( \frac{1}{2} dz \right) \right] [r dr d\theta dz] \quad (\text{II. 7})$$

$$\dot{m}_{\text{in,front}} = \left[ (\rho V_r) + \frac{\partial}{\partial z} (\rho V_r) \left( -\frac{1}{2} dr \right) \right] \left[ \left( r - \frac{1}{2} dr \right) d\theta dz \right] \quad (\text{II. 8})$$

$$\dot{m}_{\text{out,back}} = \left[ (\rho V_r) + \frac{\partial}{\partial z} (\rho V_r) \left( \frac{1}{2} dr \right) \right] \left[ \left( r + \frac{1}{2} dr \right) d\theta dz \right] \quad (\text{II. 9})$$

$$\dot{m}_{\text{in,RHS}} = \left[ (\rho V_\theta) + \frac{\partial}{\partial z} (\rho V_\theta) \left( \frac{1}{2} d\theta \right) \right] (dr dz) \quad (\text{II. 10})$$

$$\dot{m}_{\text{out,LHS}} = \left[ (\rho V_\theta) + \frac{\partial}{\partial z} (\rho V_\theta) \left( \frac{1}{2} d\theta \right) \right] (dr dz) \quad (\text{II. 11})$$

With

$$\dot{m}_{\text{out,net}} = \dot{m}_{\text{out,top}} + \dot{m}_{\text{out,back}} + \dot{m}_{\text{out,back}} - (\dot{m}_{\text{in,RHS}} + \dot{m}_{\text{in,front}} + \dot{m}_{\text{in,bottom}})$$

The equation (II.4) is reduced to:

$$\frac{\partial \rho}{\partial t} (r dr d\theta dz) + \left[ \frac{\partial \rho}{\partial t} + \frac{\partial}{\partial r} (r \rho V_r) + \frac{1}{r} \frac{\partial}{\partial \theta} (\rho V_\theta) + \frac{\partial}{\partial z} (\rho V_z) + \frac{\rho V_r}{r} \right] (r dr d\theta dz) = 0 \quad (\text{II. 12})$$

Also, it can be written in its indicial form as follows:

$$\frac{\partial \rho}{\partial t} (r dr d\theta dz) + \frac{\partial (\rho V_i)}{\partial x_i} (r dr d\theta dz) = 0 \quad (\text{II. 13})$$

For a 3D compressible flow in cylindrical coordination, the equation is reduced to [32]:

$$\frac{\partial \rho}{\partial t} + \frac{1}{r} \frac{\partial}{\partial r} (r \rho V_r) + \frac{1}{r} \frac{\partial}{\partial \theta} (\rho V_\theta) + \frac{\partial}{\partial z} (\rho V_z) = 0 \quad (\text{II. 14})$$

### III.2 Linear Momentum equations:

Also known as the Navier-stokes equations, considered as a set of nonlinear partial differential equations derived from the newton's laws that describe the motion of fluids substances by accounting for the effects of pressure gradients, viscous and external forces.

Those equations are essential for predicting the fluid behavior (laminar or turbulent) it can be expressed as follows [34] [32]:

$$\rho \frac{dV}{dt} = \rho g - \nabla p - \frac{2}{3} \nabla(\mu \nabla \cdot V) + \nabla[\mu(\nabla \cdot V + (\nabla \cdot V)^T)] \quad (\text{II. 15})$$

Also, in its indicial form it can be written as follows:

$$\rho \left( \frac{\partial V_i}{\partial t} + V_j \frac{\partial V_i}{\partial x_j} \right) = \rho g_i - \frac{\partial P}{\partial x_i} - \frac{2}{3} \frac{\partial}{\partial x_i} \left( \mu \frac{\partial V_j}{\partial x_j} \right) + \frac{\partial}{\partial x_j} \left[ \mu \left( \frac{\partial V_i}{\partial x_j} + \frac{\partial V_j}{\partial x_i} \right) \right] \quad (\text{II. 16})$$

The equations in cylindrical form become:

✓ **Radial momentum equation**

$$\begin{aligned} \rho \left( \frac{\partial V_r}{\partial t} + V_r \frac{\partial V_r}{\partial r} + \frac{V_\theta}{r} \frac{\partial V_r}{\partial \theta} + V_z \frac{\partial V_r}{\partial Z} - \frac{V_\theta^2}{r} \right) &= \rho g_r - \frac{\partial P}{\partial r} + \frac{\partial}{\partial r} \left[ \mu \left( -\frac{2}{3} \nabla \cdot \vec{V} + 2 \frac{\partial V_r}{\partial r} \right) \right] \\ &+ \frac{1}{r} \frac{\partial}{\partial \theta} \left[ \mu \left( \frac{1}{r} \frac{\partial V_r}{\partial \theta} + \frac{\partial V_\theta}{\partial r} \right) \right] + \frac{\partial}{\partial Z} \left[ \mu \left( \frac{\partial V_r}{\partial Z} + \frac{\partial V_z}{\partial r} \right) \right] + \frac{2\mu}{r} \left( \frac{\partial V_r}{\partial r} - \frac{1}{r} \frac{\partial V_r}{\partial \theta} - \frac{V_r}{r} \right) \end{aligned} \quad (\text{II. 17})$$

✓ **Azimuthal momentum equation**

$$\begin{aligned} \rho \left( \frac{\partial V_\theta}{\partial t} + V_r \frac{\partial V_\theta}{\partial r} + \frac{V_\theta}{r} \frac{\partial V_\theta}{\partial \theta} + V_z \frac{\partial V_\theta}{\partial Z} + \frac{V_\theta V_r}{r} \right) &= \rho g_\theta - \frac{1}{r} \frac{\partial P}{\partial \theta} \\ &+ \frac{1}{r} \frac{\partial}{\partial \theta} \left[ \mu \left( -\frac{2}{3} \nabla \cdot \vec{V} + \frac{2}{r} \frac{\partial V_\theta}{\partial \theta} + \frac{2V_r}{r} \right) \right] + \frac{2\mu}{r} \left( \frac{1}{r} \frac{\partial V_r}{\partial \theta} - \frac{1}{r} \frac{\partial V_\theta}{\partial r} - \frac{V_\theta}{r} \right) \\ &+ \frac{\partial}{\partial Z} \left[ \mu \left( \frac{\partial V_\theta}{\partial Z} + \frac{1}{r} \frac{\partial V_z}{\partial \theta} \right) \right] + \frac{\partial}{\partial r} \left( \mu \left( \frac{\partial V_\theta}{\partial r} + \frac{1}{r} \frac{\partial V_r}{\partial \theta} - \frac{V_\theta}{r} \right) \right) \end{aligned} \quad (\text{II. 18})$$

✓ **Axial momentum equation**

$$\begin{aligned} \rho \left( \frac{\partial V_z}{\partial t} + V_r \frac{\partial V_z}{\partial r} + \frac{V_\theta}{r} \frac{\partial V_z}{\partial \theta} + V_z \frac{\partial V_z}{\partial Z} \right) &= \rho g_z - \frac{\partial P}{\partial Z} + \frac{\partial}{\partial Z} \left[ \mu \left( -\frac{2}{3} \nabla \cdot \vec{V} + 2 \frac{\partial V_z}{\partial Z} \right) \right] \\ &+ \frac{1}{r} \frac{\partial}{\partial \theta} \left[ \mu \left( \frac{\partial V_z}{\partial \theta} + \frac{\partial V_\theta}{\partial Z} \right) \right] + \frac{\partial}{\partial r} \left[ \mu \left( \frac{\partial V_r}{\partial Z} + \frac{\partial V_z}{\partial r} \right) \right] + \frac{\mu}{r} \left( \frac{\partial V_r}{\partial Z} + \frac{\partial V_z}{\partial r} \right) \end{aligned} \quad (\text{II. 19})$$

### III.3 Energy equation

The energy equation illustrates the mathematical formulation of the energy conservation principle. It claims that the rate of energy influx into a volume of a moving fluid is equivalent to the rate at which the fluid performs work on its surroundings. In addition to the rate of energy increase within the fluid itself. The energy contained in a moving fluid encompasses internal energy, flow energy, kinetic energy, and potential energy. Its general form is expressed as [36]:

$$\dot{Q} - \dot{W}_s - \dot{W}_v = \frac{\partial}{\partial t} \left( \int_{CV} e \rho dV \right) + \int_{CS} \rho (\mathbf{V} \cdot \mathbf{n}) \left( e + \frac{p}{\rho} \right) dA \quad (\text{II. 20})$$

Following a bunch of simplifying assumptions as follows [33]:

- No shaft work:  $\dot{W}_s = 0$
- The viscous work represented as a dissipation

$$\dot{W}_v = \int_{CV} \phi dV \quad (\text{II. 21})$$

- Fourier's law for heat conduction:

$$\mathbf{q} = -k \nabla T \quad (\text{II. 22})$$

- Conversion of the integral into differential form
- Compressible Newtonian fluid.

These simplifications result in the following energy equation [34] [32]:

$$\rho C_P \frac{dT}{dt} = \rho \dot{q}_g + \nabla \cdot (k \nabla T) + \beta T \frac{DP}{Dt} + \varrho \quad (\text{II. 23})$$

with:

$$\varrho = \left( -\frac{2}{3} \mu \nabla \cdot \mathbf{V} + \mu [\nabla \mathbf{V} + (\nabla \mathbf{V})^T] \right) : \nabla \cdot \vec{\mathbf{V}} \quad (\text{II. 24})$$

where:

- $\rho C_P \frac{dT}{dt}$  is the material derivative of the specific energy.
- $\rho \dot{q}_g$  is the volumetric heat source term.
- $\nabla \cdot (k \nabla T)$  is the divergence of the conductive heat flux.
- $\varrho$  is the dissipation function.
- $: \nabla \cdot \vec{\mathbf{V}}$  is the tensor operation that sums products of corresponding components.

**In its indicial form:**

$$\rho C_p \left( \frac{dT}{dt} + V_i \frac{\partial T}{\partial x_i} \right) = \rho \dot{q}_g + \frac{\partial}{\partial x_i} \left( k \frac{\partial T}{\partial x_i} \right) + \beta T \left( \frac{\partial P}{\partial t} + V_i \frac{\partial P}{\partial x_i} \right) + \phi \quad (\text{II. 25})$$

In its cylindrical form, it can be expressed as follows [32]:

$$\begin{aligned} \rho C_p \left( \frac{\partial T}{\partial t} + V_r \frac{\partial T}{\partial r} + \frac{V_\theta}{r} \frac{\partial T}{\partial \theta} + V_z \frac{\partial T}{\partial Z} \right) = & \rho \dot{q}_g + \frac{1}{r} \frac{\partial}{\partial r} \left( kr \frac{\partial T}{\partial r} \right) + \frac{1}{r^2} \frac{\partial}{\partial \theta} \left( k \frac{\partial T}{\partial \theta} \right) + \frac{\partial}{\partial Z} \left( k \frac{\partial T}{\partial Z} \right) \\ & + \beta T \left( \frac{\partial P}{\partial t} + V_r \frac{\partial P}{\partial r} + \frac{V_\theta}{r} \frac{\partial P}{\partial \theta} + V_z \frac{\partial P}{\partial Z} \right) + \phi \end{aligned} \quad (\text{II. 26})$$

Where the viscous dissipation is written as [32]:

$$\begin{aligned} \phi = 2\mu \left[ \left( \frac{\partial V_r}{\partial r} \right)^2 + \left( \frac{1}{r} \frac{\partial V_\theta}{\partial \theta} + \frac{V_r}{r} \right)^2 + \left( \frac{\partial V_z}{\partial Z} \right)^2 \right] - \frac{2}{3} \mu \left( \frac{1}{r} \frac{\partial(rV_r)}{\partial r} + \frac{1}{r} \frac{\partial V_\theta}{\partial \theta} + \frac{\partial V_z}{\partial Z} \right)^2 \\ + \mu \left[ \left( \frac{1}{r} \frac{\partial V_r}{\partial \theta} + \frac{\partial V_\theta}{\partial r} - \frac{V_\theta}{r} \right)^2 + \left( \frac{\partial V_\theta}{\partial Z} + \frac{1}{r} \frac{\partial V_z}{\partial \theta} \right)^2 + \left( \frac{\partial V_z}{\partial r} + \frac{\partial V_r}{\partial Z} \right)^2 \right] \end{aligned} \quad (\text{II. 27})$$

After multiple developments and simplifications defined as:

$$\checkmark \quad \text{Steady state } \frac{\partial}{\partial t} = 0$$

The equation system becomes:

$$\frac{1}{r} \frac{\partial}{\partial r} (r \rho V_r) + \frac{1}{r} \frac{\partial}{\partial \theta} (\rho V_\theta) + \frac{\partial}{\partial Z} (\rho V_z) = 0 \quad (\text{II. 28})$$

The Navier-Stokes equations become:

$$\begin{aligned} \rho \left( V_r \frac{\partial V_r}{\partial r} + \frac{V_\theta}{r} \frac{\partial V_r}{\partial \theta} + V_z \frac{\partial V_r}{\partial Z} - \frac{V_\theta^2}{r} \right) = & \rho g_r - \frac{\partial P}{\partial r} + \frac{\partial}{\partial r} \left[ \mu \left( -\frac{2}{3} \nabla \cdot \vec{V} + 2 \frac{\partial V_r}{\partial r} \right) \right] \\ & + \frac{1}{r} \frac{\partial}{\partial \theta} \left[ \mu \left( \frac{1}{r} \frac{\partial V_r}{\partial \theta} + \frac{\partial V_\theta}{\partial r} \right) \right] + \frac{\partial}{\partial Z} \left[ \mu \left( \frac{\partial V_r}{\partial Z} + \frac{\partial V_z}{\partial r} \right) \right] + \frac{2\mu}{r} \left( \frac{\partial V_r}{\partial r} - \frac{1}{r} \frac{\partial V_r}{\partial \theta} - \frac{V_r}{r} \right) \end{aligned} \quad (\text{II. 29})$$

$$\begin{aligned} \rho \left( V_r \frac{\partial V_\theta}{\partial r} + \frac{V_\theta}{r} \frac{\partial V_\theta}{\partial \theta} + V_z \frac{\partial V_\theta}{\partial Z} + \frac{V_\theta V_r}{r} \right) = & \rho g_\theta - \frac{1}{r} \frac{\partial P}{\partial \theta} \\ & + \frac{1}{r} \frac{\partial}{\partial \theta} \left[ \mu \left( -\frac{2}{3} \nabla \cdot \vec{V} + \frac{2}{r} \frac{\partial V_\theta}{\partial \theta} + \frac{2V_r}{r} \right) \right] + \frac{2\mu}{r} \left( \frac{1}{r} \frac{\partial V_r}{\partial \theta} - \frac{1}{r} \frac{\partial V_\theta}{\partial r} - \frac{V_\theta}{r} \right) \\ & + \frac{\partial}{\partial Z} \left[ \mu \left( \frac{\partial V_\theta}{\partial Z} + \frac{1}{r} \frac{\partial V_z}{\partial \theta} \right) \right] + \frac{\partial}{\partial r} \left( \mu \left( \frac{\partial V_\theta}{\partial r} + \frac{1}{r} \frac{\partial V_r}{\partial \theta} - \frac{V_\theta}{r} \right) \right) \end{aligned} \quad (\text{II. 30})$$



$$\rho \left( V_r \frac{\partial V_z}{\partial r} + \frac{V_\theta}{r} \frac{\partial V_z}{\partial \theta} + V_z \frac{\partial V_z}{\partial z} \right) = \rho g_z - \frac{\partial P}{\partial z} + \frac{\partial}{\partial z} \left[ \mu \left( -\frac{2}{3} \nabla \cdot \vec{V} + 2 \frac{\partial V_z}{\partial z} \right) \right] + \frac{1}{r} \frac{\partial}{\partial \theta} \left[ \mu \left( \frac{\partial V_z}{\partial \theta} + \frac{\partial V_\theta}{\partial z} \right) \right] + \frac{\partial}{\partial r} \left[ \mu \left( \frac{\partial V_r}{\partial z} + \frac{\partial V_z}{\partial r} \right) \right] + \frac{\mu}{r} \left( \frac{\partial V_r}{\partial z} + \frac{\partial V_z}{\partial r} \right) \quad (\text{II. 31})$$

**The energy equation:**

$$\rho C_p \left( V_r \frac{\partial T}{\partial r} + \frac{V_\theta}{r} \frac{\partial T}{\partial \theta} + V_z \frac{\partial T}{\partial z} \right) = \rho \dot{q}_g + \frac{1}{r} \frac{\partial}{\partial r} \left( k r \frac{\partial T}{\partial r} \right) + \frac{1}{r^2} \frac{\partial}{\partial \theta} \left( k \frac{\partial T}{\partial \theta} \right) + \frac{\partial}{\partial z} \left( k \frac{\partial T}{\partial z} \right) + \beta T \left( \frac{\partial P}{\partial t} + V_r \frac{\partial P}{\partial r} + \frac{V_\theta}{r} \frac{\partial P}{\partial \theta} + V_z \frac{\partial P}{\partial z} \right) + \varrho \quad (\text{II. 32})$$

Knowing that the viscous dissipation remains unchanged and the following term is expressed as:

$$\nabla \cdot \vec{V} = \frac{1}{r} \frac{\partial}{\partial r} (r \rho V_r) + \frac{1}{r} \frac{\partial}{\partial \theta} (\rho V_\theta) + \frac{\partial}{\partial z} (\rho V_z) \quad (\text{II. 33})$$

### III.4 The angular momentum equation

By analyzing the linear momentum equation described in (eq N°33), it is noticeable that it measures the net forces that cause the acceleration of the fluid in translation.

On the other hand, the angular momentum formula (eq N°34) used the position vector ‘**r**’ from a chosen reference axis of rotation to calculate and deduce the torque responsible for rotational acceleration in fluid systems, it is essential for turbomachinery (e.g., turbines) [2].

For the linear momentum equation, according to YUNUS ÇENGEL, it can be written as:

$$\Sigma \vec{F} = \int_{CV} \frac{\partial}{\partial t} (\rho \times \vec{V}) dV + \int_{CS} (\rho \times \vec{V}) (\vec{n} \times \vec{V}) dA \quad (\text{II. 34})$$

Where, the first term on the right represents the unsteady change of linear momentum, the second term accounts for the momentum carried into & out of the control volume by the fluid flow. While for the angular momentum equation, the moment of force about point O or also called the net torque and can be denoted as [31]:

$$\Sigma \vec{M} = \Sigma (\vec{r} \times \vec{F}) \quad (\text{II. 35})$$

With a magnitude of:

$$M = F \times r \times \sin \theta \quad (\text{II. 36})$$

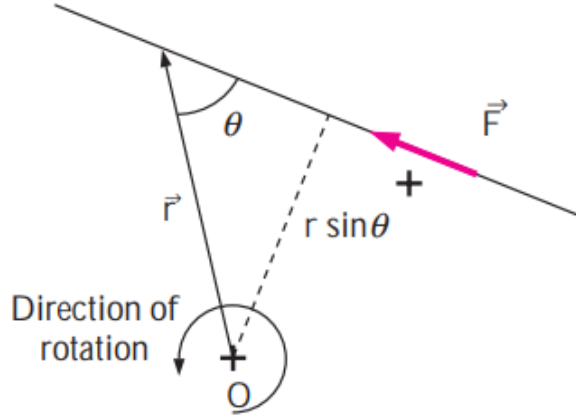


**Figure II.5:** Representation of vector forces [31].

With, theta the angle between  $\vec{r}$  and  $\vec{F}$ , noting that any force that acts through O is equal to none. Introducing the angular momentum or alternatively known as ‘the moment of a momentum’, which is expressed as:

$$\vec{H} = \vec{r} \times (m\vec{V}) \quad (\text{II. 37})$$

And for a system:

$$\vec{H}_{\text{sys}} = \int_{\text{Sys}} (\vec{r} \times \vec{V}) \rho dV \quad (\text{II. 38})$$

So, the conservation law of this moment for both control volume and surface can be called the general angular momentum formulation which is denote as:

$$\Sigma \vec{M} = \frac{d\vec{H}_{\text{sys}}}{dt} = \int_{\text{CV}} \frac{\partial}{\partial t} (\vec{r} \times \vec{V}) \rho dV + \int_{\text{CS}} (\vec{r} \times \vec{V}) \rho (\vec{n} \times \vec{V}) dA \quad (\text{II. 39})$$

Also, on a control volume, both body and surface forces can be observed, including gravity or pressure and contact reactions at the CV boundaries. The net torque is composed of both moments resulting from these forces and externally applied torques.

Building on the principle of angular momentum, Euler’s equation explains how turbomachinery transfers energy. The torque on fluid in a rotor depends on its entry/exit distances from  $r_1$  and  $r_2$  and some key properties like density and flow rate. Through tracking fluid’s

swirling motion changes, calculating power exchange is possible through turning rotational force into energy [30][31].

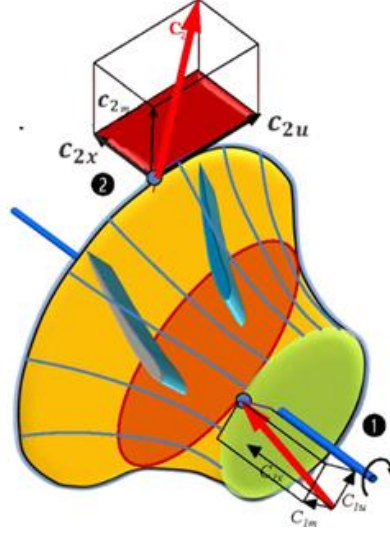


**Figure II.6:** Rotor schematic and Euler equation [2].

For a steady state, unidirectional flow, equation (II.) can be reduced to:

$$M = \int_S r \rho V V dA \quad (\text{II. 40})$$

Then

$$M = r_2 \rho_2 V_2 Q_2 - r_1 \rho_1 V_1 Q_1 \quad (\text{II. 41})$$

Knowing that, from the mass conservation equation (explained in the section down below) the term  $Q_2 \rho_2$  can be reduced the actual mass flow  $\dot{m}$ . So, equation (II.) can be reduced to:

$$M = \dot{m}(r_2 V_2 - r_1 V_1) \quad (\text{II. 42})$$

Also, the power generated by the rotation of the rotor at a speed denoted  $\omega$  and knowing that  $U = r\omega$ , Euler's turbine equation is finally expressed as:

$$\dot{W} = \dot{m}(U_2 C_{2u} - U_1 C_{1u}) \quad (\text{II. 43})$$

For an axial turbine:

$$\dot{W} = \dot{m}U(C_{2U} - C_{1U}) \quad (\text{II. 44})$$

From ‘figure.6’, the notations  $C_{2U}$  and  $C_{1U}$  replaced  $C_{\theta 2}$  and  $C_{\theta 1}$  , reflecting a shift of conventions from Dixon’s to the standard adopted notations at Our university. Alternatively, the expression can be written as [30][31]:

$$\Delta h_0 = U(C_{2U} - C_{1U}) > 0 \quad (\text{II. 45})$$

Or

$$h_{01} - h_{02} = U(C_{2U} - C_{1U}) \quad (\text{II. 46})$$

Where:

- $U_1$  and  $U_2$  are the rotor inlet and outlet velocities
- $c_{\theta 1}$  and  $c_{\theta 2}$  are the tangential components of the absolute velocities
- $h_{01}$  and  $h_{02}$  represent the total enthalpy at inlet and outlet

### III.5 Turbine design parameters

The geometry of turbine velocity triangles is described by three dimensionless fundamental parameters that are crucial in setting up initial turbine stage design.

### III.6 The flow coefficient

The flow coefficient in compressible flow machines is defined as the ratio of the average meridional velocity to the mean blade speed, this parameter can be considered alongside other nondimensional parameters to fully determine the operating conditions for ideal gas applications [37][30].

$$\varphi = \frac{C_x}{u} \quad (\text{II. 47})$$

For an ideal gas

$$\varphi = \frac{\rho_0 R_{cst} T_0}{P_0} \times \frac{C_x}{u} = \frac{\sqrt{R_{cst} T_0}}{U} \times \frac{\rho_0 C_x \sqrt{R_{cst} T_0}}{P_0} \quad (\text{II. 48})$$

Also

$$\varphi = \frac{\sqrt{R_{cst} T_0}}{U} \times \frac{\dot{m} \sqrt{R_{cst} T_0}}{A P_0} \quad (\text{II. 49})$$

### III.7 The stage loading coefficient

The stage loading coefficient is a dimensionless parameter that quantifies the actual energy transfer occurring within a turbine stage. Unlike the head coefficient used in hydraulic machines, it reflects the genuine change in enthalpy rather than the maximum isentropic work achievable. [37] [30]

$$\psi^* = \frac{W_e}{U^2} = \frac{h_{03} - h_{01}}{U^2} = \frac{\Delta h_0}{U^2} = \eta_s \frac{Dh_{0s}}{U^2} \quad (\text{II. 50})$$

**important notes:**

- ✓ for a turbine, the loading coefficient is always positive
- ✓ for a gas turbine, the loading coefficient superior to 1.5 indicates that the blades are heavily charged, while when it's inferior to 1, the blades are lightly charged [30][84].

### III.8 The reaction degree

The degree of reaction characterizes how the fluid's pressure drop is distributed between the rotor and stator. Since energy transfer involves forms of energy beyond pressure such as kinetic energy, a more comprehensive definition incorporates enthalpy to capture the full scope of the stage energy exchange [30][35]. It can be expressed as follows:

$$R = \frac{\text{enthalpy variation in the rotor}}{\text{enthalpy variation for the full stage}}$$

With

$$R = \frac{\Delta h_r}{\Delta h_s} = \frac{h_3 - h_2}{h_3 - h_1} \quad (\text{II. 51})$$

This equation can be further simplified to be expressed down below as [30]:

$$R = \frac{\Delta h_r}{\Delta h_s} = 1 - \frac{(C_3^2 - C_2^2)/2}{2(U_3 C_{3u} - U_2 C_{2u})} \quad (\text{II. 52})$$

Also, since

$$U_3 = U_2 = U \text{ and } C^2 = C_x^2 + C_u^2$$

The reaction degree can be written as:

$$R = 1 - \frac{C_{3u} + C_{2u}}{2U} = \frac{W_3^2 - W_2^2}{2\psi^*U^2} \quad (\text{II.53})$$

For a fixed stage loading and flow coefficients, only the degree of reaction varies which directly governs the blade geometry, it distinguishes 2 main turbine configurations or styles:

### ➤ Impulse turbines

Also called zero reaction turbines where the entire pressure drops in the stator, while the rotor barely extracts kinetic energy which varies the geometry between the stator and the rotor [30].

### ➤ Reaction turbines

The pressure drops mainly in a split way between both blades leading to a symmetrical blade geometry [30].

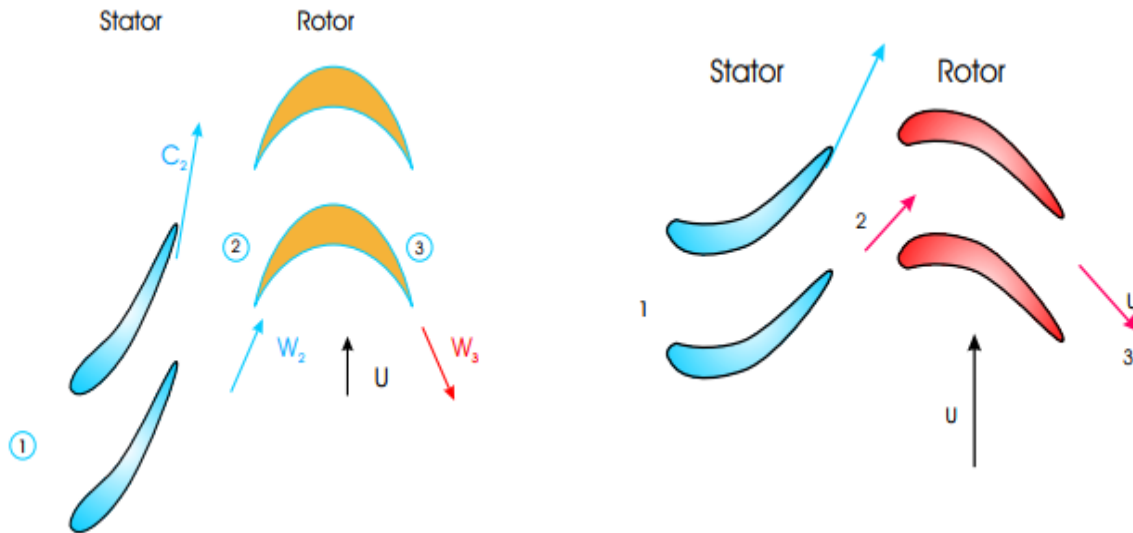


**Figure II.7: left-Impulse turbine cascade, right-Reaction turbine cascade velocity triangles [30].**

## III.9 Smith chart

Smith et al. were the first to examine how stage loading and flow coefficient affect turbine performance by analyzing a vast database from Rolls-Royce gas turbines. Their findings led to the development of the ‘**Smith Chart**’.

This chart, based on turbines with 0 tip clearance, illustrates that for a given stage loading, reducing the flow coefficient can enhance efficiency. This improvement is attributed to reduced turning, which results in taller blades with higher aspect ratios, thereby minimizing secondary losses. Conversely, higher flow coefficients correspond to shorter blades, leading to increased losses [38].

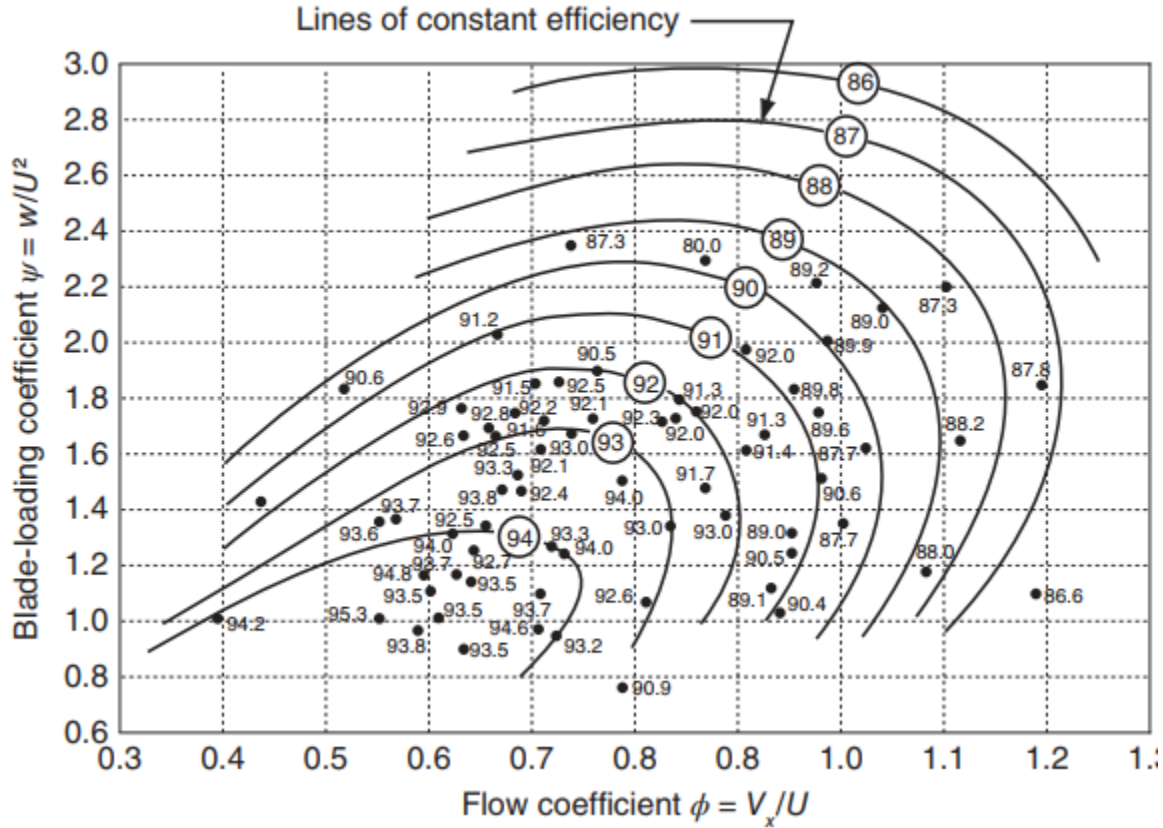


**Figure II.8:** The Smith chart for turbomachinery [39].

According to Korpela, «The flow coefficients in the range of  $0.6 \leq \phi \leq 1$  give uncorrected efficiencies in a range from 90% to 94%, depending on how heavily loaded the blades are. Typical turbines have a blade-loading coefficient in the range of  $1.5 \leq \psi \leq 2.2$ , but there are designs outside this range». (Korpela, 2019, p.285).

#### IV. Thermodynamic recap and Efficiency

Thermodynamics examines how a system shifts between equilibrium states, often visualized on surfaces defined by pressure, temperature, and also volume. For an ideal reversible process from point 1 to point 2 for example, the system remains in equilibrium at every step.

## CHAPTER II

---

However, for a real process which is generally irreversible causes an increase in something called entropy and an energy quality reduction. This concept determines why no transformation of energy is fully efficient and why returning a system to its initial state entails losses [40].

For an ideal gas, total enthalpy which is defined down below, is the starting point for a well-known equation that frequently links the stagnation and static temperatures [40] [41]:

$$h_0 = h + \frac{V^2}{2} \rightarrow C_p T_0 = C_p T + \frac{V^2}{2} \quad (\text{II. 54})$$

Which gives us:

$$T_0 = T + \frac{V^2}{2C_p} \quad (\text{II. 55})$$

Knowing that:

$$\alpha = \sqrt{\gamma R_{cst} T} \text{ and } C_p = \frac{\gamma R_{cst}}{\gamma - 1}$$

The final equation of the temperature ratio is:

$$\frac{T_0}{T} = 1 + \frac{(\gamma - 1)V^2}{2 \cdot a^2} = 1 + \frac{(\gamma - 1) \times Ma^2}{2} \quad (\text{II. 56})$$

Where M is the well-known Mach number. And for an isentropic process, other ratios can be defined:

$$\frac{P_0}{P} = \left( \frac{T_0}{T} \right)^{\frac{\gamma}{(\gamma-1)}} = \left( 1 + \frac{(\gamma - 1) \times Ma^2}{2} \right)^{\frac{\gamma}{(\gamma-1)}} \quad (\text{II. 57})$$

$$\frac{\rho_0}{\rho} = \left( \frac{T_0}{T} \right)^{\frac{1}{(\gamma-1)}} = \left( 1 + \frac{(\gamma - 1) \times Ma^2}{2} \right)^{\frac{1}{(\gamma-1)}} \quad (\text{II. 58})$$

### IV.1 Gas properties:

Since all the parameters change throughout a turbine, it is vital to examine the behavior of the working fluid (air in this case), the perfect gas concept is adopted which states that the relationship between pressure, volume and mass is given by [42]:



$$P \times V = m \times R_{\text{cst}} \times T \quad (\text{II. 59})$$

Where  $R_{\text{cst}}=8.314 \text{ J/mol}\cdot\text{K}$  is the universal specific gas constant that is equal to:

$$R_{\text{cst}} = C_p - C_v \quad (\text{II. 60})$$

With

$$C_p = \left( \frac{\partial h}{\partial T} \right)_p \text{ and } C_v = \left( \frac{\partial h}{\partial T} \right)_v \quad (\text{II. 61})$$

## IV.2 Efficiency formulations

Efficiency of a turbine refers to how a turbine converts the energy of the fluid effectively into work. It is simply a measure of actual work done as opposed to ideal work done in an ideal case. To researchers like Dixon, Kadambi, and Regio, the measure informs us about how much energy is being converted successfully with allowance for losses due to friction, turbulence for example. In particular, total-to-total efficiency compares the actual drop in total enthalpy to it's ideal, while the total-to-static focuses on the energy recovered at the outlet under static conditions. In this section, formulas for these 2 important parameters will be even further developed.

### IV.2.1 Total-to-total efficiency

In turbomachinery systems, the use of loss coefficients is essential to characterize and assess energy dispersion. These coefficients compute losses based on the total pressure drop across all components of the system. A general formulation for this coefficient for turbine application in the stator and the rotor can be expressed as [30]:

$$K_{\text{Stat}} = \frac{\Delta P_{0S}}{\rho C_2^2 / 2} \quad (\text{II. 62})$$

And

$$K_{\text{Rot}} = \frac{\Delta P_{0R}}{\rho W_3^2 / 2} \quad (\text{II. 63})$$

#### ❖ Total-to-Total efficiency formula:

The turbine efficiency as a function of total conditions is expressed as follows:

$$\eta_{tt} = \frac{\Delta h_0}{\Delta h_0 + \Delta h_{0P}} = \frac{1}{1 + \left[ \frac{\Delta h_{0P}}{\Delta h_0} \right]} \quad (\text{II. 64})$$

- $\Delta h_0$  is the actual enthalpy variation
- $\Delta h_{0P}$  accounts for the energy dispersion due to losses which can approximated to:

$$\Delta h_{0P} \approx \frac{\Delta P_{0P}}{\rho} \quad (\text{II. 65})$$

And total pressure reduction can be written as

$$\Delta P_{0P} = \Delta P_{0PS} + \Delta P_{0PR} \quad (\text{II. 66})$$

The efficiency formulation becomes:

$$\eta_{tt} = \frac{1}{1 + \left[ \frac{\Delta P_{0PS} + \Delta P_{0PR}}{\rho \times \Delta h_0} \right]} \quad (\text{II. 67})$$

Introducing the loss coefficients and knowing that  $\psi = \frac{\Delta h_0}{U^2}$  gives us:

$$\eta_{tt} = \frac{1}{1 + \frac{1}{2\psi^*} \left( \frac{K_S \times C_2^2}{U^2} + \frac{K_R \times W_3^2}{U^2} \right)} \quad (\text{II. 68})$$

introducing some special axial turbine correlations [30]:

$$\frac{C_2}{U} = \sqrt{\phi^2 + \left( \frac{\psi^*}{2} + 1 - R \right)^2} \quad (\text{II. 69})$$

And

$$\frac{W_3}{U} = \sqrt{\phi^2 + \left( \frac{\psi^*}{2} + R \right)^2} \quad (\text{II. 70})$$

Finally, the Total-to-Total efficiency can be written as according to Reggio:

$$\eta_{tt} = \frac{1}{1 + \frac{1}{2\Psi^*} \left( K_S \left( \phi^2 + \left( \frac{\Psi^*}{2} + 1 - R \right)^2 \right) + K_R \left( \phi^2 + \left( \frac{\Psi^*}{2} + R \right)^2 \right) \right)} \quad (\text{II. 71})$$

And according to Dixon [43], the 2 formulations can be written as:

$$\eta_{tt} = \frac{1}{1 + \frac{\zeta_R W_3^2 + \zeta_N C_2^2 \cdot \frac{T_3}{T_2}}{2(h_1 - h_3)}} \quad (\text{II. 72})$$

$$\eta_{ts} = \frac{1}{1 + \frac{\zeta_R W_3^2 + \zeta_N C_2^2}{2(h_1 - h_3)}} \quad (\text{II. 73})$$

### IV.3 Entropy

Derived from the second law of thermodynamics. Entropy, is a measure of disorder, randomness, and chaos within a system. It describes how energy becomes less usable over-time as it spreads out and how evenly the energy and matter are distributed such as when a heat source flows over a cold one, the fast and hot moving molecules collide with the cold slower ones sharing the energy evenly until everything reaches equilibrium but that energy becomes too dispersed to be harnessed effectively. Entropy can never be conserved but only remains constant in reversible processes that don't exist outside the theoretical aspect. In real systems, friction, heat loss, and turbulence cause entropy generation which is irreversible and unavoidable. Entropy helps us understand why heat can't flow backward and why every energy has unavoidable waste. In simple terms, it's nature's way of shifting towards balance, but in doing so the process deviates from the ideal performance [44].

The below enthalpy-entropy diagram of the full turbine expansion confirms the definition given in this section, where the maximum efficiency occurs during the ideal path from 1-2s or 2s-3s or even 1-3s since level 2 is just an intermediate stat with a maximum enthalpy drop  $\Delta h_s$  that means the highest work output. The actual real path on the contrary, shows a deviation due to entropy generation with a lower enthalpy drop and less useful output.

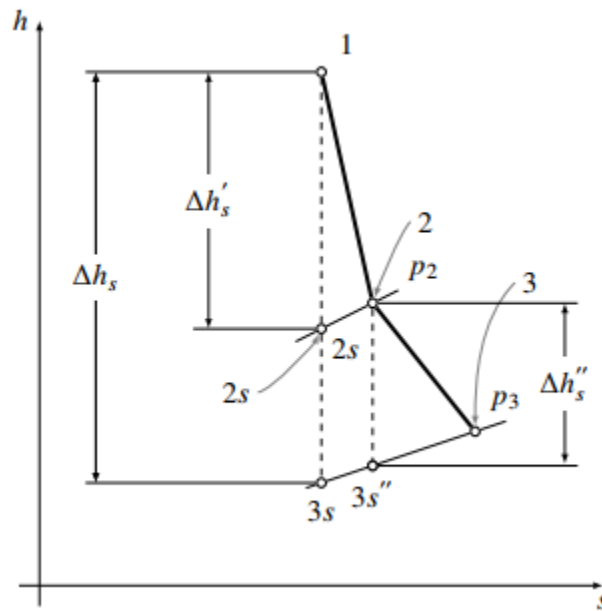


**Figure II.9:** h-s diagram of a turbine stage [38].

#### IV.4 Boundary layers

A boundary layer is a thin region of the fluid near a solid surface (blade) where the velocity of the fluid changes from zero at the surface to stream velocity once you're away from the surface, the boundary layer thickness and behavior depend on the Reynolds number. Based on this, the displacement thickness which represents how much the boundary layer displaces to the outer region can be estimated with the following formula [8]:

$$\frac{\delta^*}{X} = \frac{Cst}{Re_x^N} \quad (II. 74)$$

With:

- $X$  is the distance from the edge of the surface.
- $Cst$  and  $N$ : constants that depend on the flow regime:
  - ✓ Turbulent flow:  $C=0.045$ ,  $N=1/5$
  - ✓ Laminar flow:  $C=1.72$ ,  $N=0.5$
- $\delta^*$  is the boundary thickness.

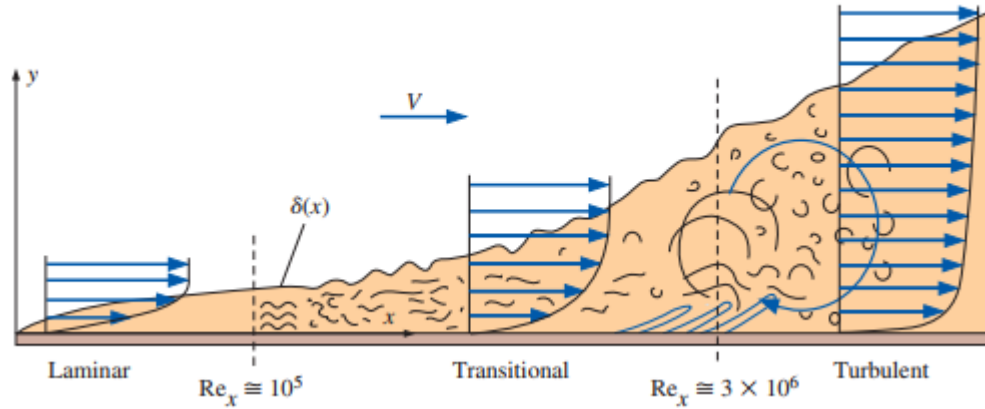


**Figure II.10:** flow regime and layer thickness [8].

## V. Turbulence

### V.1 Historical and theoretical perspectives on turbulence

Turbulence has intrigued scholars for centuries, starting from the sketching of Leonardo da Vinci on which he captured the swirling and chaotic nature of fluid motion to Richardson (1922) [45] who famously summarized the energy cascade with the phrase “big whorls have little whorls”, indicating how large eddies break down into smaller ones which each a concept that remains central to understanding turbulence nowadays.

In more recent years, the mathematical concept of turbulence has been explored. Von-Karman and Taylor (1937) [46] characterized turbulence as a chaotic and irregular movement within fluids, typically arising when fluid streams interact with obstacles or with each other. Expanding on this foundation, chapman and Tobak (1985) [47] provided a more comprehensive definition, describing turbulence as a chaotic solution to the three-dimensional Navier-Stokes equations. They emphasized that turbulence is extremely sensitive to initial conditions and evolves through a series of instabilities that emerge from laminar flow. J.O. Heinz [48] came up with even a better explanation of turbulence as follows: “Turbulent fluid motion is an irregular condition of the flow in which quantities show a random variation with time and space coordinates, so that statistically distinct average values can be discerned”. J.O. Heinz (1959).



**Figure II.9:** Laminar to turbulent transition example [49].

### V.2 Statistical and structural definitions of turbulence

- ✓ **Statistical perspective:** turbulence is commonly analyzed by decomposing the instantaneous flow into a steady mean and random fluctuations. This method, referred to as Reynolds-Averaging method, highlights important elements such as turbulent kinetic energy and a range of statistical measures [50].
- ✓ **Structural perspective:** turbulence can be understood through the lens of coherent structures such as eddies and vortices. These formations emerge within the chaotic flow, illustrating the organization of energy as it transitions from larger scales to smaller ones.

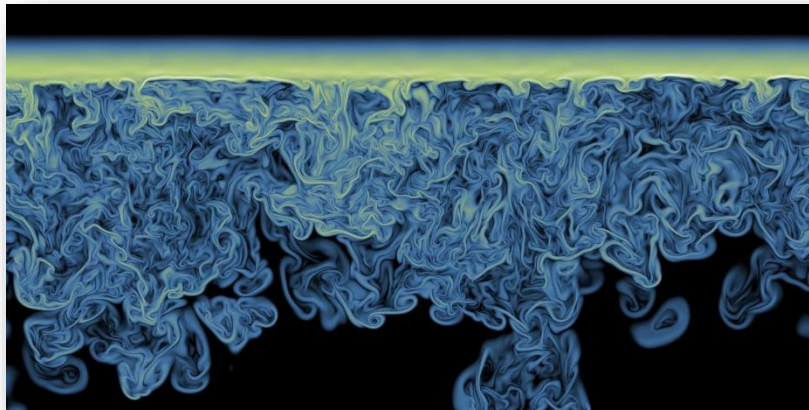


**Figure II.10:** example of a chaotic flow [51].

### V.3 Characteristics of turbulence

- ✓ **Irregularity:** these flows are characterized by unpredictability, showcasing random and chaotic variations.
- ✓ **Diffusivity:** turbulence plays a crucial role in enhancing the mixing process, thereby increasing the rates of momentum, heat, and mass transfer.
- ✓ **High Reynolds number:** turbulence typically arises when inertial forces dominate over viscous forces.
- ✓ **Three-dimensionality:** while turbulent flows may sometimes seem 2D on average, their fluctuations are fundamentally 3D.
- ✓ **Dissipation:** the viscous effects present in turbulence convert kinetic energy into thermal energy.
- ✓ **Continuum behavior:** even the smallest turbulent eddies are significantly larger than molecular scales, permitting the flow to be treated as a continuous medium [52].

### V.4 Turbulence applications

Turbulence can be found in multiple applications such as industrial processes to optimize reactors, heat exchangers, it can also be found in aerospace engineering to ensure stability and efficient aircraft by the prediction of flow around the wings and fuselages. It can also improve wind turbine and renewable system efficiency throughout simulations, and for climate modeling to forecast atmospheric circulation and pollutant transport. It can also help with the aerodynamic design of equipment like golf balls and tennis rackets in the sports domain or for environmental engineering [53].

### V.5 Turbulence approaches

Various methods can be employed to simulate turbulent flows. Each method presents its own set of benefits and drawbacks, and then selection of a particular approach is contingent upon the specific application and the required degree of precision. Some of the most usable approaches are explained down below [53]:

- **DNS:** addresses the complete Navier-Stokes equations without the use of turbulence models, providing high precision. However, this approach incurs significant computational expenses and is restricted to straightforward, low-Reynolds number flow scenarios.

- **LES:** addresses significant turbulent structures while simulating smaller scales, effectively capturing transient characteristics. However, this approach requires high grid resolution and considerable computational resources.
- **RANS:** which will further developed in the section down below, averages the turbulent flow to calculate the mean values through closure models, resulting in computational efficiency while maintaining ability to efficiently capture transient phenomena.
- **DES:** integrates RANS near the walls with LES in the outer flow to achieve a balance between efficiency and accuracy. However, it is sensitive to grid dependency and necessitates meticulous adjustment of model constants.

To better understand which method to choose at certain scenarios, the figure down below shows the ranking of the approaches compared to their efficiency and computational cost:

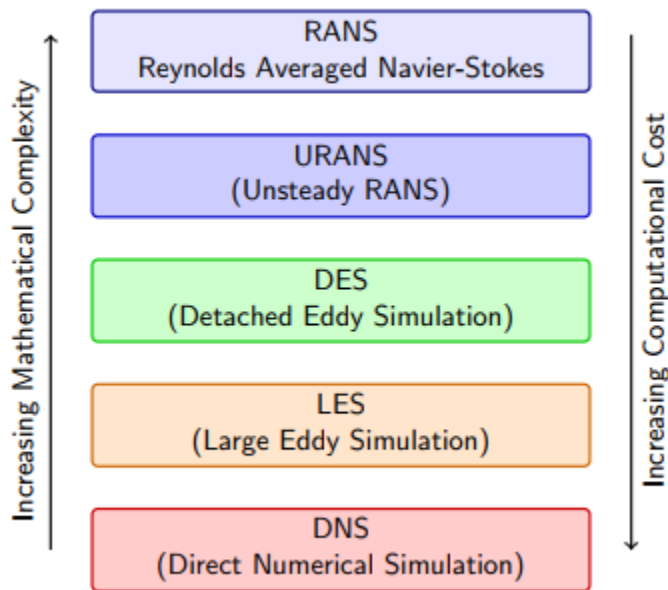


**Figure II.11:** overview of turbulence approaches [52].

## VI. Reynolds Averaging

Proposed by Reynolds, it is a technique for the approximation of turbulent flows by applying a decomposition of velocity and pressure variables into 2 components, one is called mean component with the overbar while the other the fluctuating component.



## CHAPTER II

---

This decomposition facilitates the resolution of the Navier-Stokes equations for mean values, these components can be expressed as follows [54]:

$$U_i = \bar{U}_i + U'_i \quad (\text{II. 75})$$

For pressure:

$$P_i = \bar{P}_i + P'_i \quad (\text{II. 76})$$

### VII. Favre mass averaging

Favre averaging is applied where there are considerable variations in flow density. Unlike Reynolds, Favre assigns weights to variables such as velocity based on local density. This averaging can be expressed as [55]:

$$\tilde{U}_i = \frac{\overline{\rho U_i}}{\bar{\rho}} \quad (\text{II. 77})$$

Respectively:

$$U_i = \bar{U}_i + U''_i \quad (\text{II. 78})$$

Where:

- $\overline{\rho U_i}$  and  $\bar{\rho}$  are Reynolds-averaged density and velocity.
- $U''_i$  the mass weighted fluctuation.

### VIII. Averaged equations

Substituting the variables from subsection (VII) it can be finally said that the averaged equations of the continuity, momentum, and energy for a compressible flow are written as follows [55]:

$$\frac{\partial \bar{\rho}}{\partial t} + \bar{\rho} \frac{\partial \bar{U}_i}{\partial x_i} = 0 \quad (\text{II. 79})$$

And

$$\frac{\partial}{\partial t} (\bar{\rho} \bar{U}_i) + \frac{\partial}{\partial x_j} (\bar{\rho} \tilde{U}_i \tilde{U}_j) = \frac{\partial}{\partial x_j} (\bar{\tau}_{ij} - \bar{\rho} \times \widetilde{U''_i U''_j}) - \frac{\partial \bar{P}}{\partial x_i} \quad (\text{II. 80})$$

$$\begin{aligned} \frac{\partial}{\partial t}(\bar{\rho}\tilde{E}) + \frac{\partial}{\partial x_j}(\bar{\rho}\tilde{U}_j\tilde{H}) = & \frac{\partial}{\partial x_j} \left( \underbrace{k \frac{\partial \tilde{T}}{\partial x_j}}_1 + \underbrace{\tau_{ij}\tilde{U}_i''}_2 - \underbrace{\bar{\rho}\tilde{U}_j''\tilde{K}}_3 - \underbrace{\bar{\rho} \times \tilde{U}_j''h''}_4 \right) \\ & + \frac{\partial}{\partial x_j} \left[ \tilde{U}_i \left( \underbrace{\tilde{\tau}_{ij}}_5 - \underbrace{\bar{\rho} \times \tilde{U}_i''\tilde{U}_j''}_6 \right) \right] \end{aligned} \quad (\text{II. 81})$$

## IX. The Boussinesq Approach

The Boussinesq hypothesis is a widely utilized approach for representing Reynolds stresses by relating them to mean velocity gradients through something called turbulent viscosity  $\mu_t$ . It is commonly found in famous closure models with a crucial advantage of maintaining low computational expenses, as it generally requires only a maximum of 2 equations for resolution. This hypothesis assumes that viscosity is anisotropic scalar, it is formulated as [54] [56]:

$$\underbrace{-\overline{\rho U_i' U_j'}}_{\text{Reynolds Stress}} = \mu_t \left( \frac{\partial U_i}{\partial x_j} + \frac{\partial U_j}{\partial x_i} \right) - \frac{2}{3} \left( \rho k + \mu \frac{\partial U_k}{\partial x_k} \right) \delta_{ij} \quad (\text{II. 82})$$

## X. The closure models

### X.1 Spalart-Allmaras Model

The Spalart-Allmaras model is a low Reynolds number and one-equation model originally developed for aerospace and turbomachinery applications, particularly for flow constrained by walls. It computes a modified turbulent viscosity  $\tilde{\nu}$  by solving a transport equation that accounts for both production and dissipation near walls. It requires a fine near-wall resolution, its Ansys CFX implementation now uses a wall-insensitive approach, enabling accurate predictions on coarser grids. While effective for aerodynamic boundary layers with adverse pressure gradients, it is less reliable for free shear flows and for predicting the decay of homogeneous turbulence. Its main equation is [54] [58]:

$$\frac{\partial}{\partial t}(\rho\tilde{\nu}) + \frac{\partial}{\partial x_i}(\rho\tilde{\nu}U_i) = G_v + \frac{1}{\sigma_{\tilde{\nu}}} \left[ \frac{\partial}{\partial x_j} \left\{ (\mu + \rho\tilde{\nu}) \times \frac{\partial \tilde{\nu}}{\partial x_j} \right\} + c_{b2} \times \rho \left( \frac{\partial \tilde{\nu}}{\partial x_j} \right) \right] - Y_v + S_{\tilde{\nu}} \quad (\text{II. 83})$$

Where:

- $G_v$  is the production of turbulent viscosity.
- $Y_v$  is the destruction of turbulent viscosity.
- $\sigma_{\tilde{v}}$  and  $c_{b2}$  are the constants.
- $\nu$  is the molecular viscosity.
- $S_{\tilde{v}}$  is the user defined source term.

## X.2 Two-equation models

### X.2.1 Standard k-epsilon model

This one is a two-equation model that employs two separate transport equations, one for turbulent kinetic energy ( $k$ ) and one for the dissipation rate epsilon ( $\epsilon$ ). Those 2 equations combined together are the key for independent determination of turbulent velocity and length scales. Based on theoretical and experimental insights, and assuming fully turbulent flows with negligible molecular viscosity, it is robust, efficient, and widely used in CFD applications. Also, it has multiple derived models like the RNG and realizable which will be further discussed in the subsections to come.

The transport equations for the kinetic energy ( $k$ ) and dissipation ( $\epsilon$ ) are [54] [59]:

$$\frac{\partial}{\partial t}(\rho k) + \frac{\partial}{\partial x_i}(\rho k U_i) = \frac{\partial}{\partial x_j} \left[ \left( \mu + \frac{\mu_t}{\sigma_k} \right) \frac{\partial k}{\partial x_j} \right] + G_k + G_b - \rho \epsilon - Y_M + S_k \quad (\text{II. 84})$$

And

$$\frac{\partial}{\partial t}(\rho \epsilon) + \frac{\partial}{\partial x_i}(\rho \epsilon U_i) = \frac{\partial}{\partial x_j} \left[ \left( \mu + \frac{\mu_t}{\sigma_\epsilon} \right) \frac{\partial \epsilon}{\partial x_j} \right] + C_{1\epsilon} \cdot \frac{\epsilon}{k} (G_k + C_{3\epsilon} G_b) - C_{2\epsilon} \cdot \rho \frac{\epsilon^2}{k} + S_\epsilon \quad (\text{II. 85})$$

While the turbulent viscosity is expressed as:

$$\mu_t = \rho \cdot C_\mu \left( \frac{k^2}{\epsilon} \right) \quad (\text{II. 86})$$

- $G_k$  and  $G_b$  are the generation of turbulent kinetic energy due to mean velocity and due to buoyancy.
- $Y_M$  represents the fluctuating dilatation to the overall dissipation.
- $S_k$  and  $S_\epsilon$  are user defined source terms

- $\sigma_\epsilon$  and  $\sigma_k$  are specific Prandtl numbers.
- $C_{1\epsilon}, C_{2\epsilon}, C_{3\epsilon}$  are constants.

The model constants utilized in ANSYS CFX are:

$$C_{1\epsilon} = 1.44, C_{2\epsilon} = 1.92, C_\mu = 0.09, \sigma_\epsilon = 1.0, \sigma_k = 1.3$$

### X.2.2 RNG k-epsilon model

This model, developed by Yakhot et al. using a renormalization group theory, refines the standard  $k - \epsilon$  formulation to better account for the effects of all turbulent scales. Unlike the standard model which computes eddy-viscosity from a single characteristic length scale; the RNG modifies the  $\epsilon$  equation by adding extra terms for adjustments, thereby incorporating contributions from smaller scales. It also offers an analytical expression for the turbulent Prandtl number and a differential formulation for effective viscosity that adapts to low Reynolds number cases when near wall regions are well resolved, making it more accurate for complex studies.

The transport equations for both  $k$  and  $\epsilon$  are [54] [60] [61]:

$$\frac{\partial}{\partial t}(\rho k) + \frac{\partial}{\partial x_i}(\rho k U_i) = \frac{\partial}{\partial x_j} \left[ \left( \alpha_k \mu_{\text{eff}} + \frac{\mu_t}{\sigma_k} \right) \frac{\partial k}{\partial x_j} \right] + G_k + G_b - \rho \epsilon - Y_M + S_k \quad (\text{II. 87})$$

And

$$\begin{aligned} \frac{\partial}{\partial t}(\rho \epsilon) + \frac{\partial}{\partial x_i}(\rho \epsilon U_i) = & \frac{\partial}{\partial x_j} \left[ \left( \alpha_\epsilon \mu_{\text{eff}} + \frac{\mu_t}{\sigma_\epsilon} \right) \frac{\partial \epsilon}{\partial x_j} \right] + C_{1\epsilon} \cdot \frac{\epsilon}{k} (G_k + C_{3\epsilon} G_b) \\ & - C_{2\epsilon} \cdot \rho \frac{\epsilon^2}{k} - R_\epsilon + S_\epsilon \end{aligned} \quad (\text{II. 88})$$

The turbulent viscosity is given as:

$$\mu_t = \rho \cdot C_\mu \left( \frac{k^2}{\epsilon} \right) \quad (\text{II. 89})$$

And the additional term is formulated as follows:

$$R_\epsilon = \frac{C_\mu \cdot \rho \cdot \eta^3 \left( 1 - \frac{\eta}{\eta_0} \right) \cdot \epsilon^2}{(1 + B\eta^3) \cdot k} \quad (\text{II. 90})$$

The equation for  $\varepsilon$  can be rearranged to:

$$\frac{\partial}{\partial t}(\rho\varepsilon) + \frac{\partial}{\partial x_i}(\rho\varepsilon U_i) = \frac{\partial}{\partial x_j} \left[ \left( \alpha_k \mu_{\text{eff}} + \frac{\mu_t}{\sigma_\varepsilon} \right) \frac{\partial \varepsilon}{\partial x_j} \right] + C_{1\varepsilon} \cdot \frac{\varepsilon}{k} (G_k + C_{3\varepsilon} G_b) - C_{2\varepsilon}^* \cdot \rho \frac{\varepsilon^2}{k} \quad (\text{II. 91})$$

Knowing that

$$C_{2\varepsilon}^* = C_{2\varepsilon} + \frac{C_\mu \cdot \eta^3 \left( 1 - \frac{\eta}{\eta_0} \right)}{(1 + \beta \eta^3)} \quad (\text{II. 92})$$

The model constants utilized in ANSYS CFX are:

$$C_{1\varepsilon} = 1.42, C_{2\varepsilon} = 1.68, C_\mu = 0.0845, \sigma_\varepsilon = 0.7194$$

$$\eta_0 = 4.38, \eta \approx 3.0, \beta = 0.012, C_{2\varepsilon}^* \approx 2.0, \sigma_k = 0.7194$$

### X.2.3 Realizable K-epsilon model

This model differs in two keys aspects, one is that it introduces a new formulation for turbulent viscosity. Second, it uses modified transport equation for  $(\varepsilon)$  derived from mean square vorticity. Also, the term realizable means that the model meets specific mathematical constraints on Reynolds stresses. These enhancements make the realizable  $k - \varepsilon$  model more accurate and reliable for complex flows cases.

The modeled transport equation of  $(k)$  and  $(\varepsilon)$  are [54] [62]:

$$\frac{\partial}{\partial t}(\rho k) + \frac{\partial}{\partial x_i}(\rho k U_i) = \frac{\partial}{\partial x_j} \left[ \left( \mu + \frac{\mu_t}{\sigma_k} \right) \frac{\partial k}{\partial x_j} \right] + G_k + G_b - \rho \varepsilon - Y_M + S_k \quad (\text{II. 93})$$

And

$$\frac{\partial}{\partial t}(\rho\varepsilon) + \frac{\partial}{\partial x_i}(\rho\varepsilon U_i) = \frac{\partial}{\partial x_j} \left[ \left( \mu + \frac{\mu_t}{\sigma_\varepsilon} \right) \frac{\partial \varepsilon}{\partial x_j} \right] + \rho C_1 S \varepsilon - \rho C_2 \frac{\varepsilon^2}{k + \sqrt{v\varepsilon}} + C_{1\varepsilon} \cdot \frac{\varepsilon}{k} C_{3\varepsilon} G_b + S_\varepsilon \quad (\text{II. 94})$$

Knowing that

$$C_1 = \max \left[ 0.43 \frac{n}{\eta + 5} \right], \eta = S \frac{k}{\varepsilon}, S = \sqrt{2 \times S_{ij} \times S_{ij}}$$

The turbulent viscosity is written as

$$\mu_t = \rho \cdot C_\mu \left( \frac{k^2}{\varepsilon} \right) \quad (\text{II. 95})$$

$C_\mu$ , is no longer considered a constant, the model constants utilized in ANSYS CFX are:

$$C_{1\varepsilon} = 1.44, C_2 = 1.9, \sigma_\varepsilon = 1.0, \sigma_k = 1.3$$

#### **X.2.4 Standard k-omega model**

The standard k –  $\omega$  model is a two-equation framework that generally surpasses the k –  $\varepsilon$  models, particularly in contexts involving wall bounded flows, free shear regions, and low Reynolds number conditions. This characteristic makes it especially proficient in managing complex boundary layers that encounter adverse pressure gradients and flow separation which is frequent in turbomachinery. Based on Wilcox's formulation and adjusted to account for low Reynolds effects, compressibility, and shear flow dispersion.

The turbulence kinetic energy (k) and the specific dissipation rate ( $\omega$ ) are denoted as [63] [64]:

$$\frac{\partial}{\partial t}(\rho k) + \frac{\partial}{\partial x_i}(\rho k U_i) = \frac{\partial}{\partial x_j} \left[ \Gamma_k \times \frac{\partial k}{\partial x_j} \right] + G_k + G_b - Y_k + S_k \quad (\text{II. 96})$$

And

$$\frac{\partial}{\partial t}(\rho \omega) + \frac{\partial}{\partial x_i}(\rho \omega U_i) = \frac{\partial}{\partial x_j} \left[ \Gamma_\omega \times \frac{\partial \omega}{\partial x_j} \right] + G_\omega + G_{\omega b} - Y_\omega + S_\omega \quad (\text{II. 97})$$

With the effective diffusivity

$$\begin{aligned} \Gamma_k &= \mu + \frac{\mu_t}{\sigma_k} \\ \Gamma_\omega &= \mu + \frac{\mu_t}{\sigma_\omega} \end{aligned} \quad (\text{II. 98})$$

Also

$$\mu_t = \alpha^* \frac{\rho k}{\omega} \quad (\text{II. 99})$$

The coefficient  $\alpha^*$  reduces the turbulent viscosity, providing a correction for low-Reynolds number effects:

$$\alpha^* = \alpha_\infty^* \left( \frac{\alpha_0^* + \frac{Re_t}{R_k}}{1 + \frac{Re_t}{R_k}} \right) = \alpha_\infty^* \left( \frac{\frac{\beta_i}{3} + \frac{Re_t}{R_k}}{1 + \frac{Re_t}{R_k}} \right) \quad (II. 100)$$

Also, the production of turbulence kinetic energy is formulated as:

$$G_k = \mu_t S^2 \quad (II. 101)$$

Where “S” is the magnitude of the mean rate of strain tensor

$$G_\omega = \alpha \frac{\omega}{k} G_k \quad (II. 102)$$

With

$$\alpha = \frac{\alpha_\infty}{\alpha^*} \left( \frac{\alpha_0 + \frac{Re_t}{R_\omega}}{1 + \frac{Re_t}{R_\omega}} \right) \quad (II. 103)$$

The constants values for this model are:

$$\alpha_\infty^* = 1, \alpha_\infty = 0.52, \alpha_0 = \frac{1}{9}, \sigma_\omega = 2$$

$$\beta_i = 0.072, R_\omega = 2.95, R_k = 6, \sigma_k = 2, Re_t = \frac{\rho k}{\mu \omega}$$

### X.2.5 Shear stress transport k-omega model

Developed by Menter (1994), represents an innovative integration of the most effective characteristics from  $k - \varepsilon$  which are incorporated in  $k - \omega$  model. These incorporations activate the conventional modeling of  $k - \omega$  in proximity of the wall, while transitioning to the adjusted  $k - \varepsilon$  formulation farther away from the wall. Additionally, the model incorporates a damped cross-diffusion term  $D_\omega$  in the  $\omega$  equation and revises the turbulent viscosity to more effectively capture the transport of shear stress. These enhancements contribute to greater accuracy in simulations involving adverse pressure gradients and complex aerodynamic cases.

The SST  $k - \omega$  model has a similar equation set as the normal model [64] [65]:

$$\frac{\partial}{\partial t}(\rho k) + \frac{\partial}{\partial x_i}(\rho k U_i) = \frac{\partial}{\partial x_j} \left[ \Gamma_k \times \frac{\partial k}{\partial x_j} \right] + \widetilde{G}_k - Y_k + S_k \quad (\text{II. 104})$$

And

$$\frac{\partial}{\partial t}(\rho \omega) + \frac{\partial}{\partial x_i}(\rho \omega U_i) = \frac{\partial}{\partial x_j} \left[ \Gamma_\omega \times \frac{\partial \omega}{\partial x_j} \right] + G_\omega + D_\omega - Y_\omega + S_\omega + G_{\omega b} \quad (\text{II. 105})$$

The revised turbulent viscosity is reformulated as follows:

$$\mu_t = \frac{\rho k}{\omega} \times \frac{1}{\max \left[ \frac{1}{\alpha^*}, \frac{SF_2}{\alpha_1 \omega} \right]} \quad (\text{II. 106})$$

Turbulence production is defined as:

$$\widetilde{G}_k = \min(G_k, 10 \times \rho \times \beta^* \times k \times \omega) \quad (\text{II. 107})$$

While the production of  $\omega$  is defined as:

$$G_\omega = \frac{\alpha \alpha^*}{\nu_t} \widetilde{G}_k \quad (\text{II. 108})$$

Also, the dissipation of  $k$  and  $\omega$  are defined simply:

$$Y_k = \rho \cdot \beta^* \cdot k \omega \quad (\text{II. 109})$$

$$Y_\omega = \rho \cdot \beta \cdot \omega^2 \quad (\text{II. 110})$$

Moving to an important factor, instead of having a constant value the  $\beta_i$  is given by the following correlation:

$$\beta_i = F_1 \beta_{i1} + (1 - F_1) \beta_{i2} \quad (\text{II. 111})$$

The cross-diffusion term is mathematically expressed to model the transition between the 2 models as:

$$D_\omega = 2(1 - F_1) \times \rho \times \frac{1}{\omega \cdot \sigma_{\omega 2}} \frac{\partial k}{\partial x_j} \cdot \frac{\partial \omega}{\partial x_j} \quad (\text{II. 112})$$



The model constants are:

$$\alpha_1 = 0.31, \alpha_0 = \frac{1}{9}, \sigma_{\omega,1} = 2, \sigma_{\omega,2} = 1.168$$

$$\beta_{i,1} = 0.075, \beta_{i,2} = 0.0828, \sigma_{k,1} = 1.176, \sigma_{k,2} = 1.0$$

Turbulence presents a complex phenomenon characterized by chaotic and multifaced behavior, making its modeling a significant challenge. Through high fidelity techniques offer comprehensive insights, practical applications predominantly utilize methods like RANS which have some strong models that can balance precision with computational efficiency.

### **XI. Conclusion:**

This chapter has emphasized the foundational role of mathematical modeling in describing the governing equations associated with the axial turbine system, With its boundary conditions. Additionally, the turbulence models introduced were crucial to justify the simulation strategies and modeling assumptions that will be adopted in chapter III.

## CHAPTER III

# **Numerical Methods and CFD Implementation**

## **I Introduction**

The aerodynamics of axial turbine cascades encompasses complex fluid-structure interactions influenced by conservation laws that resist analytical solutions due to their coupled, nonlinear nature. Key phenomena such as rotor-stator unsteadiness, shockwave behavior, and boundary layer transitions necessitate the use of numerical approaches such as computational fluid dynamics for effective analysis. The finite volume method (FVM) excels here by dividing the domain into control volumes aligned with blade geometry, ensuring strict conservation of mass, momentum, and energy across interfaces. This approach effectively captures critical flow features, secondary vortices, tip leakage while handling irregular mesh configurations and steep gradients near surfaces. By resolving variables like pressure and velocity at cell centers, FVM enables accurate estimations of aerodynamic losses and thermal loads, directly informing turbine design for enhanced efficiency and operational longevity.

## **II Numerical Discretization Approaches**

### **Finite difference method (FDM)**

The FDM approximates differential equation using a set of algebraic equations at a set of discrete nodal points, it begins with a differential formulation of the problem and discretizes the derivatives with an accuracy that depends on the number of nodes and terms added to the approximations, the solutions are always calculated at the nodes themselves. This method typically employs structured grids and commonly applied in image processing, diffusion convection problems, thermal problems. Its limitations are:

- Oscillations and numerical diffusion especially at discontinuities
- Mass conservation is only achieved as grid spacing approaches zero
- Difficulty handling complex geometries

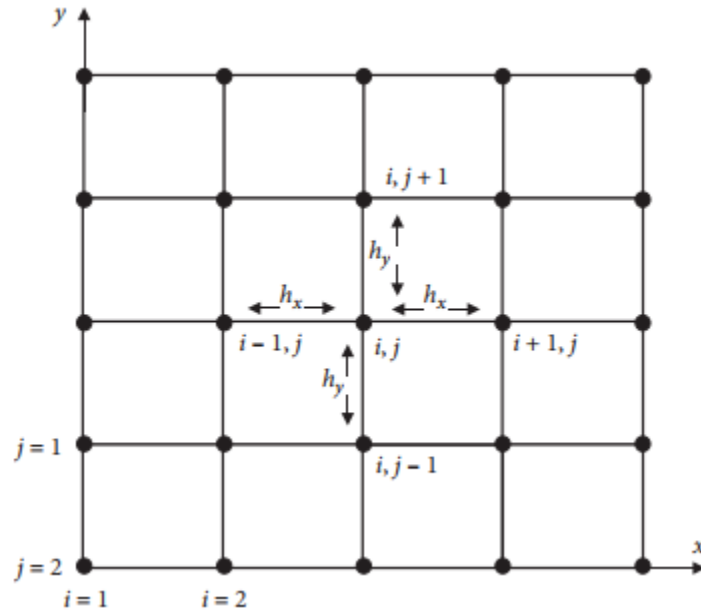


**Figure III.1:** An FDM grid representation [66].

### Finite element method (FEM)

The FEM solves boundary-value problems by discretizing a continuous domain into small, interconnected triangular (2D) or hexahedron (3D) elements. Within each element, the solution variable is approximated using polynomial shape functions defined at nodal points. To derive the governing equations, this method applies the Galerkin method. Which minimizes residuals by requiring them to be orthogonal to the chosen shape function. This process generates an element specific stiffness matrix for each subdivision, these matrices combine into one global system for the mesh after which the boundary condition are enforced to. Solving this system estimates all the values across the domain. Accuracy may be improved through mesh refinement or by employing high order shape functions, albeit with increased computational expenses [67].

### Finite volume method (FVM)

The finite volume method introduced by Patankar and Spalding in 1971 [66][67], is a numerical approach that transforms partial differential equations into algebraic equations by integrating them over small control volumes. It ensures local and global conservation of physical quantities.

The domain is divided into control volumes (structured and unstructured) making it suitable for complex geometries. Unknowns are located at the center of every single volume, and interpolation between nodes helps compute fluxes across all cell faces. This method is valued for its adaptability, accuracy to any mesh type making it widely used in simulation concerning fluid dynamics domain.

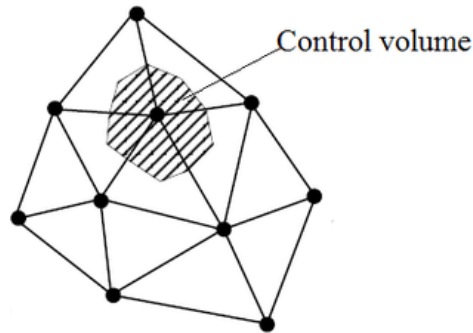


**Figure III.2:** Control volume illustration [67].

### III The fundamentals of mesh generation

- **Mesh definition:**

A mesh in the context of CFD represents a discretized model of the fluid domain, constructed by distributing a lattice of nodes that divide the geometry into numerous small, interlinked cells. These cells, whether treated as control volumes or finite elements serve as the basic units for numerically approximating the governing equations. To be effective, a mesh must be refined enough to resolve essential flow characteristics such as boundary layer behavior, temperature and represent complex shapes, while also maintaining high quality elements (skewness an aspect ratio) to ensure computational stability.

- **Meshing definition:**

Otherwise called grid generation, it refers to the process of producing a computational grid tailored for a specified CFD problem. With the application of mathematical algorithms to automate grid creation. Effective meshing clarifies user insight into the physics and phenomena of the treated problem without unduly inflating computational cost or numerical artifacts [68].

### III.1 Types of meshes

- **Structured mesh**

A Structured mesh arranges cells in an orderly logical grid indexed  $(i, j, k)$ , ideal for simple or mildly curved geometries. They include uniform cartesian grids (rectangular), stretched clusters (triangular) for resolving gradients, and curvilinear grids via coordinate mapping like H-O grids. While computationally efficient, they require block subdivisions for complex shapes and risk distortion in sharp curves [68].

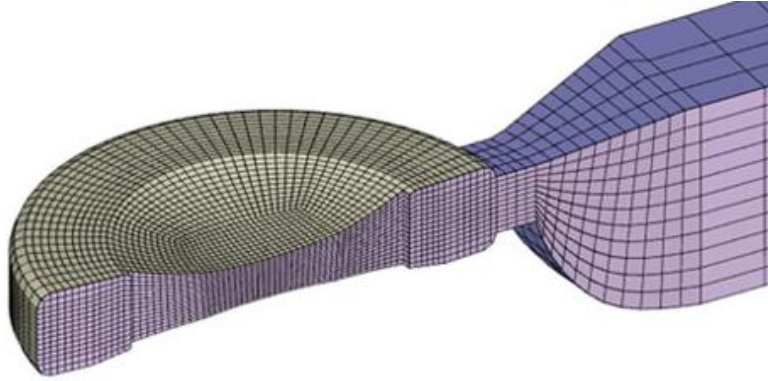


**Figure III.3:** representation of a structured mesh [69].

- **Body-fitted mesh**

Body-fitted meshes are specialized structured meshes in which the grid lines follow the domain boundaries through a curvilinear mapping  $(\xi, \eta, \zeta)$ . Ensuring precise geometry representation. Generated via algebraic or elliptic methods, they excel in turbomachinery simulations but demand equation transformations, increasing computational complexity [68].

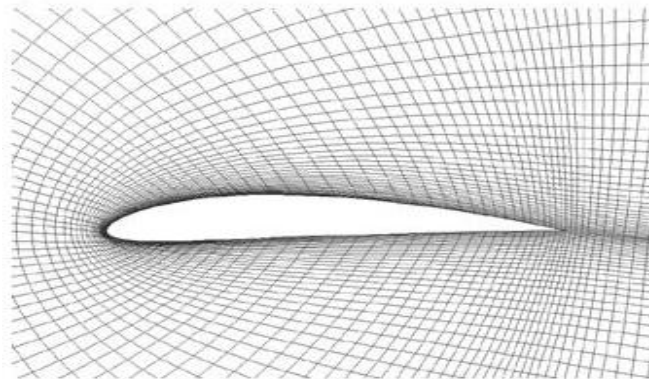


**Figure III.4:** Body-fitted mesh representation [70].

- **Unstructured mesh**

Unstructured meshes use irregular cells (triangles, tetrahedra, polyhedral) with explicit connectivity for complex domains. Hybrid versions later prism/hex cells near walls and simpler shapes elsewhere, balancing accuracy and efficiency. Though flexible, they require robust data structures, quality control, and advanced solvers due to irregularity [68].

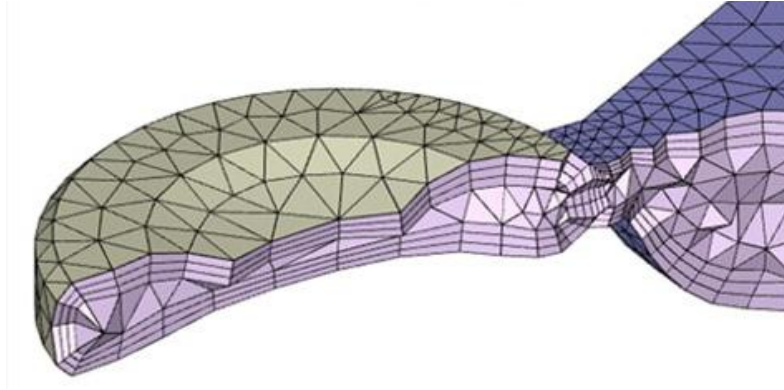


**Figure III.5:** Representation of a double unstructured mesh [69].

The geometrical shapes of internal cells are summarized in the picture down below:

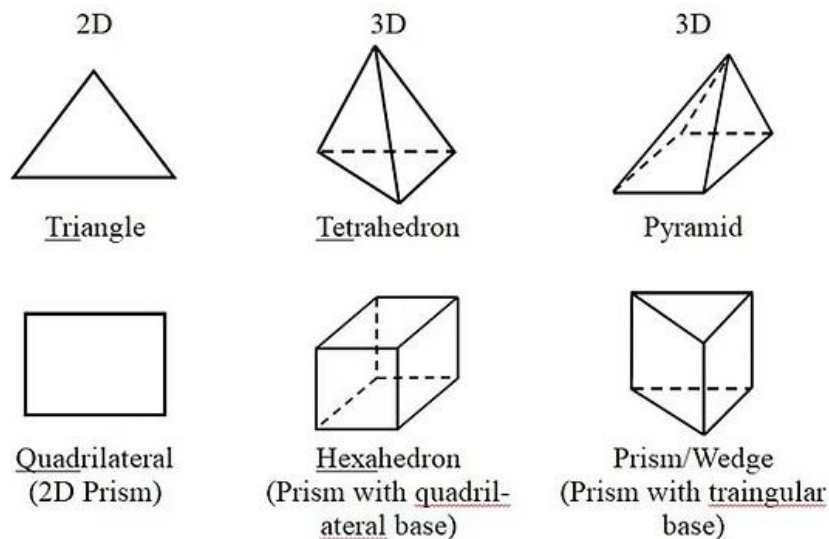


**Figure III.6:** Geometrical shapes representation [70].

## IV Numerical discretization by finite volume method

This section presents the general formulation of the FVM for the governing equations in cartesian-cylindrical coordinates, the first step is to efficiently write the equation system in convection-diffusion format which is called the transport equation otherwise, it is expressed as follows:

$$\frac{\partial \phi}{\partial \tau} + \frac{1}{r} \frac{\partial r U \phi}{\partial r} + \frac{\partial V \phi}{\partial \theta} + \frac{\partial W \phi}{\partial Z} = \Gamma_{\phi} \left[ \frac{1}{r} \frac{\partial}{\partial r} \left( r \frac{\partial \phi}{\partial r} \right) + \frac{1}{r^2} \frac{\partial^2 \phi}{\partial \theta^2} + \frac{\partial^2 \phi}{\partial Z^2} \right] + S_{\phi} \quad (\text{III. 1})$$

The variables  $\phi$ ,  $\Gamma_{\phi}$ , and  $S_{\phi}$  can be summarized in the table down below where changing each one's value for the convection and diffusion term can lead to a new equation in its differential form, which also contains the coupling between variables. It will be clear that that no analytical solution is found for these equations in the current form. Hence, finite volume method is the go-to at such cases because it handles these kinds of mathematical problems in the most efficient way:

equation	$\phi$	$\Gamma_{\phi}$	$S_{\phi}$
<b>Energy</b>	$\rho C_p T$	$k$	$\rho \dot{q}_g + \frac{1}{r} \frac{\partial}{\partial r} \left( k r \frac{\partial T}{\partial r} \right) + \frac{\partial}{\partial Z} \left( k \frac{\partial T}{\partial Z} \right) + \beta T \left( \frac{dP}{dt} + V_r \frac{\partial P}{\partial r} + V_z \frac{\partial P}{\partial Z} \right) + \phi$
<b>Continuity</b>	$\rho$	0	0
<b>Radial momentum</b>	$\rho V_r$	$\mu$	$\rho g_r - \frac{\partial P}{\partial r} + \frac{\partial}{\partial r} \left[ \mu \left( -\frac{2}{3} \nabla \cdot \mathbf{V} + 2 \frac{\partial V_r}{\partial r} \right) \right] + \frac{\partial}{\partial Z} \left[ \mu \left( \frac{\partial V_r}{\partial Z} + \frac{\partial V_z}{\partial r} \right) \right] + \frac{2\mu}{r} \left( \frac{\partial V_r}{\partial r} - \frac{1}{r} \frac{\partial V_r}{\partial \theta} - \frac{V_r}{r} \right) + \frac{1}{r} \frac{\partial}{\partial \theta} \left[ \mu \left( \frac{1}{r} \frac{\partial V_r}{\partial \theta} + \frac{\partial V_{\theta}}{\partial r} \right) \right]$
<b>Axial momentum</b>	$\rho V_z$	$\mu$	$\rho g_z - \frac{\partial P}{\partial Z} + \frac{\partial}{\partial r} \left[ \mu \left( -\frac{2}{3} \nabla \cdot \mathbf{V} + 2 \frac{\partial V_z}{\partial Z} \right) \right] + \frac{\partial}{\partial r} \left[ \mu \left( \frac{\partial V_r}{\partial Z} + \frac{\partial V_z}{\partial r} \right) \right] + \frac{\mu}{r} \left( \frac{\partial V_r}{\partial Z} + \frac{\partial V_z}{\partial r} \right)$
<b>Azimuthal momentum</b>	$\rho V_{\theta}$	$\mu$	$\rho g_{\theta} - \frac{1}{r} \frac{\partial P}{\partial \theta} + \frac{1}{r} \frac{\partial}{\partial \theta} \left[ \mu \left( -\frac{2}{3} \nabla \cdot \mathbf{V} + \frac{2}{r} \frac{\partial V_{\theta}}{\partial \theta} + \frac{2 V_r}{r} \right) \right] + \frac{2\mu}{r} \left( \frac{1}{r} \frac{\partial V_r}{\partial \theta} - \frac{1}{r} \frac{\partial V_{\theta}}{\partial r} - \frac{V_{\theta}}{r} \right) + \frac{\partial}{\partial Z} \left[ \mu \left( \frac{\partial V_{\theta}}{\partial Z} + \frac{1}{r} \frac{\partial V_z}{\partial \theta} \right) \right] + \frac{\partial}{\partial r} \left( \mu \left( \frac{\partial V_{\theta}}{\partial r} + \frac{1}{r} \frac{\partial V_r}{\partial \theta} - \frac{V_{\theta}}{r} \right) \right)$

**Table III.1:** Cylindrical coordinates system [71].



Building on Patankar's methodology, the computational domain is segmented into discrete control volumes. Scalar quantities such as temperature and pressure are centered inside the grid while velocity components are stored along each cylindrical coordinate's direction. The full set of governing equations for convection diffusion, source, and transient terms is integrated over each volume to solve the set numerically as follows:

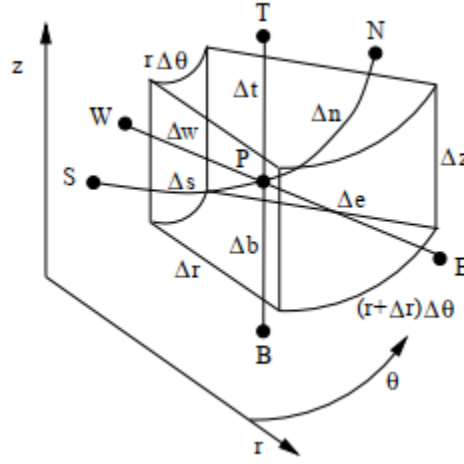


**Figure III.7:** Control volume representation in cylindrical coordinates [71].

$$F_e \phi_e + F_w \phi_w + F_n \phi_n + F_t \phi_t = D_e(\phi_E - \phi_P) - D_w(\phi_P - \phi_W) + D_n(\phi_N - \phi_P) - D_s(\phi_P - \phi_S) + D_t(\phi_T - \phi_P) - D_b(\phi_P - \phi_B) + S_\phi V \quad (\text{III. 2})$$

With:

- ❖ The letters (P, W, E, S, N, B, T) are for  $\phi$  node variables at volumes center.
- ❖ The letters (w, e, s, n, b, t) are for faces values.

Where:

- ❖ The convective coefficient of  $\phi$  at face f with a surface  $S_f$  :

$$F_f = (\rho V S)_f$$

- ❖ The diffusive coefficient :

$$D_f = \left( \Gamma \frac{S}{\Delta} \right)_f$$

### CHAPTER III

---

Introducing the Peclet number at face  $f$ , which is considered one of the main factors to evaluate values of variables at faces  $\phi_f$ , it is expressed as [71]:

$$Pe_f = \frac{F_f}{D_f} \quad (\text{III. 3})$$

The set of all the neighboring (Nb) coefficients has the following form:

$$a_{p,\phi} \cdot \phi_p + \sum_{nb} a_{Nb,\phi} \cdot \phi_{Nb} = b_{p,\phi} \quad (\text{III. 4})$$

Knowing that:

$$\rightarrow a_{W,\phi} = D_w \cdot A(Pe_w) + F_w \cdot \max(F_w, 0) \quad (\text{III. 5})$$

$$\rightarrow a_{E,\phi} = D_e \cdot A(Pe_e) + F_e \cdot \max(-F_e, 0) \quad (\text{III. 6})$$

$$\rightarrow a_{S,\phi} = D_s \cdot A(Pe_s) + F_s \cdot \max(F_s, 0) \quad (\text{III. 7})$$

$$\rightarrow a_{N,\phi} = D_n \cdot A(Pe_n) + F_n \cdot \max(-F_n, 0) \quad (\text{III. 8})$$

$$\rightarrow a_{B,\phi} = D_b \cdot A(Pe_b) + F_b \cdot \max(F_b, 0) \quad (\text{III. 9})$$

$$\rightarrow a_{T,\phi} = D_t \cdot A(Pe_t) + F_t \cdot \max(-F_t, 0) \quad (\text{III. 10})$$

With

$$a_{p,\phi} = a_{W,\phi} + a_{E,\phi} + a_{T,\phi} + a_{B,\phi} + a_{S,\phi} + a_{N,\phi} \quad (\text{III. 11})$$

And

$$b_{p,\phi} = S_\phi v \quad (\text{III. 12})$$

Noting that  $A(Pe_f)$  is somewhat a scheme function where the argument is equal to the Peclet number. The integration of the convection and diffusion term for the momentum equations at each direction, and for the energy equation. The following equations system can be introduced [71]:

$$a_{p,V_r} \cdot V_{r,p} + \sum_{nb} a_{Nb,V_r} \cdot V_{r,Nb} = b_{p,V_r} \quad (\text{III. 13})$$

$$a_{p,V_Z} \cdot V_{Z,p} + \sum_{nb} a_{Nb,V_Z} \cdot V_{Z,Nb} = b_{p,V_Z} \quad (\text{III. 14})$$

$$a_{p,V_\theta} \cdot V_{\theta,p} + \sum_{nb} a_{Nb,V_\theta} \cdot V_{\theta,Nb} = b_{p,V_\theta} \quad (\text{III. 14})$$

$$a_{p,T} \cdot T_p + \sum_{nb} a_{Nb,\phi} \cdot T_{Nb} = b_{p,T} \quad (\text{III. 15})$$

The right-hand side of the 3 first equations in the system contains a pressure gradient, where the temperature effects over the density, so it can be written as [71]:

$$b_{p,V_r} = -\frac{P_E - P_P}{\Delta e} \vartheta_r + S_r \vartheta_r = -c_r(P_E - P_P) + S_r \vartheta_r \quad (\text{III. 16})$$

$$b_{p,V_Z} = -\frac{P_T - P_P}{\Delta t} \vartheta_Z + S_r \vartheta_Z = -c_Z(P_E - P_P) + S_Z \vartheta_Z \quad (\text{III. 17})$$

$$b_{p,V_\theta} = -\frac{P_T - P_P}{\Delta t} \vartheta_\theta + S_r \vartheta_\theta = -c_\theta(P_E - P_P) + S_\theta \vartheta_\theta \quad (\text{III. 17})$$

Where:

❖  $\vartheta_r$  and  $\vartheta_Z$  are denoted as the volumes of each staggered direction

## V ANSYS CFX numerical schemes

ANSYS CFX is a trusted tool for turbomachinery simulations, offering accurate, validated results with integrated blade design and advanced modeling features. Its efficiency and reliability help engineers optimize designs, reduce costs, and streamline complex workflows.

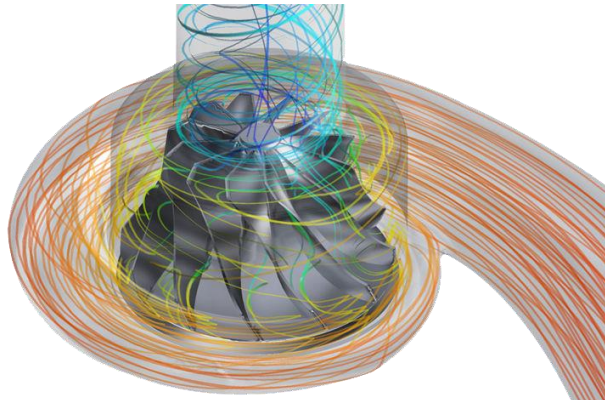


**Figure III.8:** a turbomachine simulation example [72].

- **User specified blend factor:**

Usually doesn't have a fixed well know value and varies depending on the person's set choice, mathematically  $0 < \beta < 1$ , this scheme adds something called anti-diffusive correction to the upwind scheme by integrating a small portion of the downstream values [73].

- **First-order Upwind (UDS):**

This scheme always takes the value from the upstream cell guaranteeing stability even on coarse meshes or in rapidly changing flows, with a significant numerical diffusion. It is often used as a reliable simulation starter for early convergence, it's value of  $\beta = 0$  which leads to the following equality [73]:

$$\phi_f = \phi_{up} + \beta \cdot \nabla \phi \cdot \vec{d} \quad (\text{III. 18})$$

$$\phi_f = \phi_{up} \quad (\text{III. 19})$$

Knowing that:

- $\phi_f$ : value at the integration point (face).
- $\phi_p$ : value at the current control volume node.
- $\phi_{Nb}$ : value at the neighbor node.
- $F_f$ : convective coefficient (mass flux through the face)

$$\phi_f = \phi_{up} \begin{cases} \phi_f = \phi_p, & F_f > 0 : \text{flow from P to NB} \\ \phi_f = \phi_{Nb} & F_f < 0 : \text{flow from Nb to P} \end{cases} \quad (\text{III. 20})$$

- **Central differencing scheme (CDS):**

Considered to be a second-order scheme in terms of accuracy, with a low numerical diffusion, but can be unbounded which leads to unwanted oscillations or decoupling in steep gradient zones, with  $\beta = 1$  it can be expressed as [73]:

$$\phi_f = \phi_{up} + \nabla \phi \cdot \vec{d} \quad (\text{III. 21})$$

Or mathematically, it can also be approximated as:

$$\phi_f = \frac{\phi_{Nb} + \phi_P}{2}$$

- **Bounded central difference scheme (BCD):**

Considered as an adaptive blending scheme with a variation in  $\beta$  as follows:

$$\beta = \begin{cases} 0.5, & \text{if the convection boundedness criterion is satisfied} \\ 0, & \text{if the convection boundedness criterion is violated} \end{cases}$$

this scheme's positive side is that it reduces oscillations while maintaining accuracy, but the cons of using it is it slightly more diffusive in complex flows [73].

- **High Resolution Scheme (HRS):**

As a second order scheme, it is an automatic and accurate scheme, also it is bounded but it may not converge in complex or poorly initialized cases, the blend factor  $\beta_{HRS} \leq 1$  is computed using flux limiters [73].

$$\phi_f = \phi_{up} + \beta_{HRS} \cdot \nabla \phi \cdot \vec{d} \quad (III. 22)$$

## VI Pressure-velocity coupling in ANSYS CFX

In ANSYS CFX, a co-located grid method is employed, where all study variables are stored in the control volumes which can sometimes risk pressure oscillations due to decoupled pressure-velocity fields [Patankar]. For this, CFX uses the Rhie-Chow discretization refined by Majumdar which modifies mass flow to eliminate time-step dependency in steady-state solutions to ensure stability, the advecting velocity at the integration point (ip) is defined as:

$$U_{ip} = \bar{U}_{i,ip} + f_{ip} \left( \left. \frac{\partial p}{\partial x_i} \right|_{ip} - \frac{\bar{\partial p}}{\partial x_i} \right) - c_{ip} \cdot f_{ip} (U^0_{i,ip} - \bar{U}^0_{i,ip}) \quad (III. 23)$$

With:

$\bar{U}_{i,ip}$ : the averaged advecting velocities

$f_{ip}$ : Pressure correction factor

$c_{ip}$ : time – step dependent coefficient

## CHAPTER III

---

The correction factor is expressed as:

$$f_{ip} = \frac{d_{ip}}{1 - d_{ip}c_{ip}} \quad (\text{III. 24})$$

With the geometric ratio and time dependent coefficient:

$$d_{ip} = -\frac{V}{A} \quad (\text{III. 25})$$

- V: the control volume.
- A: Momentum equation central coefficient.

And

$$c_{ip} = \frac{\rho}{\Delta t} \quad (\text{III. 26})$$

Noting that  $\Delta t$  here represent the time step.

Also, a pressure redistribution term introduces a fourth-order pressure derivative proportional to  $\Delta x^3$  to stabilize the solution, it can be expressed as:

$$f_{ip} \left( \left. \frac{\partial p}{\partial x_i} \right|_{ip} - \left. \overline{\frac{\partial p}{\partial x_i}} \right|_{ip} \right) \quad (\text{III. 27})$$

Although, this term can cause oscillations. So, CFX employs the local and averaged body-force contributions source into the term for optimization, yielding [73]:

$$f_{ip} \left[ \left( \left. \frac{\partial p}{\partial x_i} - S_i \right|_{ip} \right) - \left( \left. \overline{\frac{\partial p}{\partial x_i}} - \bar{S}_i \right|_{ip} \right) \right] \quad (\text{III. 28})$$

## VII Solution strategy in CFX

Instead of the classic “guess-solve-correct” loop, CFX tackles all equations systems together in one go through treating  $(r, \theta, Z, P)$  as a single vector of unknowns and delivers a fully implicit solution at each time increment. In steady runs, the time step acts like an acceleration parameter smoothing the solution towards convergence without messing with under relaxation factors [73].

### VII.1 The solution processes

CFX linearize nonlinear governing equations system and assemble them into a matrix system by something called the coefficient generation which enables iterative numerical solution. Furthermore, the equation solution step solves the resulting system using the Algebraic Multigrid (AMG) accelerated incomplete lower upper (ILU) factorization. This system is expressed as:

$$\underbrace{[A]}_{\text{coefficient matrix}} \cdot \underbrace{[\phi]}_{\text{solution vector}} = \underbrace{[s]}_{\text{source terms}} \quad (\text{III. 29})$$

The solution vector approximations are further refined, yielding:

$$\phi^{n+1} = \phi^n + \underbrace{\phi'}_{\text{correction}} \quad (\text{III. 30})$$

Where the correction is a solution of:

$$A \cdot \phi' = \underbrace{r^n}_{\text{residual}} \quad (\text{III. 31})$$

The residual can be obtained from the following equation [73]:

$$r^n = b - A\phi^n \quad (\text{III. 32})$$

### VII.2 The algebraic multigrid

This method is employed to accelerate convergence, it takes the fine detailed grid equations and combines them into a simpler, coarser form. On this coarse mesh, hard to fix errors decrease until they are completely eliminated. Then, those corrections are sent back into the original grid. These corrections steps merge nearby cells on the coarse grid to keep the accuracy of the governing equations for large scale volumes, this is a one pass operation as the mesh never a rebuild [73].

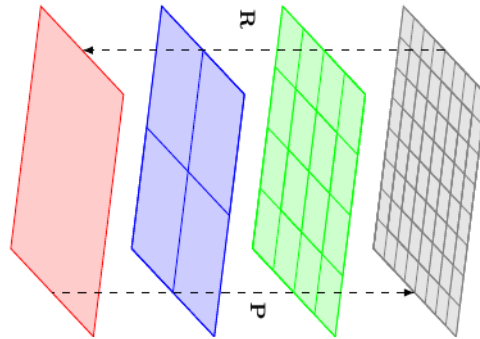


**Figure III.9:** Multigrid method [74].

The CFX algorithm flowchart can be presented as follows:

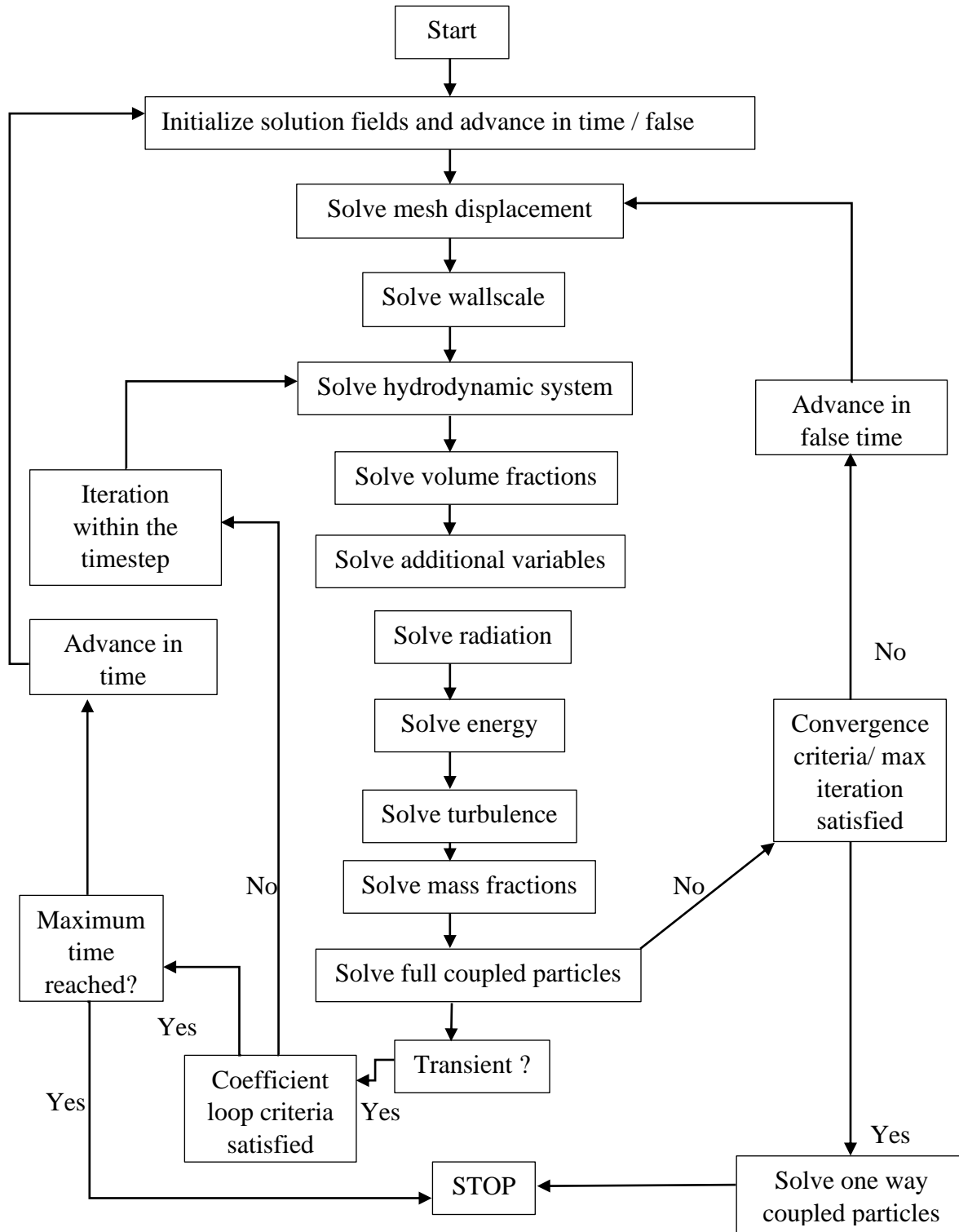


Figure III.10: CFX Algorithm [72].



### VIII CFturbo software

CFturbo is an advanced computational tool vital for the design process of axial turbines, effectively incorporating the governing aerodynamic principles such as flow dynamics, process of energy transfer, and the optimization of losses in blade designs. This software accelerates the development process through algorithmic design steps from operational parameters such as pressure gradients to the creation of the 3D Model while allowing for precision in modifications on blade profiles and aerodynamic performance.

CFturbo has the best compatibility with CFD/FEA simulation software like ANSYS, Open-Foam with its extensive fluid-profiles database. By merging empirical knowledge of turbomachinery with data from various computational methodologies, this software promotes turbine research to another level establishing itself as a crucial resource for thesis-oriented progress for turbine engineering.

#### VIII.1 Cascade geometry creation

In this thesis, a basic axial impulse turbine cascade geometry was selected as a starting point, and its key dimensions were methodically modified to farther reflect our design objectives. By introducing the targeted modification from blade angles to chord lengths passing by the spacing, the aim is to investigate their influence on aerodynamic performance, the following sections will walk through each modification to describe the rationale procedure step by step. In the global setup window, overarching design parameters are defined to establish the first foundation. For this study, these parameters are defined as:

- ✓ Mass flow rate: 0.61 Kg/s
- ✓ Total-to-static pressure ratio: 1.62.
- ✓ Rotational speed: 38000 Rpm.
- ✓ Working fluid: air.
- ✓ Thermodynamic model: perfect gas model.
- ✓ Inlet total pressure: 2.05 bar.
- ✓ Inlet total temperature: 805 K.
- ✓ Rotation direction: clockwise.
- ✓ Initial total-to-static efficiency: 100%

→ Choosing the right model for the study:

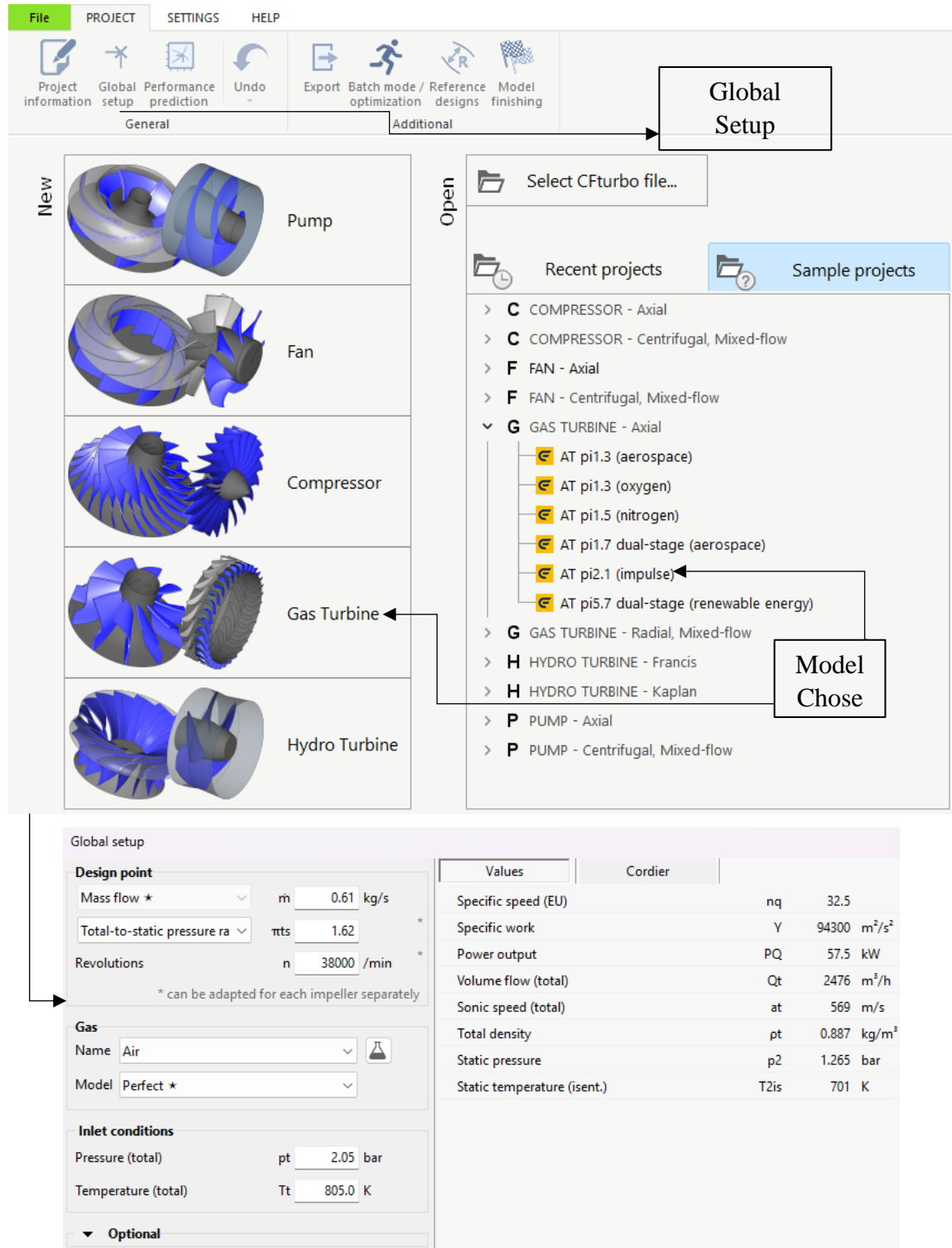
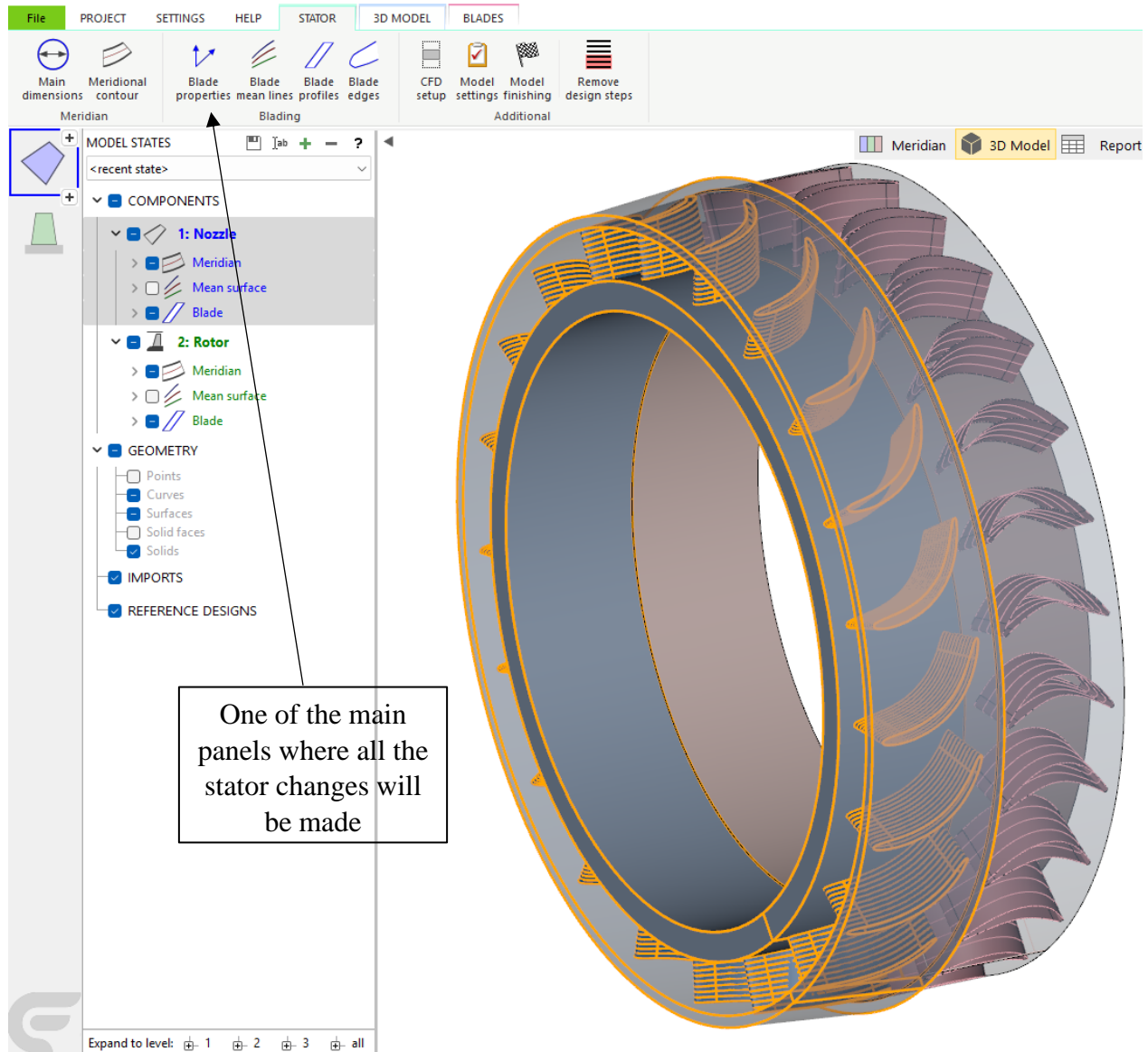


Figure III.11: CFturbo Interface + Global setup [6].

## CHAPTER III

Once the basic geometry is defined, CFturbo automatically opens a second window showcasing the meridional contour alongside a 3D view of the chosen model of the chosen model and the blade modification panels. Here, a tweak for every parameter is possible from fine surface details to primary angles and in the next section, a presentation of all changes for a stator blade in a consolidated table detailing will be discussed:



**Figure III.12:** The 3D representation of the default model [5][6].

After this step, as illustrated in figure 4, only the blade specific properties were modified in the stator design, while other settings retained CFturbo's default values. The adjustments include:

parameter	Value
Leading edge angle $\alpha_{BLE}$	0° (all spans)
trailing edge angle $\alpha_{BTE}$	60° (all spans)
Leading edge thickness	1.4 mm
trailing edge thickness	0.7mm
Number of spans/blades	5/21

**Table III.2:** General stator parameters.

The role of each one:

- ✓  **$\alpha_{BLE}$ :** minimizes the flow incidence losses by aligning the blade with axial flow.
- ✓  **$\alpha_{BTE}$ :** controls the flow deviation at the outlet for precise energy transfer to the rotor.
- ✓ **Blade thickness:** Balances the durability and reduces the wake.
- ✓ **Spans:** divides the blade in the radial sense into segments for optimization spanwise.

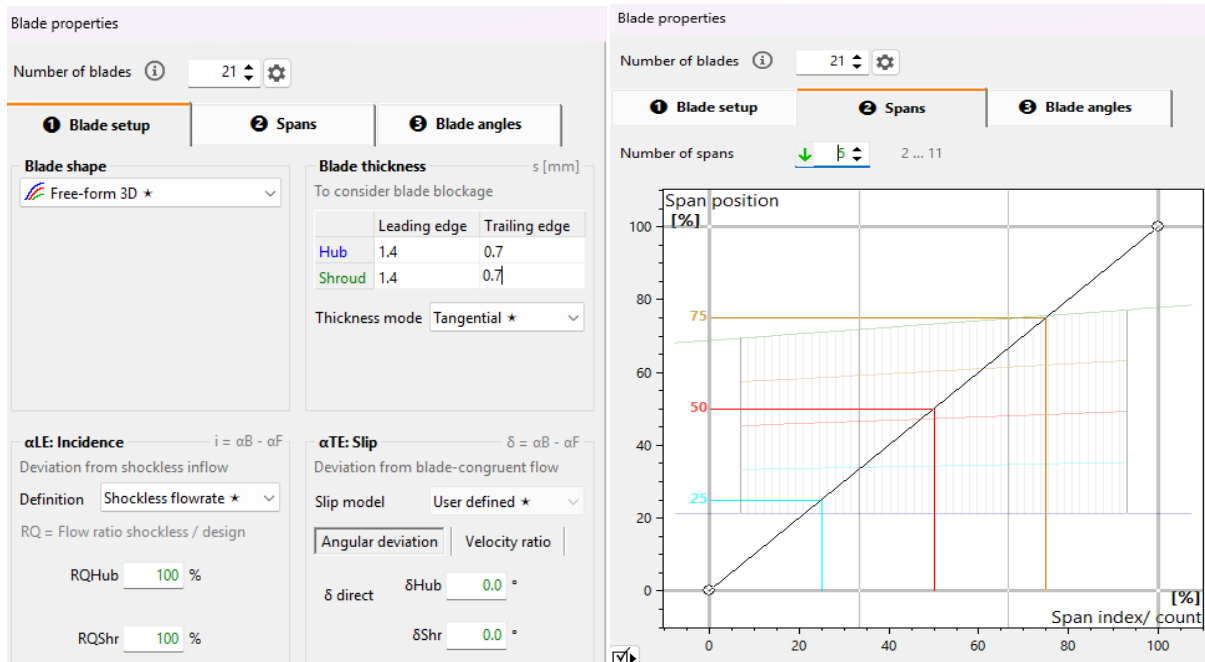


**Figure III.13:** Blade setup and span number panels in Cfturbo [5] [6].

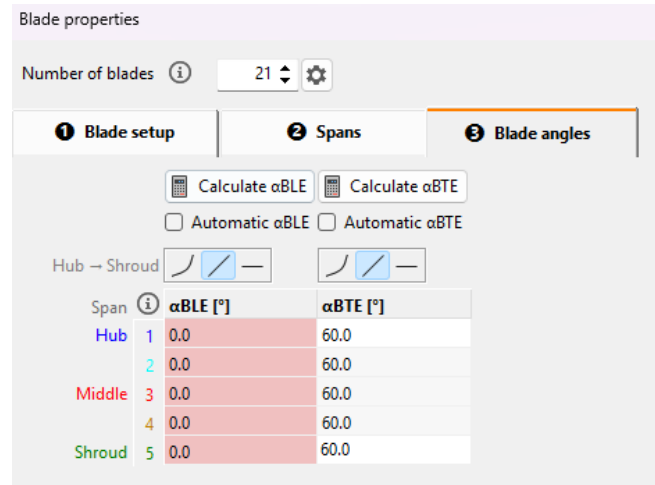


**Figure III.14:** Stator Blade angles spanwise [5][6].

Similar to the stator, the rotor blade parameters were adjusted using the same methodology. The only difference is that there is an additional value changed in the third mean lines panel, the modified values are summarized below:

Parameter	Value
Leading edge angle $\beta_{B_1}$	45° (shroud)
trailing edge angle $\beta_{B_2}$	-45° (shroud)
Leading edge thickness	0.5 mm (Hub/Shroud)
trailing edge thickness	0.5mm (Hub/Shroud)
Number of spans/blades	5/27
Angular Position $\Delta\phi$	0° (all spans)

**Table III.3:** General rotor parameters.

where:

- ✓  $\Delta\phi$ : simplifies the simulation by eliminating the blade wrapping/overlapping.

Following these modifications, the finalized geometry can be exported to an ANSYS compatible format using Cfturbo's dedicated extension. This ensures seamless integration with ANSYS for subsequent simulations and analysis. The resulting cascaded configuration is visualized in the figure down below:

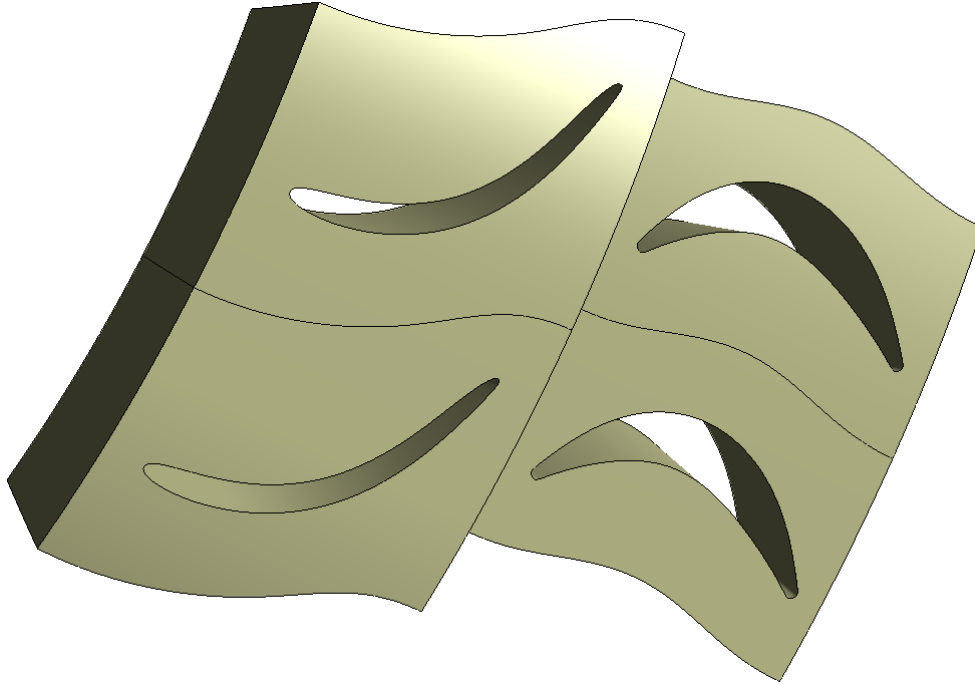


**Figure III.15:** Cascade 3D illustration.

## VIII.2 Meshing

To predict the flow in the axial turbine cascade in an efficient reliable way during the simulation, a structured body fitted hexahedral mesh was generated using ANSYS TurboGrid module to ensure precise alignment with the blade geometry, this mesh type conforms to the contours of blade shapes to minimize the interpolation errors and to maximize the accuracy of calculations. The process of geometry created to TurboGrid meshing can be illustrated in a simple scheme as follows:

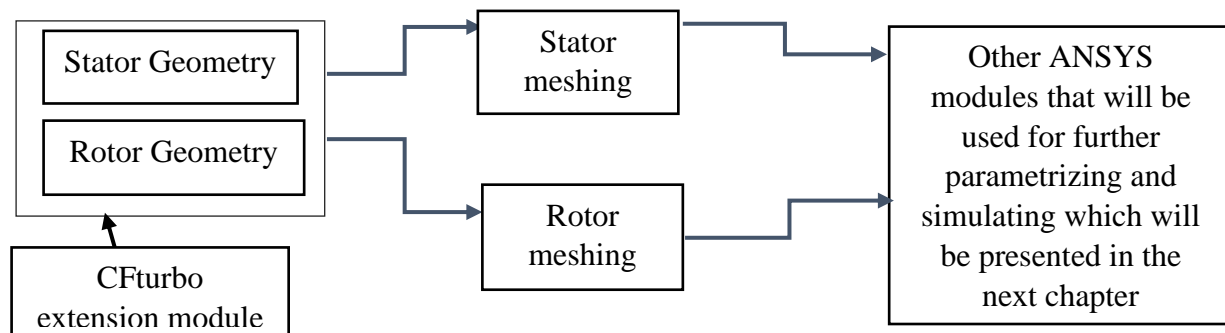


**Figure III.16:** Step-by-step process illustration

## CHAPTER III

---

The mesh was automated by the module's default algorithms with minimal intervention, the basic changes that were made in mesh data panel are:

- A global scaling size factor of 1.5 to increase the number of elements and maintain the proportional refinement near the edges.
- No explicit inflation layers near-wall were employed. TurboGrid default clustering is enough to ensure accurate resolution for the flow analysis.

An example of mesh statistics can be expressed in the following table:

component	Number of elements	Number of nodes
<b>Rotor</b>	631638	660996
<b>Stator</b>	979020	1020050

**Table III.4:** Meshing Results.

Finally, the structured grid is visualized in the figure down below:

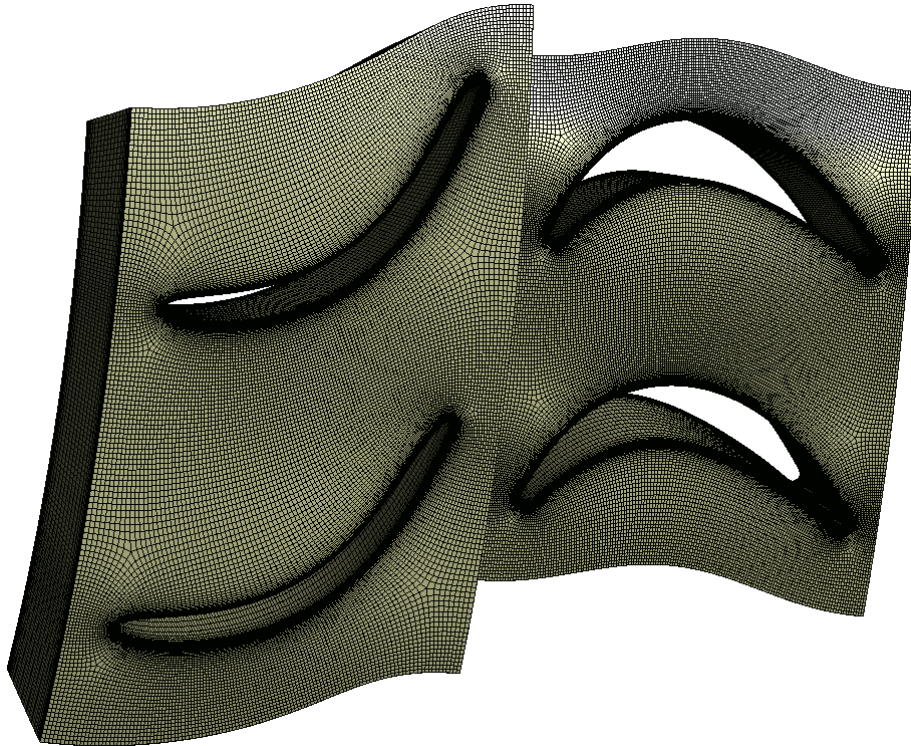


**Figure III.17:** Preview of the study mesh.



## IX Artificial Neural Network

Artificial Neural Networks (ANN) are dynamic computational architectures that replicate the biological brain neural network through artificial layers of interconnected neurons managed by modifiable parameters (links). The ANN usually consist of 3 pillar phases, the training phase where it is exposed to the desired input(samples)-output(correct answers) data set which are used to iteratively adjust the internal parameters (weights) to minimize prediction errors, after extensive iterative operation, the ANN enhances its ability to associate the inputs to their right outputs , next is the validation phase where the performance is tested on another data set different from the one used in training to check if the network understood the patterns not just memorizing data. Last is the testing phase, which checks how well the network with real life problems by giving it a completely news data set completely different from the training one and see how it can handle it, if it identifies the parameters from the previous 2 phases, the model truly learned and is ready for real life tasks [76].

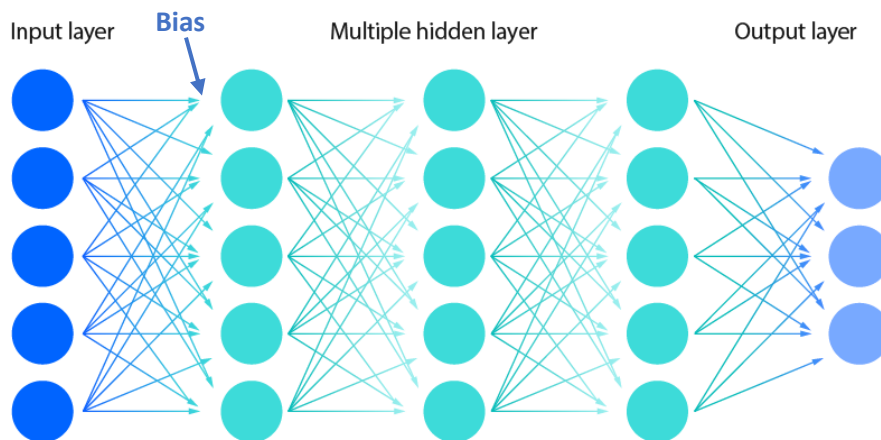


**Figure III.18:** Neural Network Layers [75].

As the figure above illustrates, the ANN processes data through:

- Input layer: receives the raw data.
- Hidden layer: process the data internally.
- Output layer: gives the final result.

Each neuron has a working methodology, which will be explained in two steps:



### IX.1 Linear combination:

The neuron combines all the inputs using adjustable weights and add a bias (constant):

$$\text{Total Input} = (W_1x_1) + (W_2x_2) + \dots + (W_nx_n) + b_i \quad (\text{III. 33})$$

$$\beta_i = \sum w_{ij}x_j + b_i \quad (\text{III. 34})$$

Where:

- $w_{ij}$ : the total weight from neuron j to i
- $x_j$ : the input from neuron j
- $b_i$ : the bias term for neuron i

For the output, hidden neurons activation

$$\alpha_i = f(\sum w_{ij}x_j + b_i) \quad (\text{III. 35})$$

- ❖ Knowing that f is an activation function (Sigmoid, tanh....)

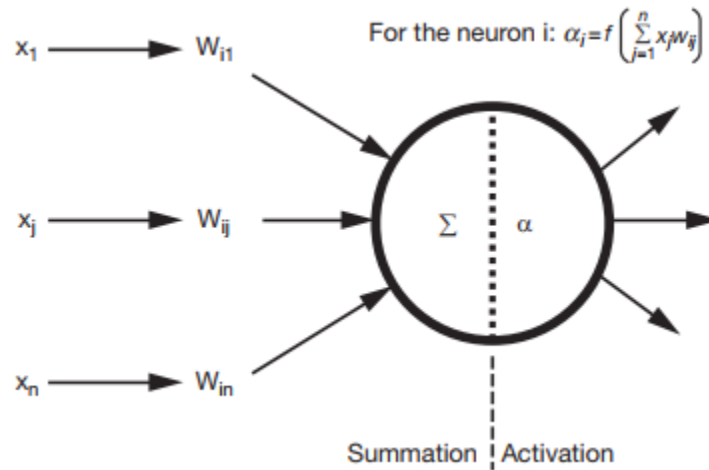


**Figure III.19:** Neural network unit data process schematic [76].

Neural networks re commonly used in the following areas of machine learning:

- ❖ segmentation of images and video
- ❖ objects detection in images
- ❖ assistance in medical diagnosis by classifying tumors and diseases [76].

- ❖ solution approximations for differential equations.

## IX.2 Error Calculation in ANNs

The error calculation in ANN models employs the widely known supervised learning algorithm called Backpropagation. This algorithm operates by systematically minimizing prediction errors through iterative adjustments of the weights to optimize the performance. While these adjustments are guided by gradient descent, the error difference between the expected and the actual output is evaluated using the ROOT MEAN SQUARE (RMS) error, mathematically expressed as:

$$E = \frac{1}{2} \left[ \sum_p \sum_i |t_{ip} - o_{ip}|^2 \right]^{0.5} \quad (\text{III. 36})$$

Where E is the total error,  $t_{ip}$  and  $o_{ip}$  are the target output and the generated output by the network respectively for each pattern p.

Initially, the weights that link neurons have random values, the input is then passed forward to calculate each neuron's activation  $x_{ip}$ . After which, the resulting output (error) is then Backpropagated to correct the weights based on their involvement for the initial output error [76].

The error for an output layer neuron in case of a logistic-sigmoid activation is calculated as follows:

$$\delta_{ip} = (t_{ip} - x_{ip}) \cdot x_{ip} \cdot (1 - x_{ip}) \quad (\text{III. 37})$$

For a hidden layer neuron:

$$\delta_{ip} = x_{ip}(1 - x_{ip}) \cdot \sum_k \delta_{pk} \cdot w_{jk} \quad (\text{III. 38})$$

Weight adjustments are calculated through:

$$\Delta \omega_{ij} = \varepsilon (\delta_{pj} x_{pi}) + L \cdot w_{ij(\text{old})} \quad (\text{III. 39})$$

Where:

- $\varepsilon$  is the learning rate for weight adjustment

- $L$  is the momentum factor for stabilization
- $x_{pi}$  is the neuron (i) activation for pattern  $p$
- $\delta_{pj}$  the error gradient at neuron  $j$
- $mw_{ij}(\text{old})$  previous weight value
- $k$  the summation over all nodes in the direction of the output later
- $j$  the weight position in each node

with multiple backward and forward passes, the network improves its accuracy by adjusting weights to map in a precise way the inputs to the outputs [76].

## X Conclusion

This chapter holds the detailed explanation of the major numerical approaches used in simulations, mesh generation, and discretization methods. CFturbo geometry creation process is further detailed in this chapter with all the chosen variable values and parameters along with CFX simulation setup and general algorithm. It also details the ANNs phases explanation and all necessary error formulations used to analyze the integrity and capability of this model's power.

## CHAPTER IV

# Results and discussion

## I Introduction

This chapter deals with the investigation of the blade metal angles effect on a micro-scale axial gas turbine efficiency and its scaling to an industrial level using non-dimensional parameters and simplifying hypothesis, simulations were performed at 38000 Rpm and 0.61kg/s retain these parameters to predict the exact performance at 3200 Rpm (large-scale industrial axial turbine):

- Flow coefficient  $\varphi$
- Reaction degree  $R$
- Total work coefficient  $\psi$

A brief overview of the cfx setup describes the solver settings with all the important details such as boundary conditions, solver schemes, turbulence model, and discretization models. This section is followed by a grid-dependency study to determine the proper and optimal node number for logical results and computational efficiency. Also, a validation of the NACA-4412 blade profile using the same models and methods as in the turbine simulation to validate that the chosen parameters succeed to attain the desirable results.

Efficiency results across the rotor inlet and outlet blade metal angles are then used to identify 8 optimal configurations with the highest performance and lowest losses. For these pairs, different contour plots are then shown to display key features such as shocks and flow separation. The chapter wraps up with an ANN section to predict efficiency for blade angles to provide a fast and precise design evaluation tool.

## II CFX parameterization

This section outlines the critical parameters applied to the simulations. To enable replication of the study and precise analysis or comparisons, all computational inputs including, solver parameters, turbulence models, numerical methods, and boundary conditions are well described in the table below. Such a methodological transparency not only aids but also clarifies the validity and scope the conclusions derived from the computational results.

Type	Parameter	Setting	Justification
Global turbo mode	Machine type	Axial turbine	Standard for turbomachines
Component configuration	Stator theta offset	4° (degrees)	Aligns the stator blade to optimize the flow entry to the rotor
	Rotor rotational speed	-38000 Rpm	Negative sign for clockwise rotation
Physics	Fluid model	Air ideal gas	For a compressible simulation
	Reference pressure	0 atm	Simplifies relative pressure calculations
	Heat transfer model	Total energy	Considers both thermal and kinetic energy fluctuations
	Turbulence model	k – $\omega$ Shear Stress Transport model	Accuracy and reliability for all turbulent phenomena
Boundary conditions	Inflow or stator inlet		
	Condition type	Mass flow inlet	For mass flow rate per design requirements
	Total temperature	805 K	To match upstream energy conditions
	Mass flow rate	0.61 Kg/s per machine	To ensure mass conservation aligns with design specifications
	Flow direction	Normal to boundary	Simplifies initialization
	Outflow or rotor outlet		
	Condition type	Static pressure outlet	Fixes the exit pressure to ambient level
	Static pressure	1 atm	Avoids unrealistic flow reversal

<b>Interface</b>	<b>Stator-rotor interface</b>	Stage (mixing plane)	So that the flow can be averaged circumferentially
	<b>Stator side (S1)</b>	Outflow	Flow leaves stator into rotor
	<b>Rotor side (R1)</b>	Inflow 2	Flow enters the rotor
<b>Solver settings And Expert solver settings</b>	<b>Advection scheme</b>	Blend factor =1.0	A full 2 <sup>nd</sup> order accuracy for sharp resolution
	<b>Turbulence Numerics</b>	High resolution	Improves accuracy for turbulence model variables k and omega
	<b>Max iterations</b>	5000	For convergence control
	<b>Convergence criteria</b>	RMS at 0.00001	To ensure precise solution accuracy
	<b>Linear solver</b>	Algebraic Multigrid	Robust for large systems and turbomachinery
	<b>Model coefficient relaxation</b>	0.9	Prevents divergence for turbulence equations
	<b>Wall scale relaxation</b>	0.75	Controls near-wall turbulence for stability

Table IV.1:CFX parameters types and values.

### III Grid convergence study

A grid dependence study investigates the CFD simulation results such as total-to-total efficiency sensitivity to a series of mesh resolutions. But, increasing the grid resolution to a finer level doesn't always guarantee stabilization, the results may continue to fluctuate even on the finest grids. To deal with such a complex uncertainty phenomenon, Grid convergence index (GCI) developed by (Celik et.al 2008) and (Eça & Hoekstra, 2009) is introduced. This method, quantifies how two consecutive grids along with their convergence rate value and a safety factor approximate the ideal case (infinitely fine grid). The GCI ensures accurate results as a function of acceptable computational cost [77][78].

### III.1 Mathematical formulations:

- **Grid spacing:**

$$GS = \left( \frac{1}{NN} \right)^{\dim}, \quad \dim = \frac{1}{\text{dimensions}} = \frac{1}{2} \text{ for a 2D case} \quad (\text{IV. 1})$$

With

- ❖ NN: the total nodes number of the grid.

- **Refinement ratio:**

$$rr = \frac{GS_{\text{coarse}}}{GS_{\text{fine}}} > 1 \quad (\text{IV. 2})$$

- **Relative error:**

$$\epsilon = \left| \frac{\text{efficiency}_{\text{fine}} - \text{efficiency}_{\text{coarse}}}{\text{efficiency}_{\text{fine}}} \right| \times 100 \quad (\text{IV. 3})$$

$$\epsilon = \left| \frac{\eta_{\text{fine}} - \eta_{\text{coarse}}}{\eta_{\text{fine}}} \right| \times 100 \quad (\text{IV. 4})$$

- **GCI expression:**

$$GCI = \frac{F_S \times \epsilon}{r^{OA} - 1} \quad (\text{IV. 5})$$

With

- ❖  $F_S = 1.25$ : the safety factor from the ASME [77] [78].

- ❖ OA=2: order of accuracy (2<sup>nd</sup> order scheme).

### III.2 Grid study table and GCI results

With the GCI definition and mathematical formulations, it is now logical to present to grid dependency study results for this thesis simulations which will be shown down below, followed by a line chart and GCI results extracted from a well-detailed MATLAB program which identifies the 2 best pairs of grids to choose one with highest accuracy and second highest with considerations to computational power and cost:



N° of stator nodes	N° of rotor nodes	Total N° of nodes	Size factor	Efficiency (%)
147160	187656	334816	0.9	89.1548
167886	222750	390636	0.95	89.1836
201345	299897	501242	1.0	89.2015
251534	345520	597054	1.1	89.2893
297726	387900	685626	1.15	89.4423
332588	446842	779430	1.2	89.4595
385596	501322	886918	1.25	89.5824
531040	691372	1222412	1.4	89.6399
660996	899712	1560708	1.5	89.6523

**Table IV.2:** CFD grid convergence study table.

The GCI MATLAB code generated the following calculations table:

Fine Size factor	Coarse size factor	Fine efficiency	Coarse efficiency	rr	Relative error	GCI value
1.5	1.4	89.6523	89.6399	1.1299	0.0138	0.0625
1.4	1.25	89.6399	89.5824	1.1740	0.0642	0.2119
1.25	1.2	89.5824	89.4595	1.0667	0.1372	1.2435
1.2	1.15	89.4595	89.4423	1.0662	0.0192	0.1757
1.15	1.1	89.4423	89.2893	1.0716	0.1711	1.4414
1.1	1	89.2893	89.2015	1.0914	0.0983	0.6430
1	0.95	89.2015	89.1836	1.1328	0.0200	0.0886
0.95	0.9	89.1836	89.1548	1.0801	0.0323	0.2421

**Table IV.3:** GCI values.

The best 2 pairs for the lowest GCI:

- 1.5 → 1.4 with a GCI=0.0625
- 1.0 → 0.95 with a GCI=0.0886

So, for the personal choice, a grid size of 1.0 was chosen for further simulations to account for accuracy and computational cost.

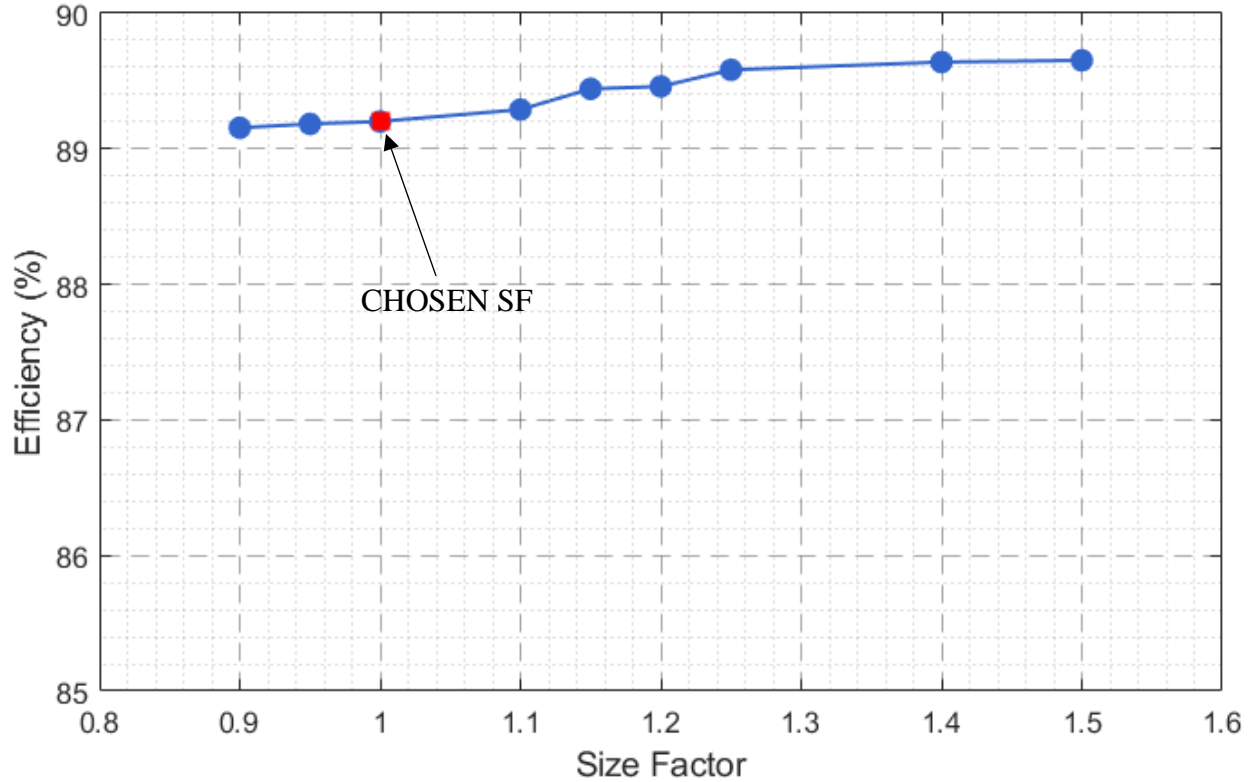


**Figure IV.1:** Size Factor vs Efficiency CFD results.

## IV Naca-4412 case validation

This section presents a validation of the CFD setup using the NACA airfoil profile with the results of NASA wind tunnel data and a turbulence model analysis by AlJarallah et.al (2023) [81]. Even though the validation did not attend the perfect match due to differences in setups, it serves as

### IV.1 The setup

The naca-4412 profile coordinates were extracted from an online tool called airfoil-tool [79][83], a C-grid and O-grid were used on the perimeter of the blade to better englobe the boundary layers behavior that suffer from flow separation. The simulation conditions are:

- Angle of attack (AOA):  $13.87^\circ$
- Reynolds number: 1.52 million (fully turbulent flow)

- Mach number: 0.1 (subsonic)
- Farfield boundary: at x100 times the chord length ( $c=1$ ) to eliminate artificial fluctuations in results.
- Stream speed: 22.292 m/s (matches the Reynolds number).

These conditions along with ANSYS CFX specified parametrization that matches the physics and solver settings section in TABLE IV.1 formed the basic setup for this validation. Another key point is the method followed to have the simulation attack the profile at an angle of  $13.87^\circ$  without rotating the geometry is to vectorize the stream velocity x and y components to match the following:

- X-direction :  $\cos(13.87^\circ) = 0.971245$ .
- Y-direction :  $\sin(13.87^\circ) = 0.238129$ .

These 2 parameters values help set the desired angle of attack without the need of rotating any profile. The simulation domain meshing and contour displays, comparison results of lift and coefficients to the NASA and article results is shown as follows:

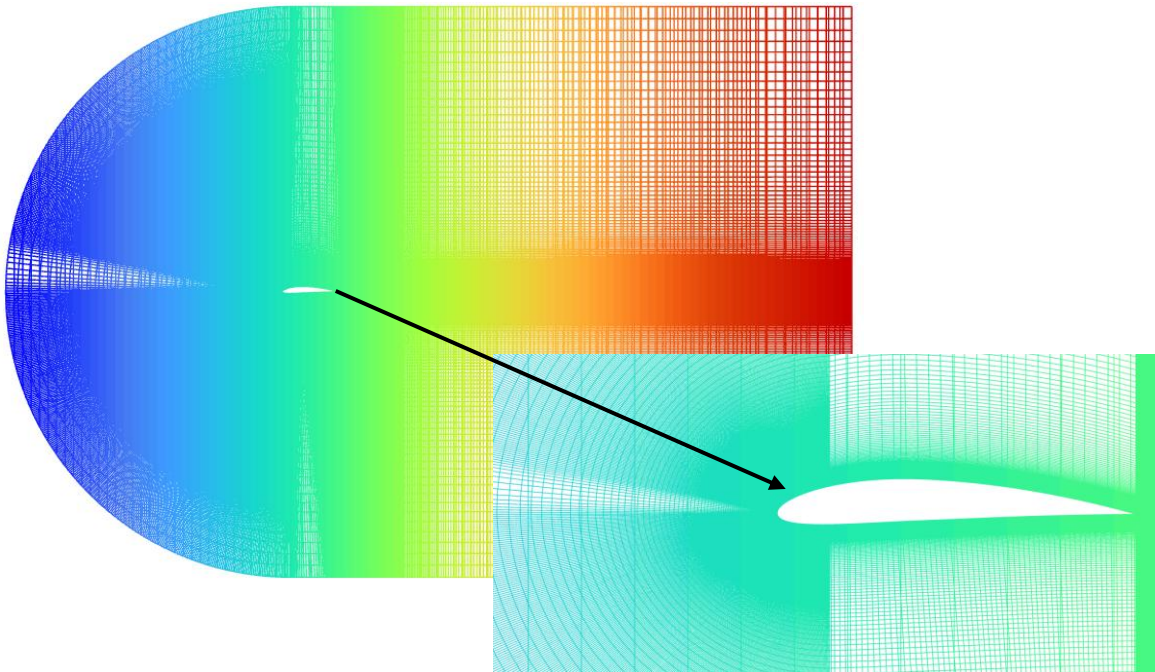


**Figure IV.2:** Domain meshing and a zoom-in of the profile perimeter body-fitted mesh.

The lift and drag coefficient comparison table is presented as follows:

Analysis	NASA report	Article	Validation
<b>Drag-coeff</b>	0.0311	0.0320	0.03219
<b>Lift-coeff</b>	1.616	1.6196	1.6757

The resulting error with the NASA report is:

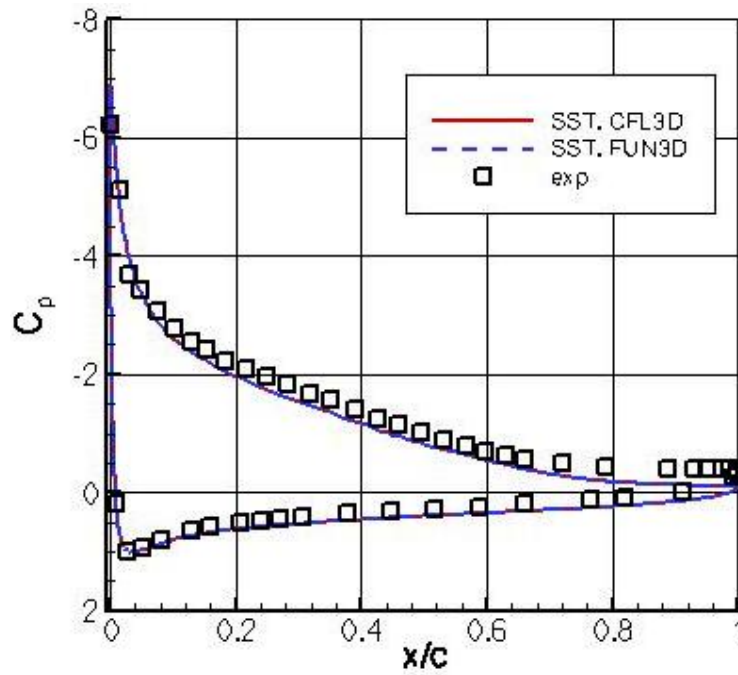
Parameter	CFD	NASA	Difference	Error (%)
<b>Lift coeff</b>	1.6757	1.616	0.0597	3.69%
<b>Drag coeff</b>	0.03219	0.0311	0.00109	3.50%

The resulting error with the article is:

Parameter	CFD	NASA	Difference	Error (%)
<b>Lift coeff</b>	1.6757	1.6196	0.0561	3.46%
<b>Drag coeff</b>	0.03219	0.0320	0.00019	0.59%

**Table IV.4:** Results Comparison.

Additionally, pressure coefficient as a function of ( $x/c$ ) comparison between the article and personal simulations is shown down below:



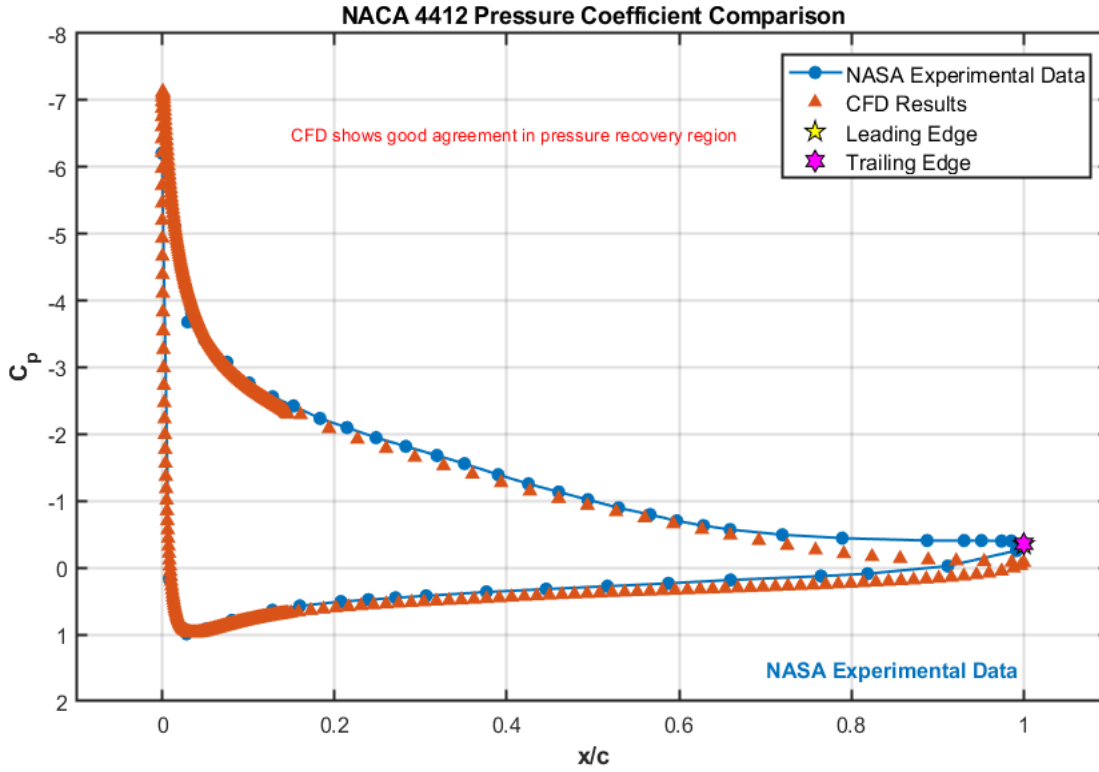


**Figure IV.3:** Pressure coefficient vs  $x/c$  plots, Bottom (Thesis) and Top (NASA-report) [82].

In summary, the simulation results showed an excellent level of agreement with the two references experimental results for the naca-4412 profile at specified conditions, with a minimal error for both lift and drag coefficients. Also, the velocity contour and pressure coefficient graph were almost identical to the references which proves that the CFD setup adapted in this thesis is reliable and accurate to analyze the aerodynamics of the stator-rotor cascades.

## V Core simulation results and discussion

Key outcomes from the CFX simulations on the chosen 1.0 (500k nodes) size factor grid are presented in this section which compares overall performance parameter chosen for this thesis which is the total-to-total isentropic efficiency to the variation of the rotor blade metal (shape) angles to identify 5 optimal configurations with the highest efficiencies, the variation of angles is as follows:

- ✓ Rotor inlet blade metal angles  $\beta_{B_1}$ : from 22 to 40°
- ✓ Rotor outlet blade metal angles  $\beta_{B_2}$ : -60°, -65°, -70°, and -75°

The results are presented in 4 different tables down below:

$\beta_{B_2} = -75^\circ$	$\beta_{B_1}$	Total-to-total efficiency	$\beta_{B_2} = -70^\circ$	$\beta_{B_1}$	Total-to-total efficiency
	22	87.7295		22	88.0049
	24	88.5650		24	88.3401
	26	88.8471		26	88.5432
	28	89.0679		28	88.8086
	30	89.2015		30	89.0175
	32	89.1283		32	89.1343
	34	88.9914		34	89.0749
	36	88.8205		36	88.6935
	38	88.2316		38	88.0298
	40	87.6422		40	87.4265

$\beta_{B_2} = -65^\circ$	$\beta_{B_1}$	Total-to-total efficiency	$\beta_{B_2} = -60^\circ$	$\beta_{B_1}$	Total-to-total efficiency
	22	87.6844		22	85.9417
	24	88.2787		24	87.3774
	26	88.5471		26	88.0125
	28	88.7724		28	88.2936
	30	88.9459		30	88.4931
	32	88.9894		32	88.9178
	34	88.9583		34	88.6577
	36	88.6608		36	88.3475
	38	87.8370		38	87.7751
	40	87.2154		40	86.9768

**Table IV.5:** Simulation Results Values.

To better understand the influence of the influence of these angles of the turbine efficiency, a detailed chart is plotted down below:

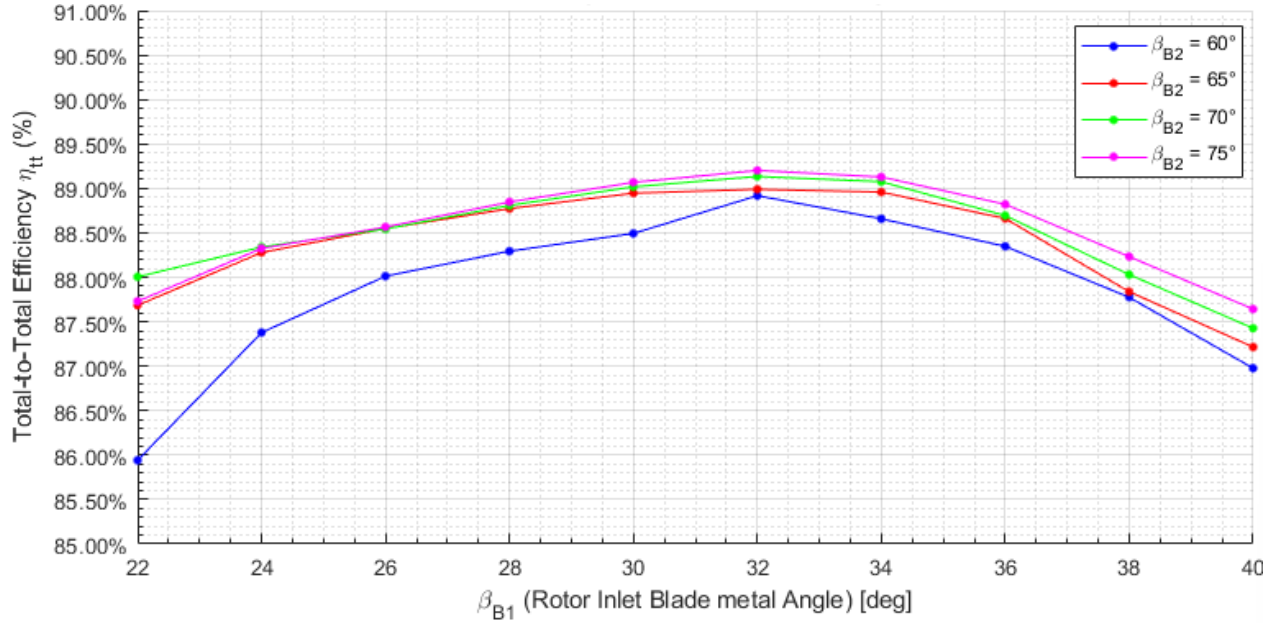


**Figure IV.4:** Inlet angle vs efficiency chart.

Figure IV.4 illustrates how the total-to-total efficiency varies with the different inlet rotor shape angles (metal)  $\beta_{B1}$  for a set of four outlet shape angles that ranges from 60 to 75°. Noting that as a starter,  $\beta_{B1} = 22^\circ$  is taken as a reference point for comparison. The chart shows a clear increase in efficiency as  $\beta_{B1}$  increases across all outlet angles, the maximum efficiency is reached in between an optimal range of 32° and 34° where it exceeds 89% which is likely due to the improved incidence at the rotor leading edge section which guarantees a smoother flow entry and lessens total aerodynamic losses. Beyond this range, the efficiency starts to decline which is likely due the excessive deviation of the incoming flow that causes unnecessary losses and local flow separation until it reaches its lowest value at:  $\beta_{B1} = 22^\circ$  and  $\beta_{B2} = 60^\circ$ . Overall, this chart highlights the vital role of the changes of blade shape angles pairing in the general turbine design and in achieving efficient and durable energy conversion.

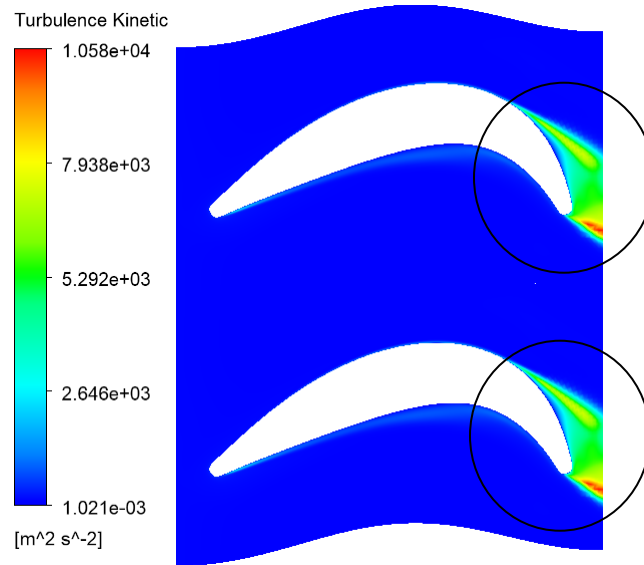
## VI Simulation Contours

This section treats all the necessary contour maps, charts, and detailed explanations of the optimal pairs chosen from the preceding section. As shown earlier, the optimal cascades correspond the ones that pair with the rotor inlet angles of 32° and 34° since these yield the highest efficiency percentages for each major case. This analysis will be structured into two parts: thermal characteristics (temperature and pressure) and the aerodynamic characteristics (Mach and vertices)

## VI.1 Temperature evolution

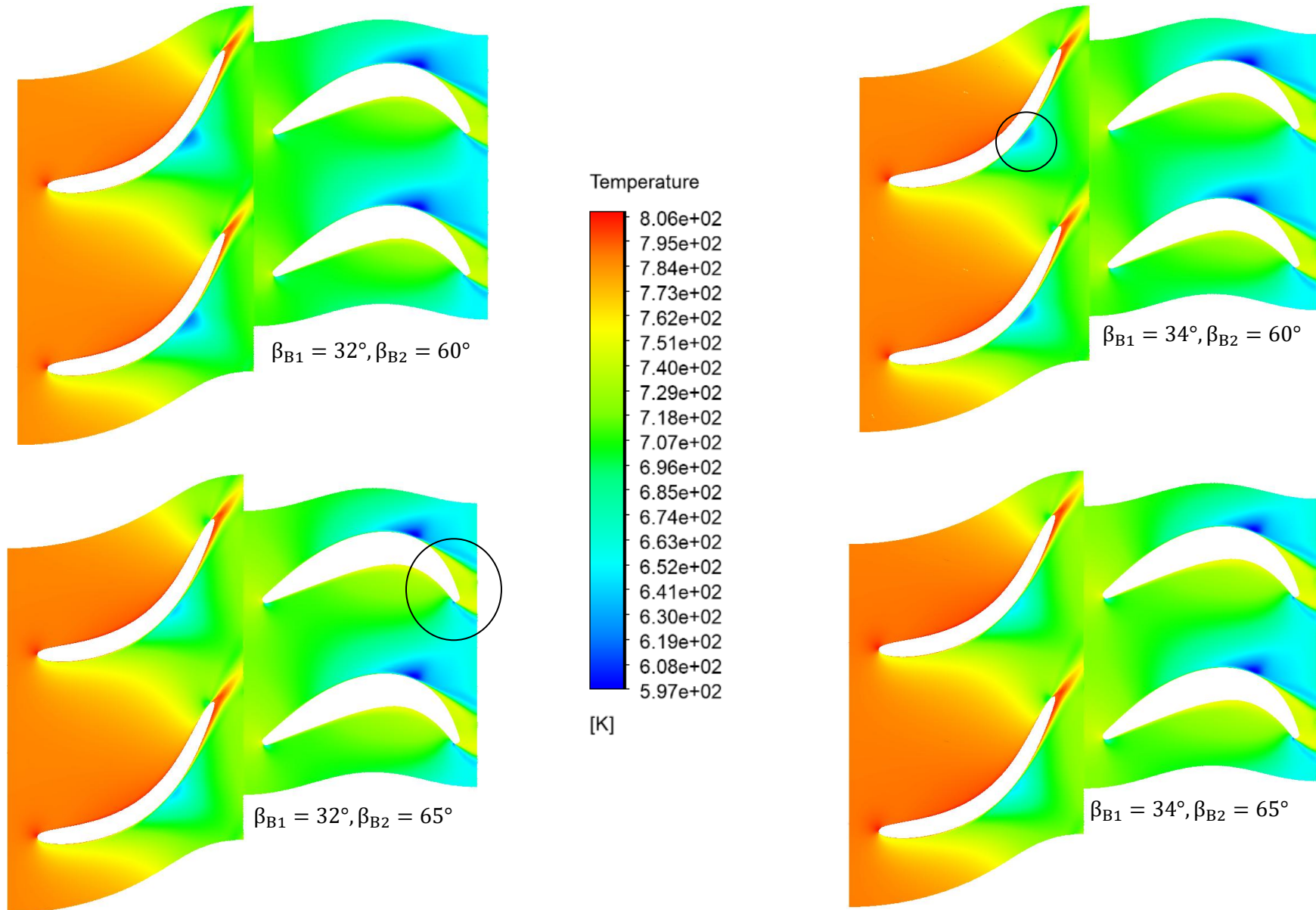
Across the full optimal simulations set in figure 6, the goal is to investigate how the flow is directed through the cascade passage. At the stator blade level, a repetitive pattern is observed: for a weak rotor outlet turning angle, a very low temperature wake-like under the stator and on top of the rotor blades is formed and displayed as a dark blue region that results when the boundary layer affects the stator mid chord walls because the rotor has extracted less work while the core flow maintained a relatively higher temperature. As the rotor turning angle is increased, two more effects become clearly visible, the strong flow deflection leads to higher energy extraction causing a higher drop in flow static temperature due to the expansion effect. Additionally, the aggressive flow turning elevates turbulence kinetic energy levels at the outlet of the rotor which causes the mixing effect that gradually smooths out the cool region until it almost homogenized

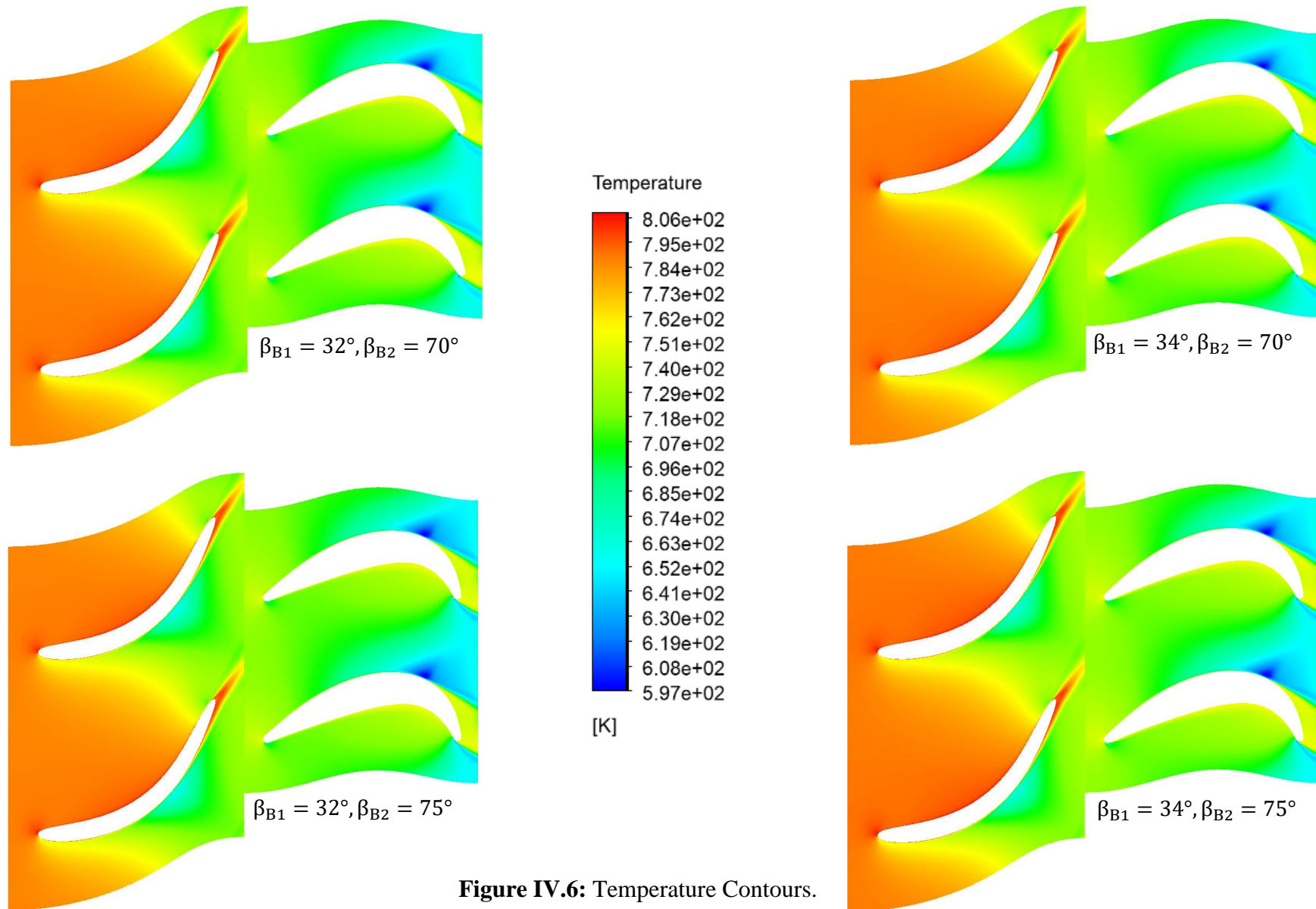
Also, the high temperature zone at the stator outlet arises due to viscous dissipation and local flow deceleration. Another persistent phenomenon at the rotor outlet occurs across all the simulations. Which is, a local high temperature zone formed due to the kinetic energy (figure 5) conversion into heat with friction and recirculation trapping the energy, this will lead to a localized temperature raise despite it happening in the expansion zone.



**Figure IV.5:** Rotor turbulent kinetic energy contour with the high intensity zone encircled.

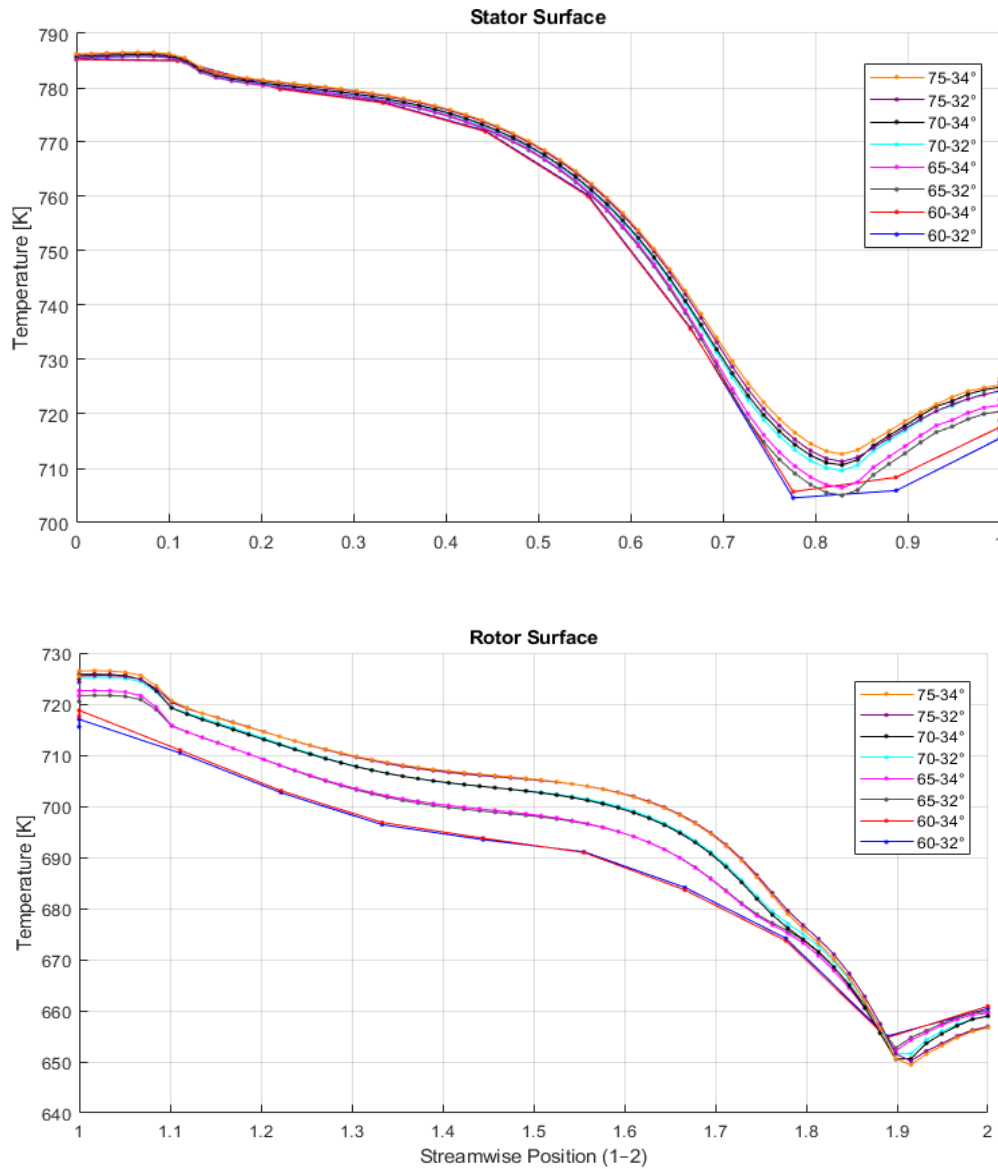






**Figure IV.6:** Temperature Contours.

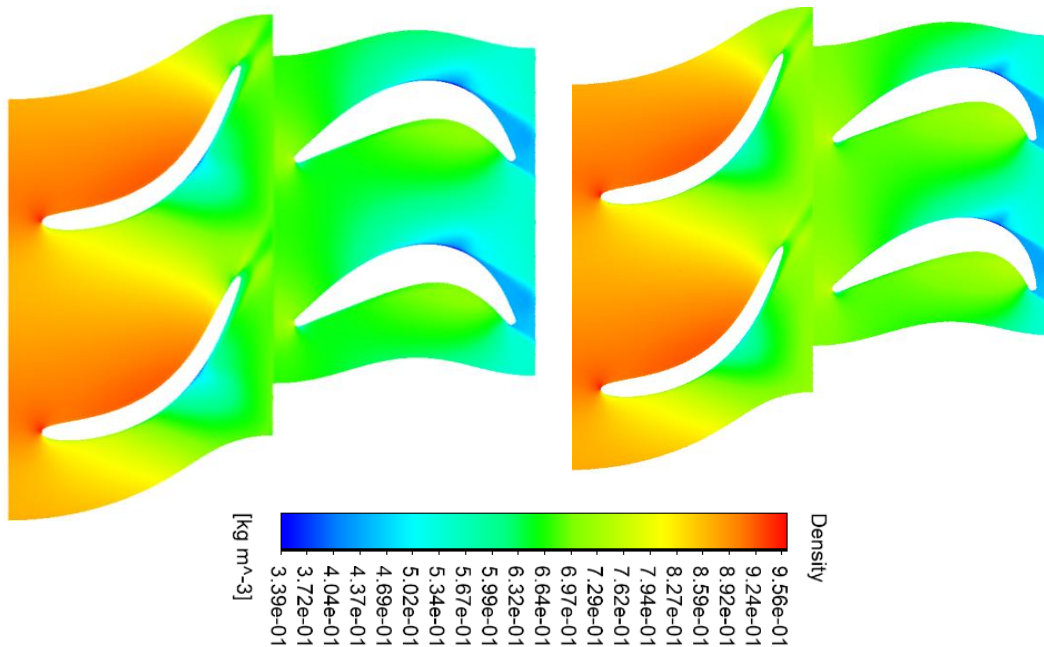
Figure 7 show the temperature distribution across the full axial turbine passage, the lines serve as a confirmation of the contour maps discussion, when the rotor deflects the flow with less sharpness, the temperature at the stator (0-1) outlet reaches a minimum. On the contrary, more aggressive flow turning causes the temperature to exit at a higher value due the fading of the low temperature wake (circle on the chart). By the cascade exit, all the lines converge uniformly, the orange line that represents the pair where the blades lean more sharply and deflect the flow harder yields the lowest exit temperature due to the maximization of the expansion cooling.



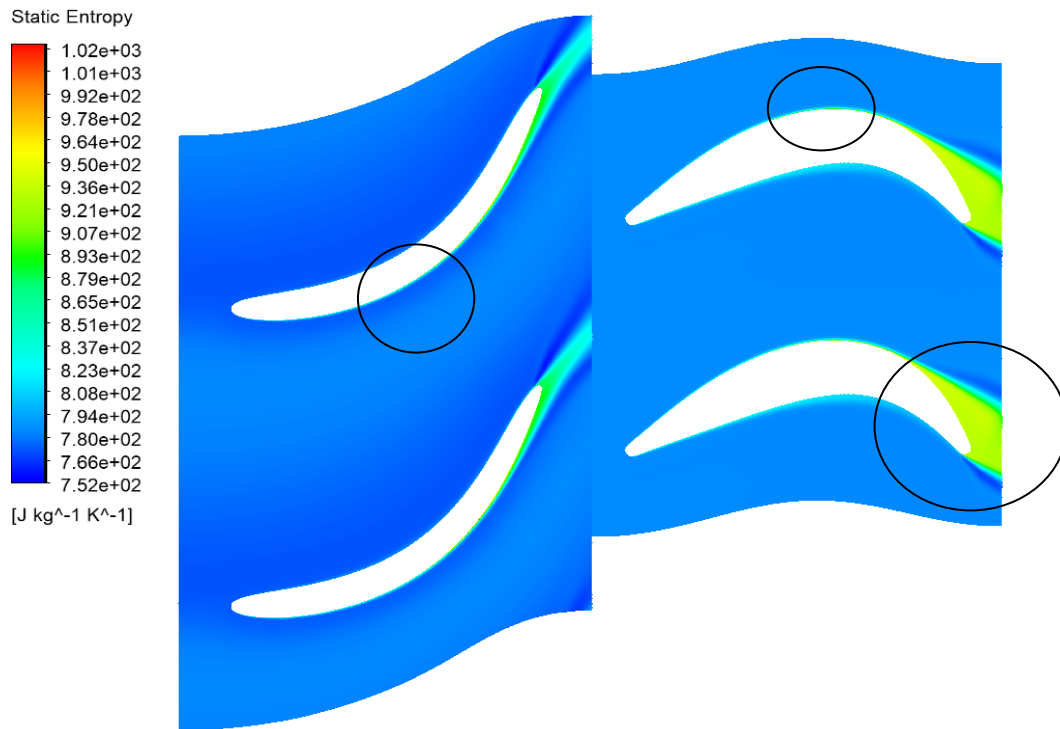
**Figure IV.8:** Temperature distribution across both blades.

## VI.2 Pressure Contours:

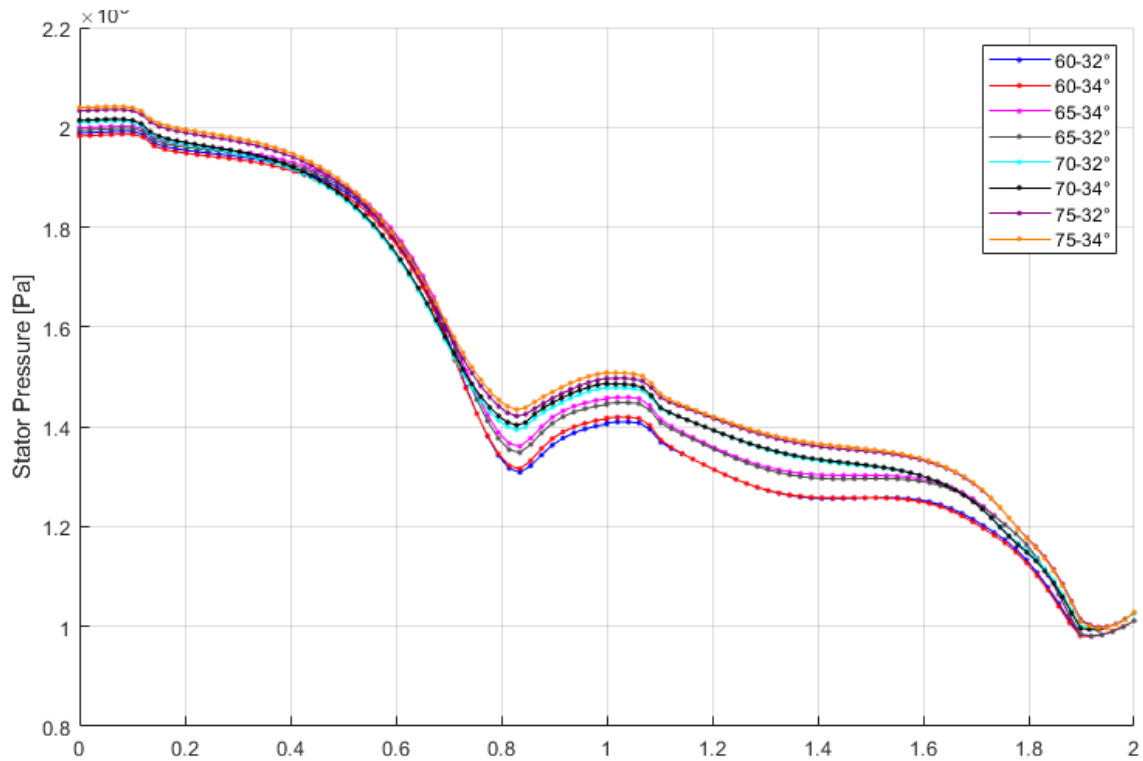
The contours, charts, and blade loading graphs displayed in this section present the pressure evolution through the domain. In all cases, low pressure (blue) zones can be clearly identified downstream on the trailing edges for both blades, specifically on the suction side (SS) for the stator and the suction side (SS) for the rotor. These zones are not the classical wakes in the sense of high entropy (figure 10) and low velocity (as will be further confirmed in the upcoming velocity analysis). Instead, the static pressure and density (figure 9) are low and tied to the turning degree of the generated geometry. At intense outlet rotor turning angles ( $-70^\circ$ ,  $-75^\circ$ ), these regions tend to gradually mix, diffuse and start to smooth-out with the surrounding flow resulting in a more uniform pressure distribution at the exit which is simplified in the chart of figure (11). Despite these changes, the pressure at the turbine cascade outlet remains stable between 1.1 and 1.2 bar which means that the geometry influences the trailing edges local flow behavior but not the overall outlet result, these wake-like dips and their evolution can be precisely identified using blade-loading graphs ‘figure (14)’ and for further clarification, they will be put in circles.



**Figure IV.9:** Density contours between a mild outlet angle ( $-60^\circ$ ) and an intense outlet angle ( $-75^\circ$ ).

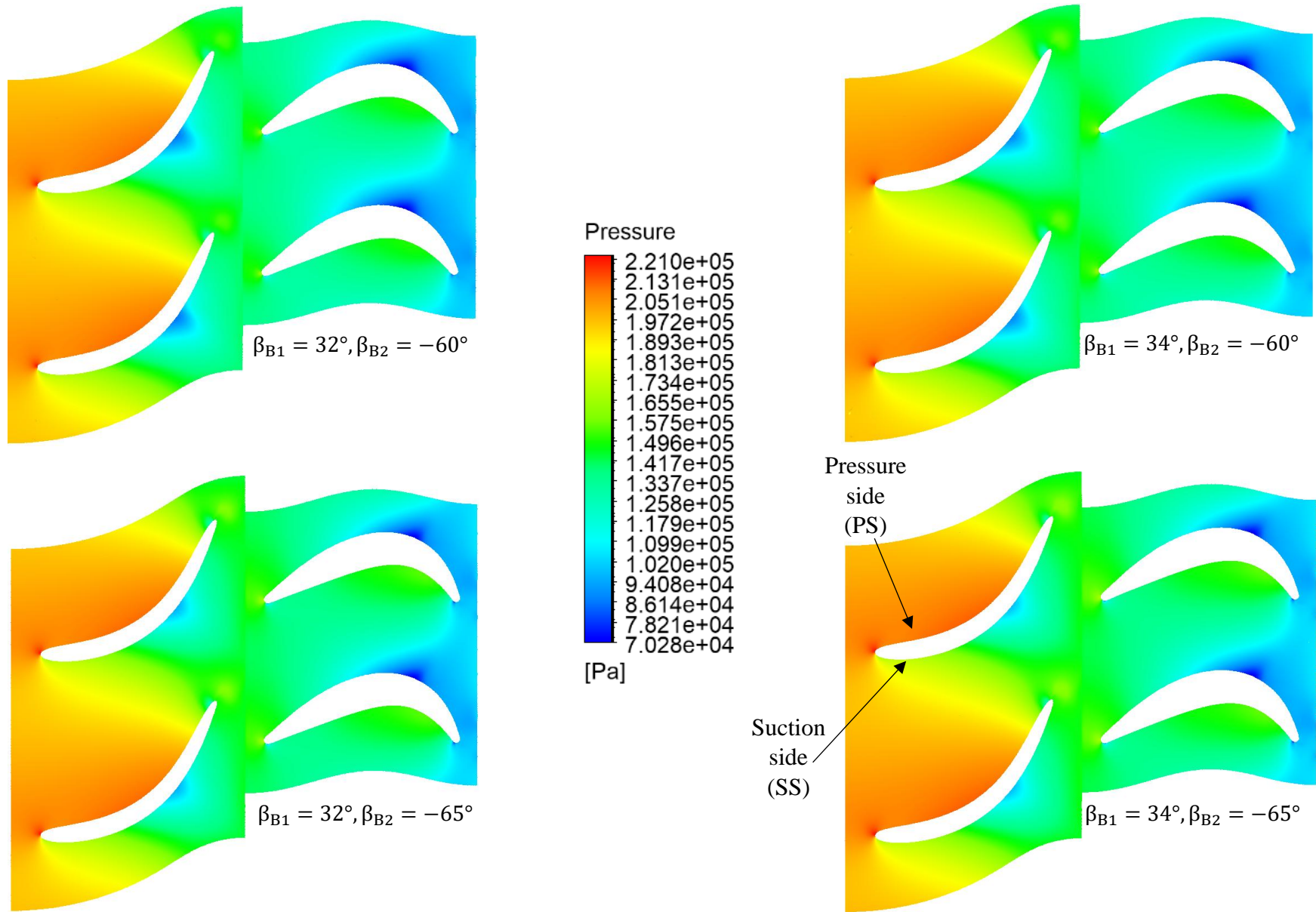


**Figure IV.10:** Entropy generation streamwise, the absence of losses in the wake-like zones, with higher value at the trailing edge outlet.



**Figure IV.11:** Pressure distribution for all cases.





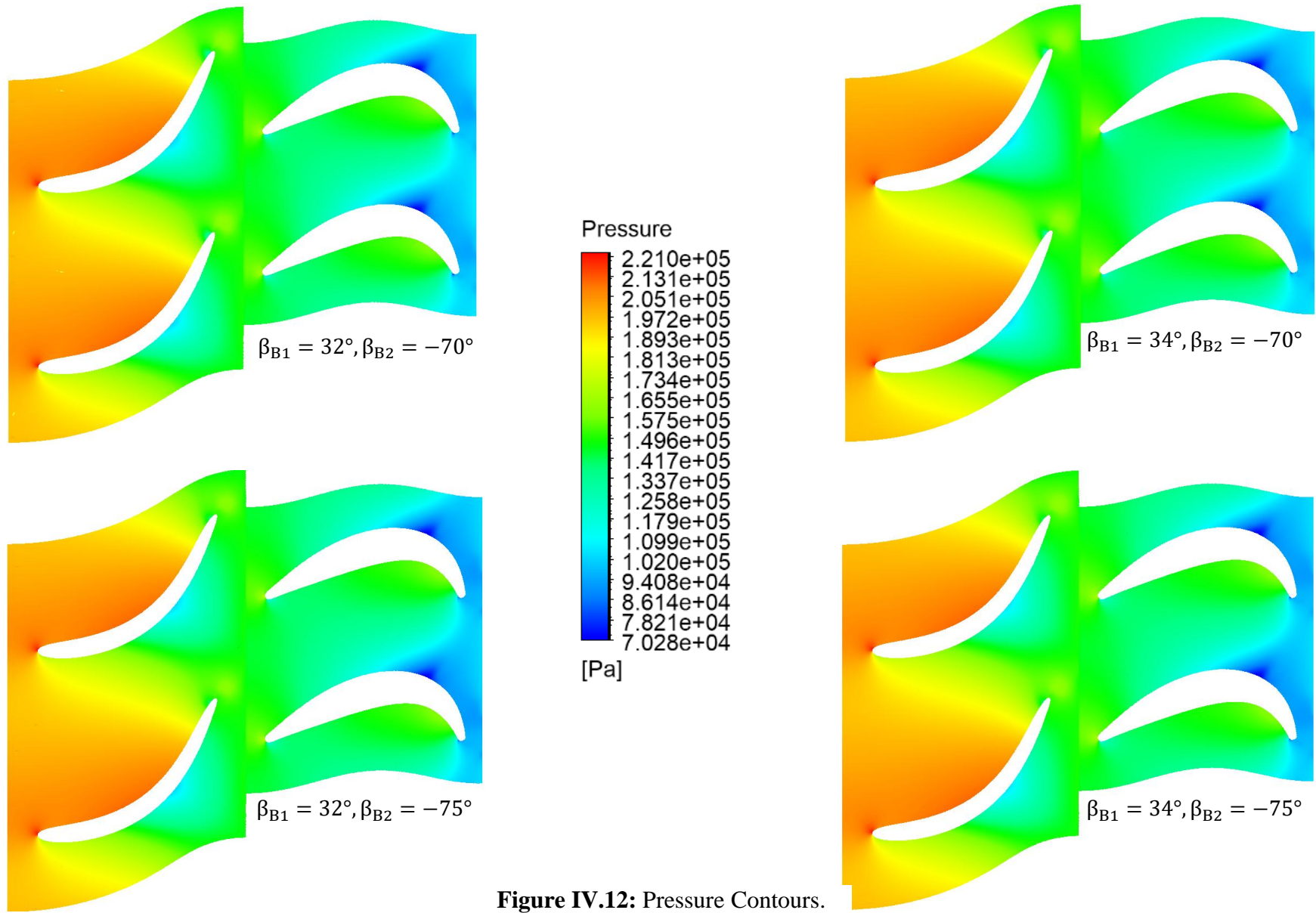


**Figure IV.12:** Pressure Contours.

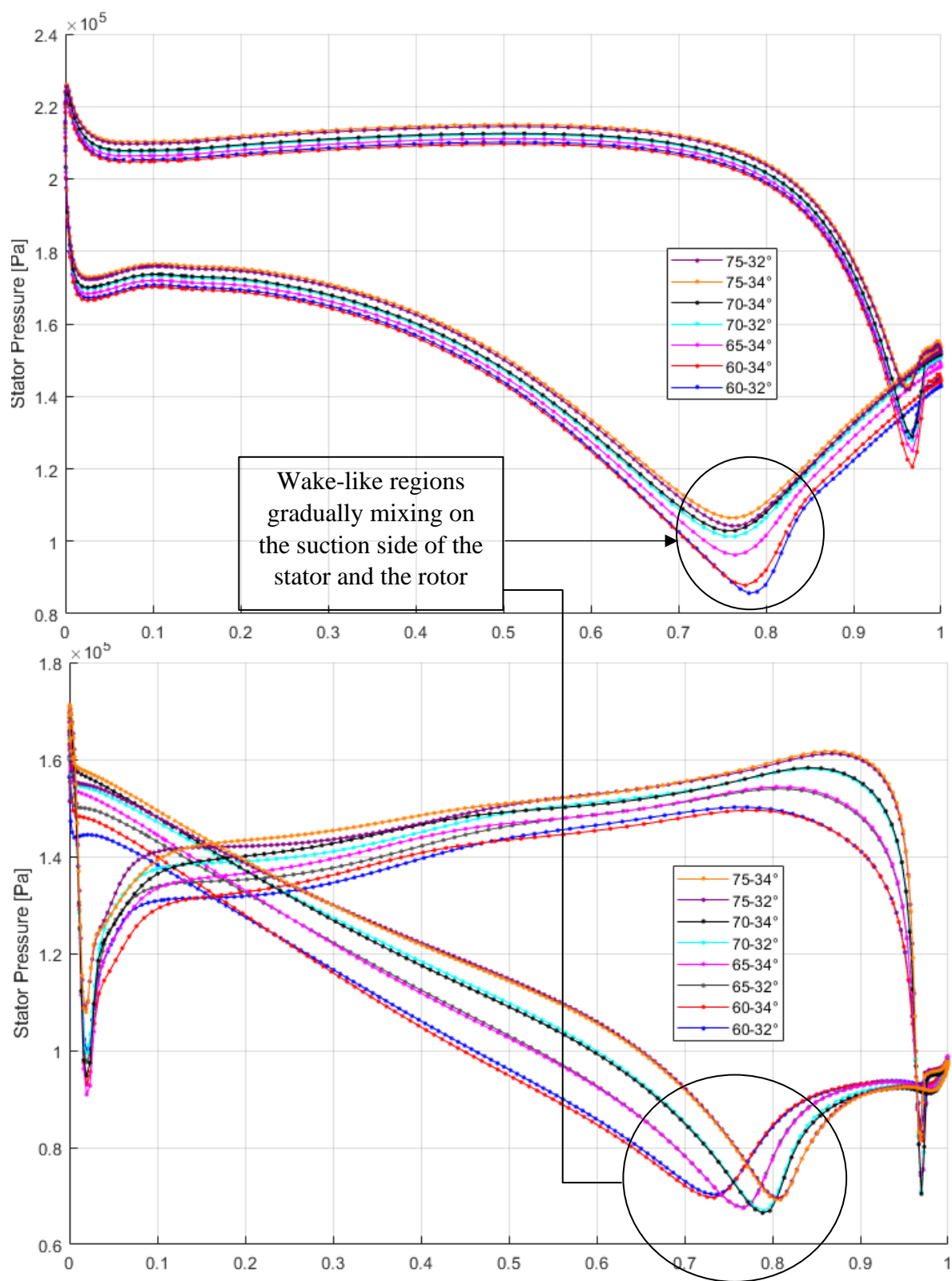


**Figure IV.14:** Blade pressure loading.



### **VI.3 Velocity, vortices and Mach contours**

Narrow high-speed zones form directly downstream of the blades which are not classical marked by deceleration or stagnation. Instead, these jet-like structures are driven by rapid turning where static pressure, density, and temperature drop sharply which signifies that the acceleration is caused by compressible isentropic expansion rather than any other mechanism. As the exit angle becomes steeper, the high-speed regions broaden, yet their maximum value tends to reduce (650 to 580 m/s) due to passage widening. These observations are further supported by the Mach contours, where supersonic pockets appear at the same regions (Mach exceeds 1). However, these pockets do not imply aerodynamic losses since they only occur if they are followed by shock waves or dissipative shear layers.

At the rotor outlet, distinct low velocity, subsonic vortex subsonic form on the suction side linked to a residual recirculation and secondary flows and it remains stable and localized but introduces elevated entropy indicating viscous dissipation. Also, the vortex coincides with the low static pressure outlet which suggests that it may also be influenced by an adverse pressure gradient. The presence of such phenomena suggests that the vortex is not merely a secondary flow feature but a core of localized aerodynamic losses likely resulting from the interaction of opposing shear layers and residual swirl.

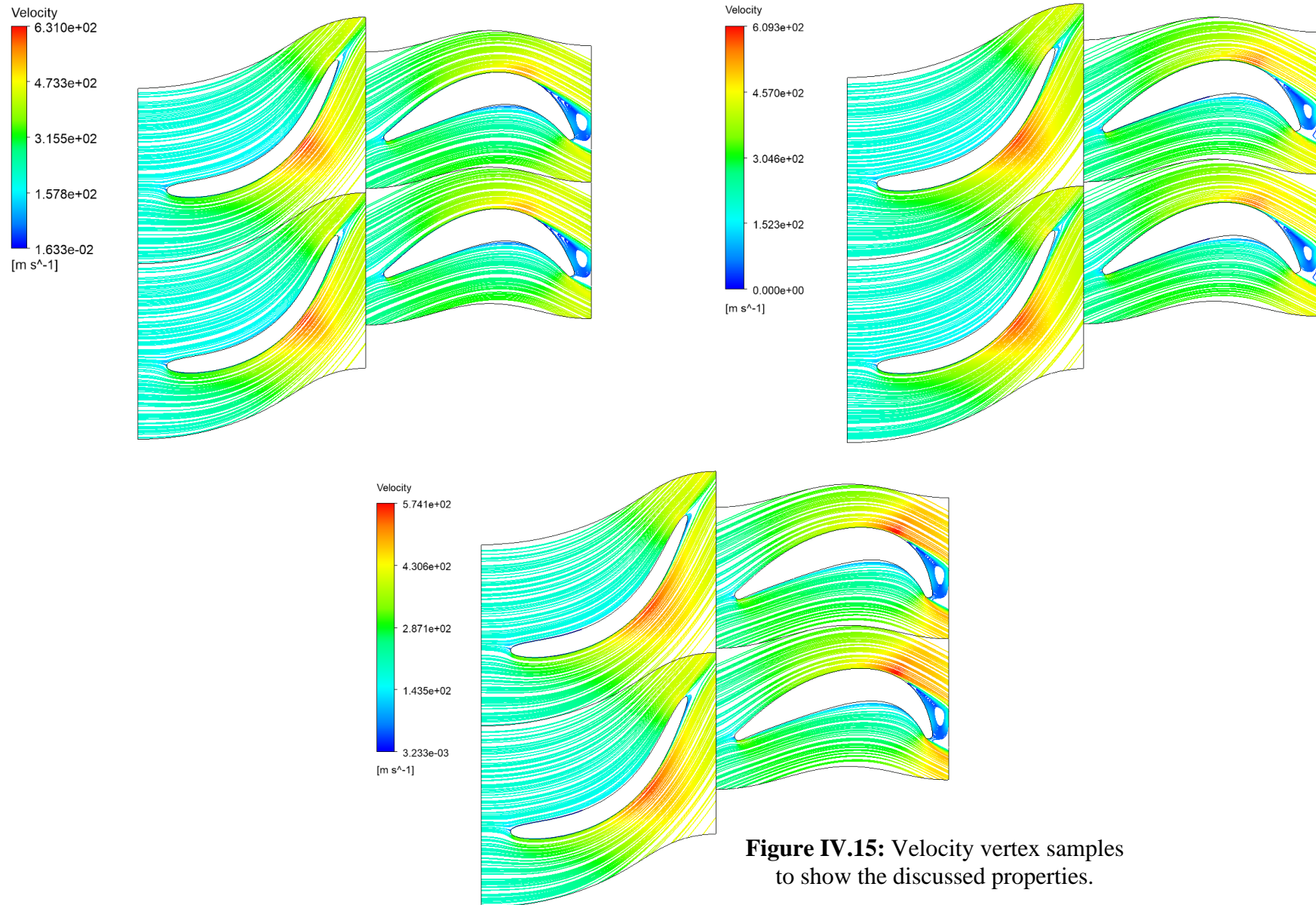


**Figure IV.15:** Velocity vertex samples to show the discussed properties.

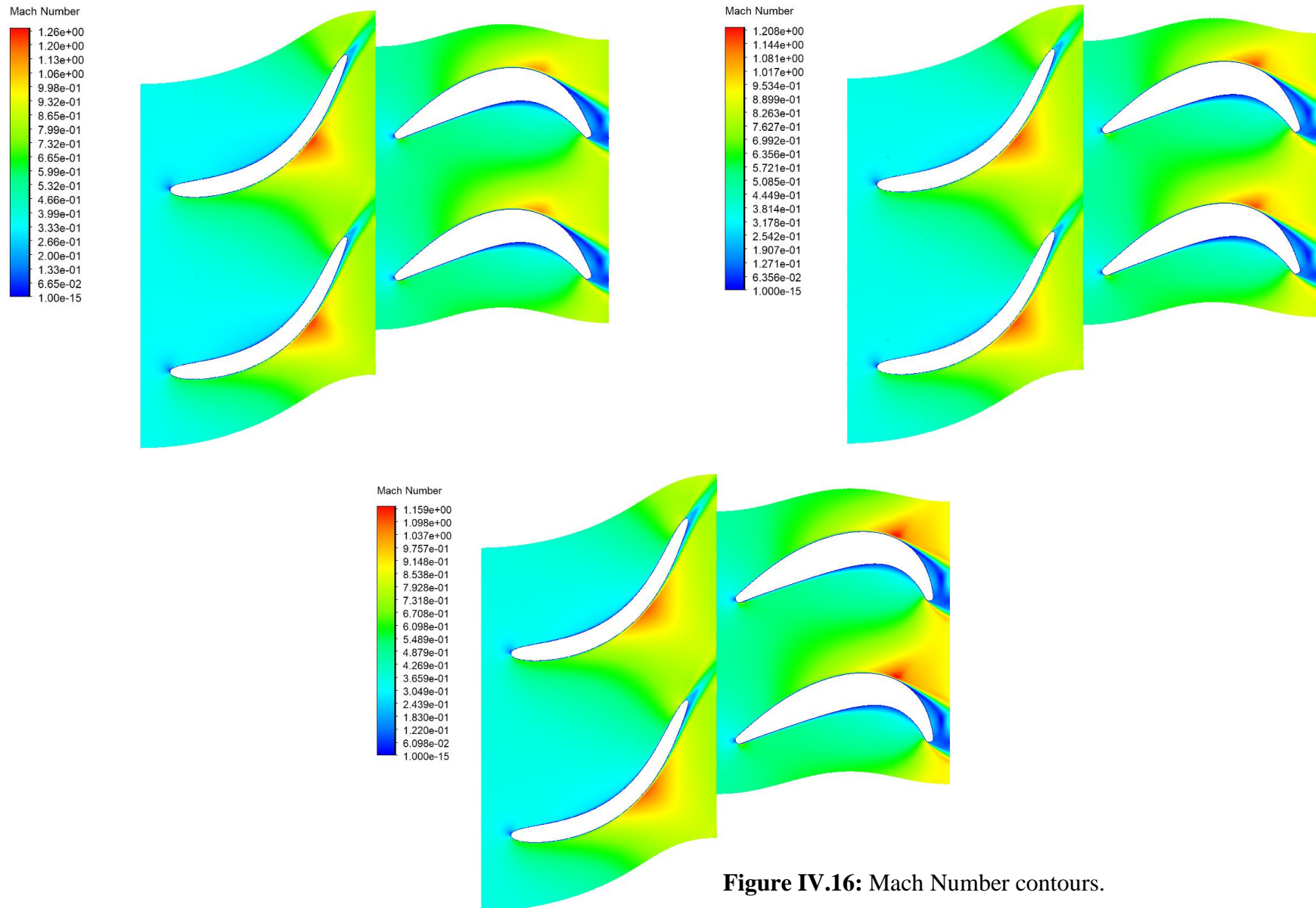


**Figure IV.16:** Mach Number contours.

## VII Micro to large turbine scaling

This section deals with the non-dimensional scaling of the micro axial gas turbine simulated in the thesis into a real-life large-scale axial gas turbine, the original to new parameters are:

$$38000 \text{ RPM} \rightarrow 3200 \text{ RPM}$$

$$\dot{m}_{\text{micro}} = 0.61 \text{ Kg/s} \rightarrow \dot{m}_{\text{NEW}}$$

As a quick reminder, all the essential parameters from CFturbo are as follows:

- Mass flow:  $\dot{m} = 0.61 \text{ Kg/s}$
- Rotational speed: 38000 RPM
- Degree of reaction:  $R=0.109$
- Flow coefficient:  $\varphi = 0.909$
- Work coefficient:  $\psi = 2.276$
- Hub diameter:  $dh1=0.136 \text{ m}$
- Tip diameter:  $dh2=0.114\text{m}$
- Total density:  $\rho = 0.887 \text{ Kg/m}^3$

The angular is expressed as:

$$\omega = \frac{2 \times \pi \times N}{60} \quad (\text{IV. 6})$$

So

$$\omega = \frac{2 \times \pi \times 38000}{60} = 3979.35 \frac{\text{rad}}{\text{s}}$$

❖ **The blade speed U:**

$$U = \omega \times r_{\text{mean}} \quad (\text{IV. 7})$$

With the mean diameter:

$$D_{\text{mean}} = \frac{dh1 + dh2}{2} = \frac{0.136 + 0.114}{2} = 0.125 \text{ m}$$

So, the mean radius:

$$r_{\text{mean}} = \frac{D_{\text{mean}}}{2} = \frac{0.125}{2} = 0.0625 \text{ m}$$

Then

$$U = 3979.35 \times 0.0625$$

$$U = 248.71 \text{ m/s}$$

❖ **The enthalpy difference:**

Using the work coefficient value from CFturbo:

$$\psi = \frac{\Delta h_{0-s} \times \eta_{tt}}{0.5 \times U^2} = \frac{\Delta h_0}{U^2} \rightarrow \Delta h_0 = \psi \times U^2 \quad (\text{IV. 8})$$

So:

$$\Delta h_0 = 2.276 \times 248.71^2$$

$$\Delta h_0 = 140785.77 \text{ J/Kg}$$

❖ **The volumetric flow rate:**

Using the general law of volumetric flow rate:

$$\dot{Q}_V = \frac{\dot{m}}{\rho} \quad (\text{IV. 9})$$

Then

$$\dot{Q}_V = \frac{0.61}{0.887} = 0.69 \frac{\text{m}^3}{\text{s}}$$

The simplifying hypothesis taken in this section are:

- ✓ All dimensions are scaled uniformly (geometric similarity)
- ✓ Non-dimensional coefficients similarity ( $\psi$ ,  $\varphi$ ,  $R$ )
- ✓ A constant blade speed to minimize centrifugal stresses
- ✓ Constant specific speed to preserve aerodynamic performance and geometry.
- ✓ The enthalpy drop is constant.

**VII.1 Turbine theoretical scaling****❖ The new mean diameter:**

Since the blade speed is kept constant:

$$U = \omega \times r_{\text{mean-large}} = \omega = \frac{2 \times \pi \times N_{\text{large}}}{60} \times \frac{D_{\text{mean-large}}}{2} \quad (\text{IV. 10})$$

So

$$D_{\text{mean-large}} = \frac{60 \times U}{\pi \times N_{\text{large}}}$$

$$D_{\text{mean-large}} = \frac{60 \times 248.71}{\pi \times 3200}$$

$$D_{\text{mean-large}} = 1.48 \text{ m}$$

And

$$r_{\text{mean-large}} = \frac{1.48}{2} = 0.74 \text{ m}$$

**❖ The new flow rate:**

Knowing that the law of specific speed  $N_s$  for the small-scale turbine is written as:

$$N_s = \text{RPM} \times \frac{\sqrt{\dot{Q}_V}}{\Delta h_0^{3/4}} \quad (\text{IV. 11})$$

So,

$$N_s = 38000 \times \frac{(0.69)^{0.5}}{140785.77^{3/4}}$$

finally

$$N_s = 4.34 \quad (\text{IV. 12})$$

Now, to properly scale it and following the assumption made above:

$$N_{s\text{-Large}} = N_s = \text{RPM} \times \frac{\sqrt{\dot{Q}_{V\text{-Large}}}}{\Delta h_0^{3/4}} = 4.34$$

And the flow rate is:

$$\dot{Q}_{V\text{-Large}} = \left( \frac{\Delta h_0^{3/4} \times 4.34}{\text{RPM}} \right)^2 = \left( \frac{140785.77^{3/4} \times 4.34}{3200} \right)^2$$

$$\dot{Q}_{V\text{-Large}} = 97.17 \frac{\text{m}^3}{\text{s}}$$

And the new mass flow rate is:

$$\dot{m}_{\text{Large}} = \rho \times 97.17 = 0.887 \times 97.17$$

$$\dot{m}_{\text{Large}} = 86.19 \frac{\text{Kg}}{\text{s}}$$

## VIII Artificial Neural Network Results

The neural network program performed in MATLAB consists of 2 inputs (blade inlet and outlet angles) with 2 hidden layers with 15 neurons for each one, and an output layer as shown in figure (17). The regression plots displayed down below for the training, validation, and test phases show a close match between the ANN predicted results and the actual experimental values from the CFD simulations, formed in pair that cross paths and displayed in black circles.

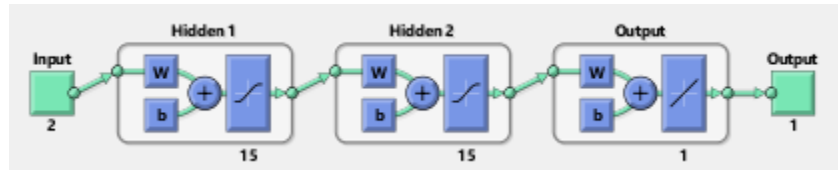


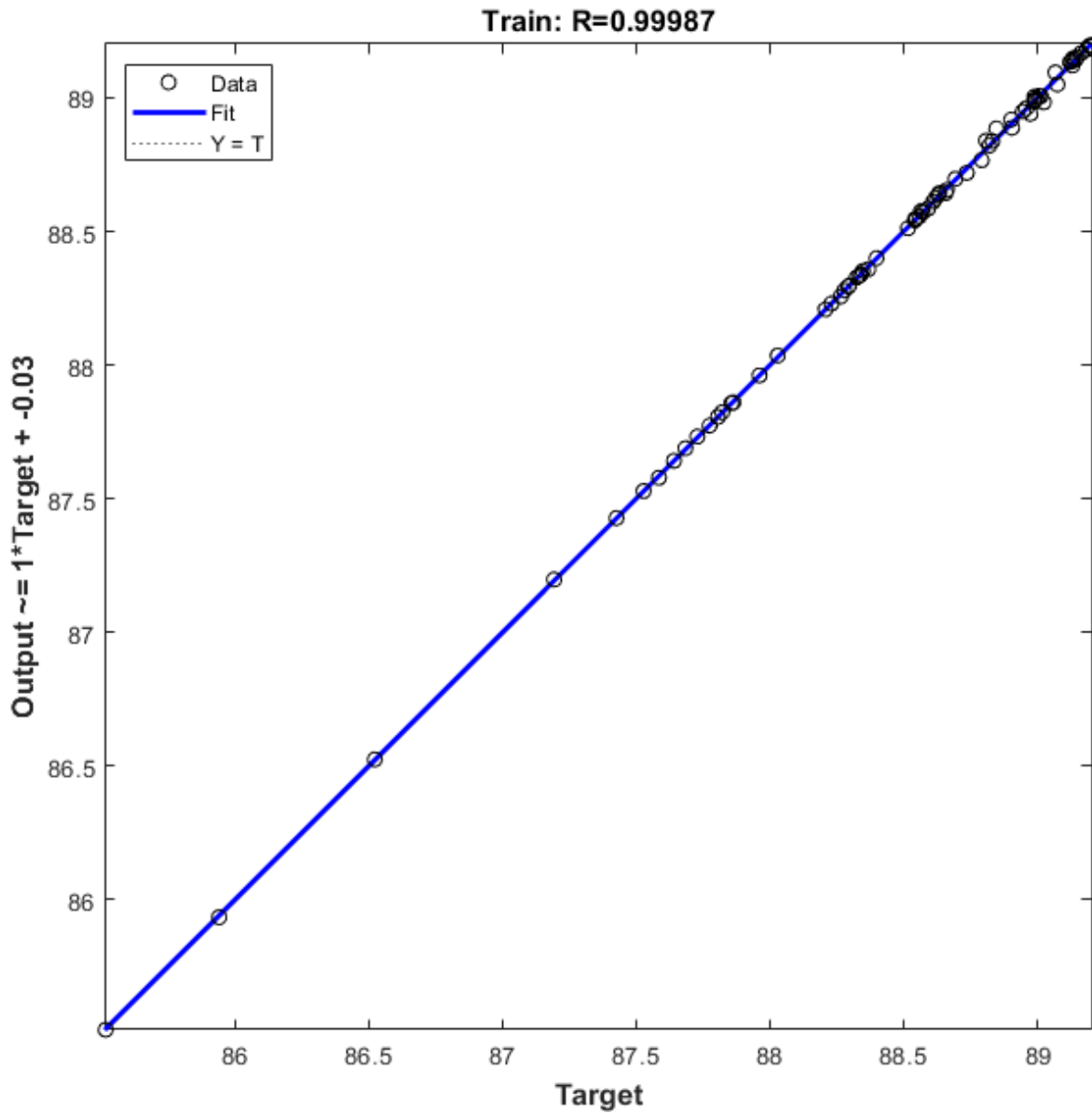
**Figure IV.17:** Neural network diagram.

During the training phase, the majority of points fall along the  $Y=T$  (dashed) that represents the ideal predictions and the regression blue line (noting that both lines are superimposed), the model ability to clearly understand and capture the key patterns and the nonlinear relationships mappings that gives the closest and most accurate predictions.

Another thing that confirms this is the correlation coefficient  $R=0.99987$  that indicates the near-perfect linear accordance. The output fit line is mathematically expressed as follows:

$$\text{Output} = 1 \times \text{Target} \pm 0.03 \quad ( )$$

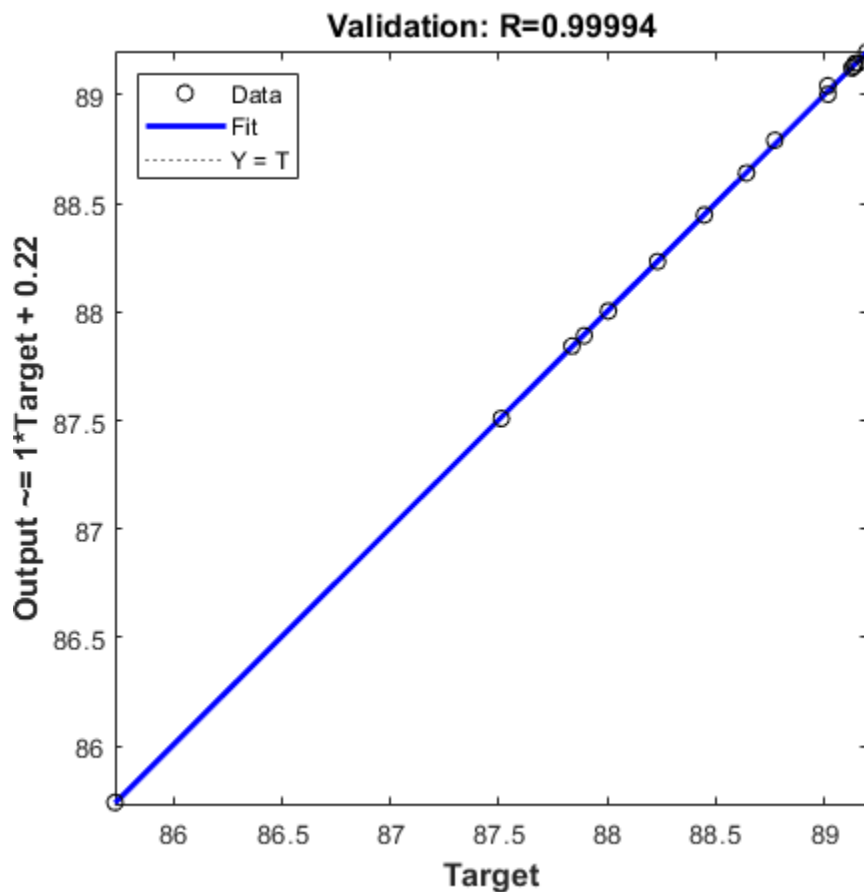
This equation with the target multiplied by 1 proves that the ANN is learning the patterns with a linear perfection without any distortion but with a small over or under-prediction of 0.03 which is generally negligible.



**Figure IV.18:** Regression Training graph.



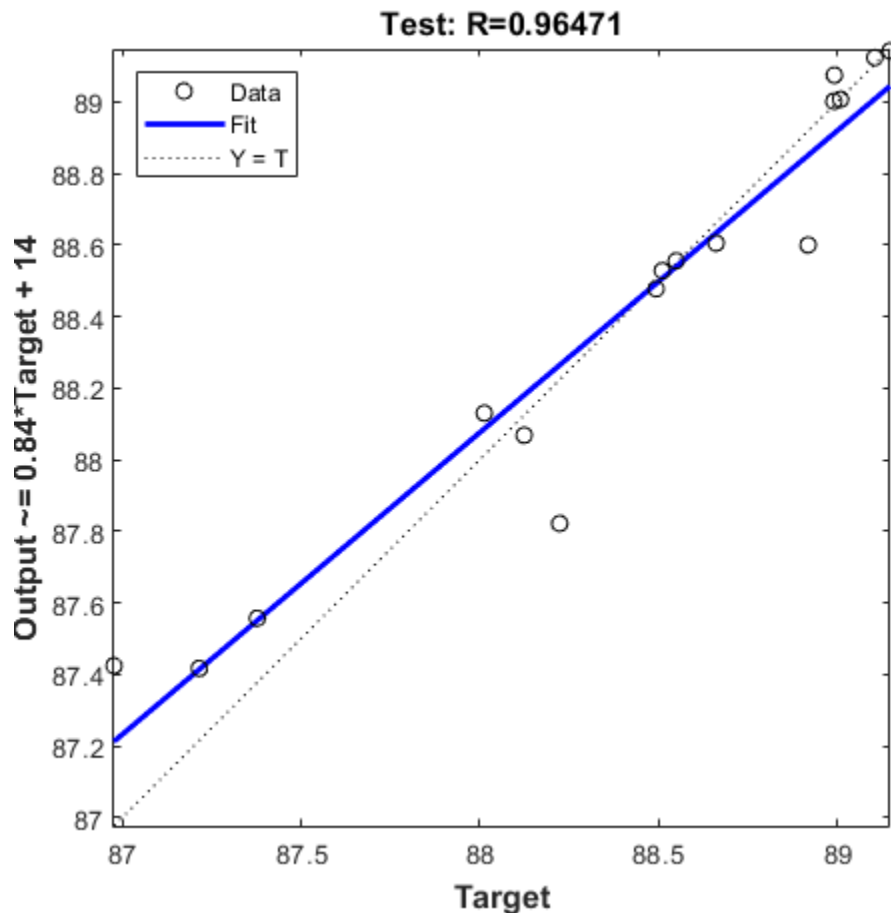
During the validation phase, the model was presented with a different portion of experimental samples different from the first phase to check on the model capability to achieve the desired results, its regression results in figure (19) shows that the majority of validation points cluster around both lines with a correlation coefficient  $R=0.99994$  and an over-estimation of 0.22. this further tells how well the models is predicting unseen cases of the same sample datasheet.



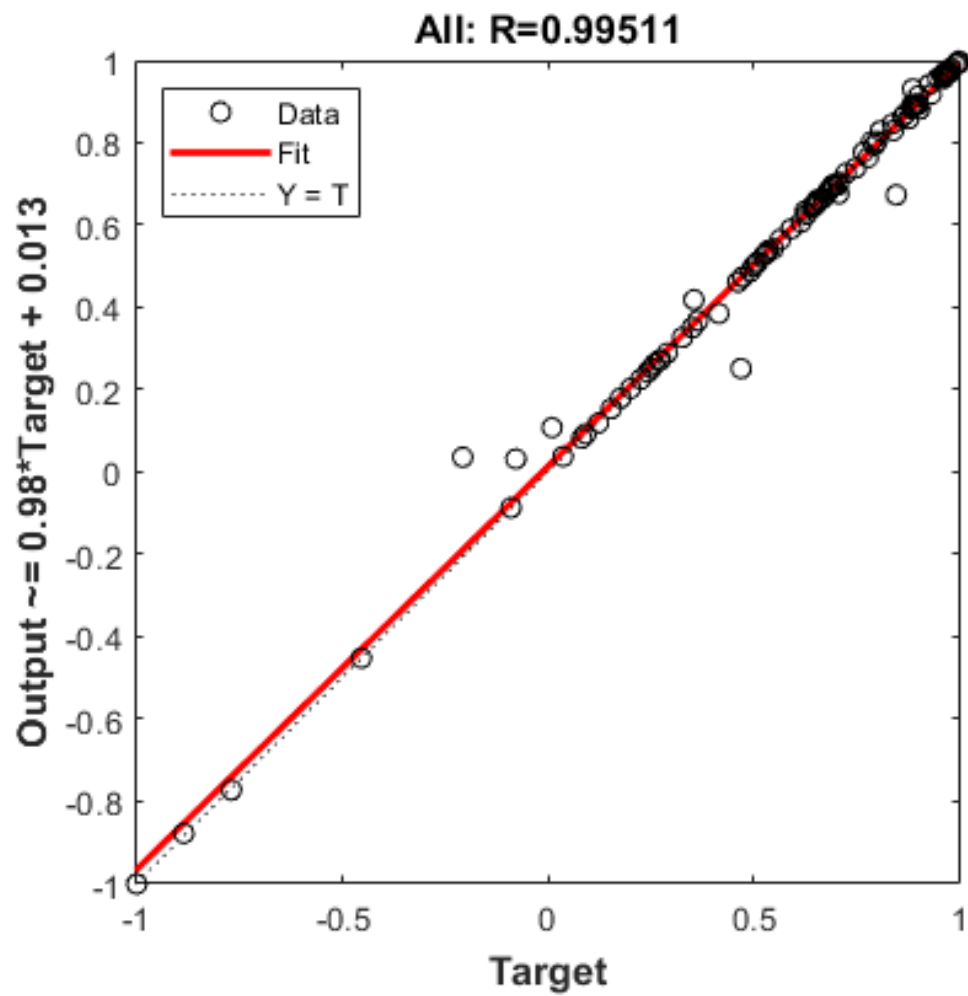
**Figure IV.19:** Regression validation graph.

For the final testing phase, the model is again presented with the remaining samples set to provide an unbiased assessment of the model's predictive power on totally unseen cases. The regression plot that while the overall fit remains relatively strong, the dashed and regression lines start slightly apart, intersect mid-span, and further separate which means that the model sometimes overpredict and sometimes underpredict with the points closing in on both lines and some clearly far.

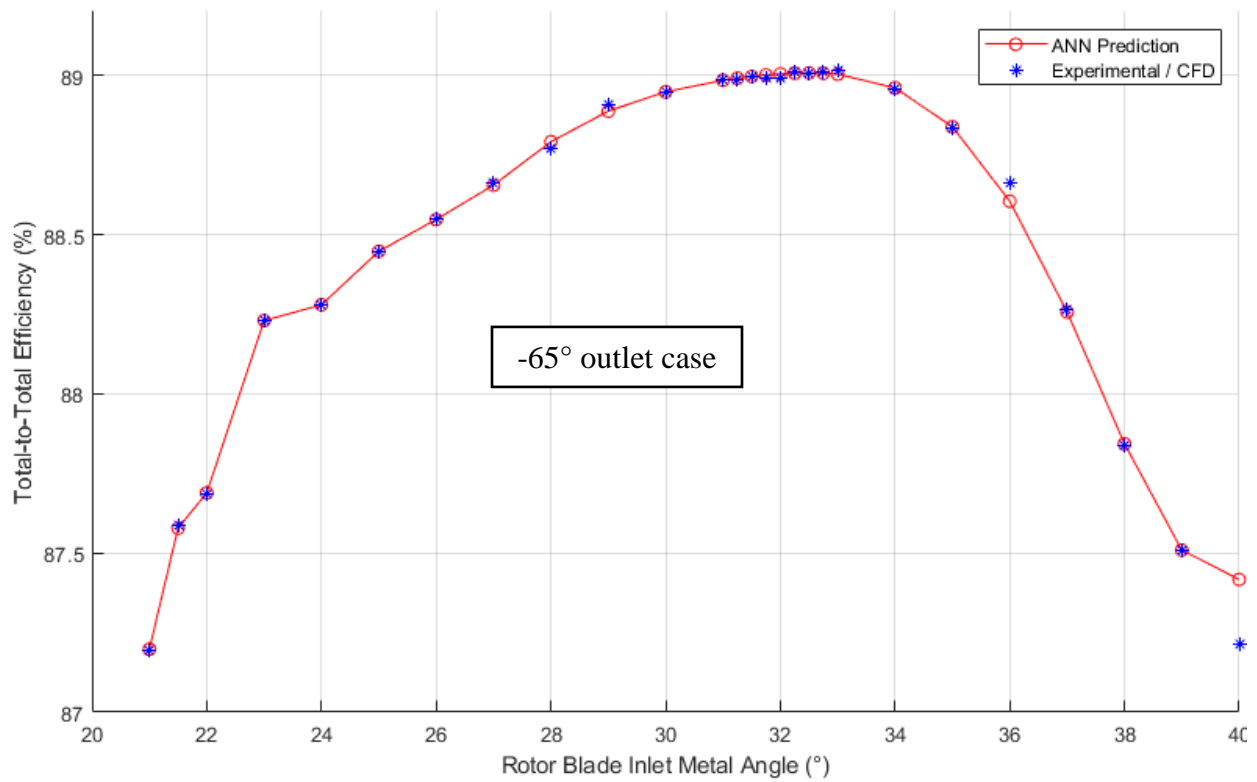
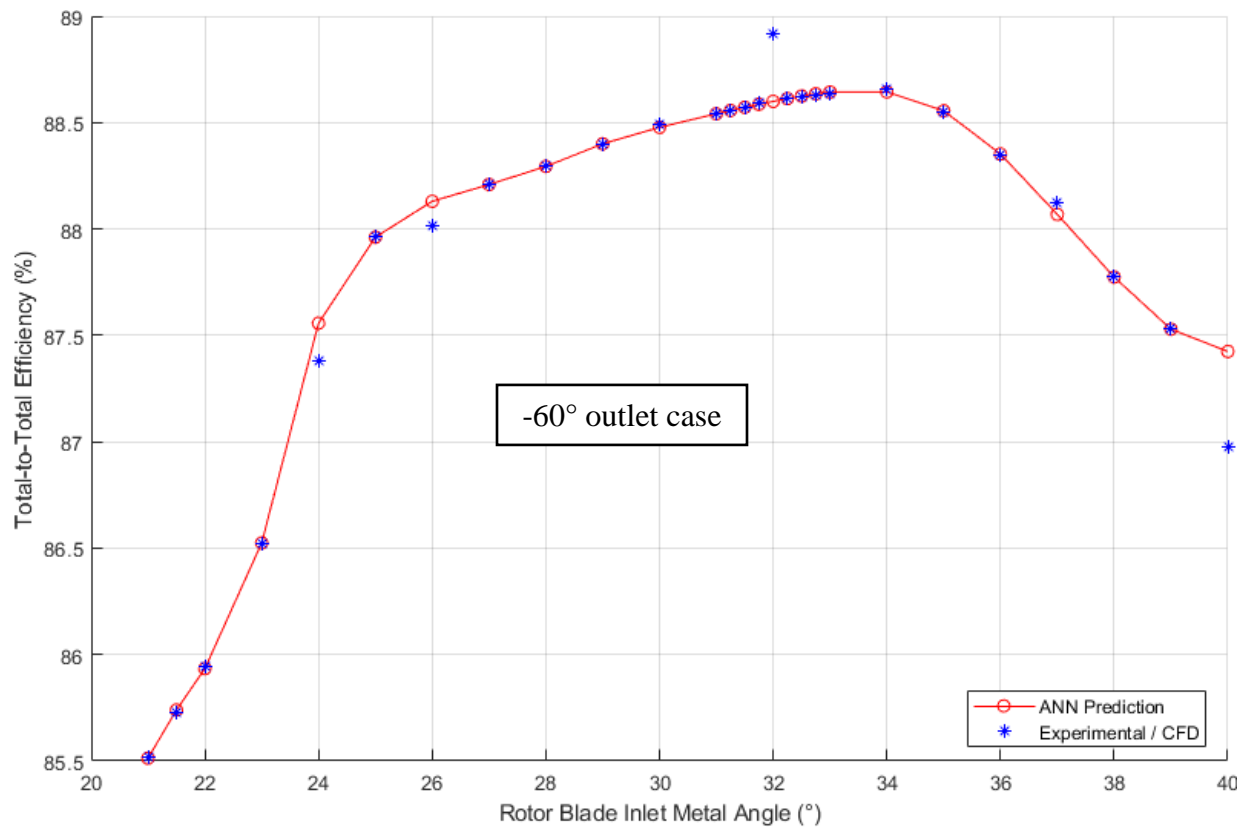
This is primarily linked to the very limited data set of 108 samples that causes the program to not perfectly learn, but the correlation coefficient still has a very good value of 0.96471 and the target factor multiplied by 0.84, a value that can be reliable but increases to near linear limits if the ANN is given enough data (generally in the order of thousand to tens of thousands). The global regression plot shows a strong alignment between the model's outputs and true results, the output nearly is linear with an overprediction of 0.013 and the  $Y=T$  line almost coincide. The biggest portion of data points fall very close to these lines indicating the overall accuracy and performance of the model that have a correlation coefficient of 0.99511. A final set of figures (Figure 22) will be presented to further confirm the discussed remarks, each figure proves that the ANN values match closely the CFD results expect for a small number of points with the peak reach at an inlet angle of  $32^\circ$ . Even though this program did well with such a small data-base, future improvements are needed to optimize it.



**Figure IV.20:** Regression Testing graph.



**Figure IV.21:** Global Graph.



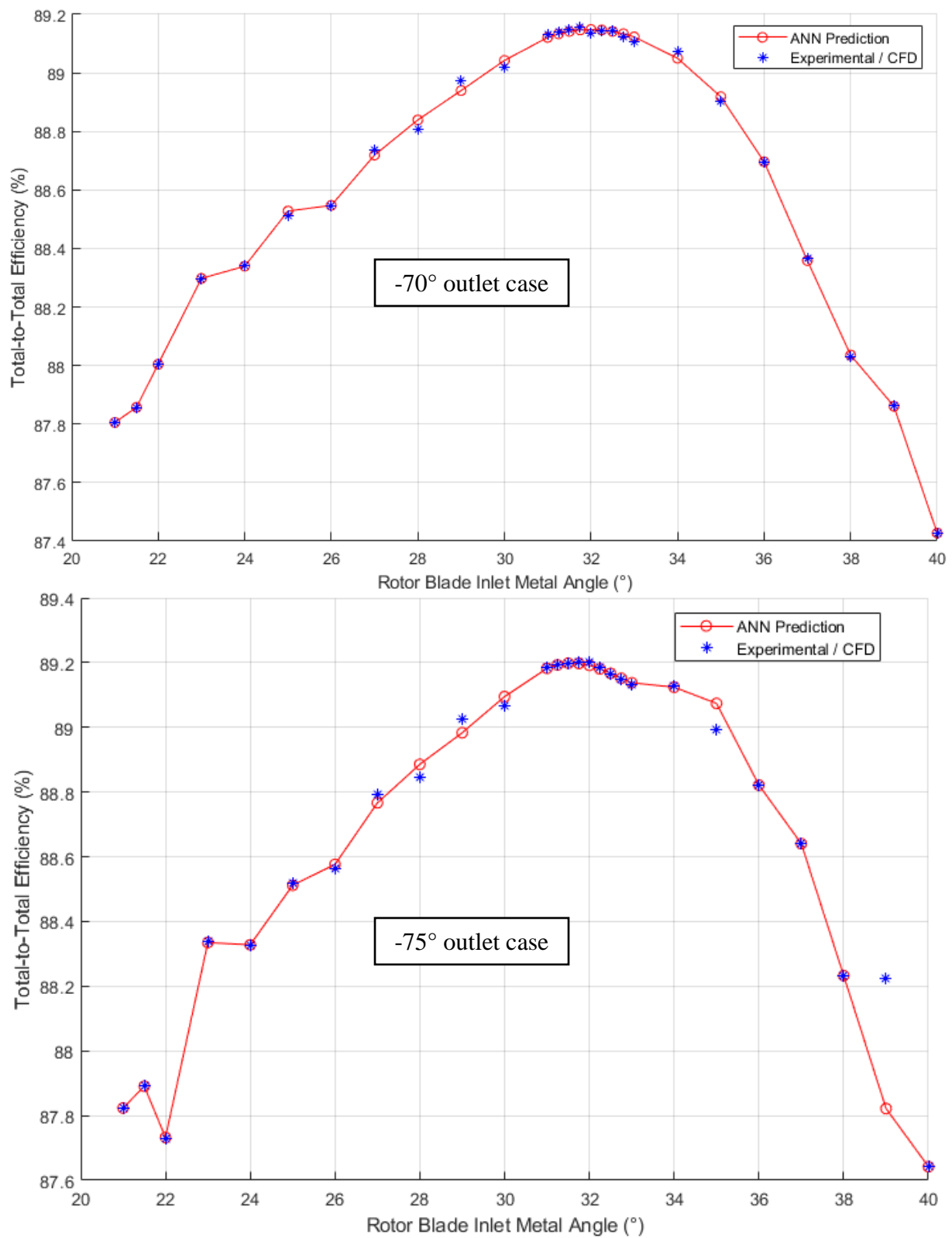


**Figure IV.22:** Prediction vs reality results.

## **IX Conclusion**

This last chapter focused on the detailed simulations of various micro axial turbine cascade geometries to analyze efficiency, thermodynamic, and aerodynamic behaviors with a clear goal to optimize and increase the overall total to total efficiency. Additionally, some NACA profile validations were performed to determine the degree of accordance to the literature and to safely utilize the models for the simulations mentioned above. The theoretical scaling of these small cascades into the large industrial sizing, the results show that despite the reduction in rotational speed, the proper adjustments to geometric dimensions and flow variables allow to preserve the flow structure and performance properties. Finally, this chapter concludes with an artificial neural network program to compare its predictive power to the actual real results.

## General Conclusion

### General Conclusion

Enhancing the overall performance and output of turbomachinery is a very important goal in modern engineering researches. This thesis focused on improving the total-to-total efficiency of a small-scale axial gas turbine by altering its 3D geometry multiple times and analyzing how the flow behaves using a combination of numerical methods and machine learning model.

The results of such a study demonstrated that the change in blade angles have a significant impact on the overall output. These results helped identify that the highest efficiencies with lowest aerodynamic losses (reduced secondary vortex formation, expansion pockets, and chaotic flow path) are attended when all the rotor outlet blade metal angles are paired with an inlet metal angle of  $32^\circ$  or  $34^\circ$ . furthermore, the Artificial Neural Network proved to be a reliable predictive tool, bridging the gap between real data and predicted outputs with the best possible accuracy though it remained dependent on the quality and quantity of the data fed to it.

Despite the promising results, the research faced some limitations since the simulations were based on the steady-state and ideal gas assumptions which may not capture the real complex flow behavior alongside the geometrical simplifications neglecting the real 3D effects. Also, the ANN was trained on a very small dataset which affects its performance outside the studied range. All these factors suggest a more advanced modeling and better validation for future work.

### Perspectives

This study opens several doors for future research opportunities that could even enlarge the understanding, some of these ideas are listed down below:

- ✓ The influence of mass flow rate on performance.
- ✓ The impact of transient flow regimes.
- ✓ The conception of a laboratory-scale prototype or a test bench to validate the results.
- ✓ implementation of more complex turbulence models like the LES or DES.
- ✓ aeroelastic analysis to study the blade deformation for various operating loads.
- ✓ increasing the dataset of simulation values to make the ANN model predict even the uncalculated cases.
- ✓ Applying real gas models and performing 3D blades study.



## References

## REFERENCES

---

- [1] Kadambi, V., Prasad, M. (2013). Principles of Turbomachinery. In: Kadambi, V., Prasad, M. (eds.). Turbomachinery (3rd ed., pp. 1-36). New Academic Science Ltd.
- [2] Dixon, S. L., & Hall, C. A. (2010). Classification of Turbomachinery. In: Fluid Mechanics and Thermodynamics of Turbomachinery (6th ed., pp. 1-27). Butterworth-Heinemann.
- [3] Kocak, G., & Durmusoglu, Y. (2018). Energy efficiency analysis of a ship's central cooling system using variable speed pump. *Journal of Marine Engineering & Technology*, **17**(1), 43–51. <https://doi.org/10.1080/20464177.2017.1283192>
- [4] Venkanna, B.K. (2009). Fundamentals of Turbomachinery. New Delhi (India): PHI Learning Private Limited. Chapter 1, pp. 1-57.
- [5] Bouzir, M. K. E. (2025). Geometries of the axial turbine generated using CFturbo 23.2. Self-produced using CFturbo software.
- [6] CFturbo GmbH. (2023). CFturbo Software (Version 23.2) [Software]. Available at: <https://www.cfturbo.com>
- [7] Korpela, S. A. (2019). Axial Turbines. In *Principles of Turbomachinery* (2nd ed., pp. 247–305). Hoboken, NJ (USA): John Wiley & Sons, Inc.
- [8] Cengel, Y. A., & Cimbala, J. M. (2017). In *Fluid mechanics: Fundamentals and applications* (4th ed., pp. 794–869). New York (USA): McGraw-Hill Education.
- [9] Saravanamutto, H. I. H., Rogers, G. F. C., Cohen, H., Straznicky, P. V., & Nix, A. C. (2017). Axial and radial flow turbines. In *Gas Turbine Theory* (7th ed., pp. 337–408). Harlow (UK): Pearson Education.
- [10] Roy, B., & Pradeep, A. M. (2015). *Turbomachinery Aerodynamics – Lecture 20*, (p. 21). NPTEL – IIT Bombay. Retrieved from <https://archive.nptel.ac.in/courses/101/101/101101058/>
- [11] Lakshminarayana B. (1996). Fluid Dynamics and Heat Transfer of Turbomachinery. John Wiley & Sons, Inc., New York, 846 p.

## REFERENCES

---

- [12] Razak, A. M. Y. (2007). Chapter 5. Industrial Gas Turbines: Performance and Operability (pp. 120-136). Woodhead Publishing.
- [13] NPTEL. (n.d.). GAS TURBINE – Figure 13.3a: Schematic diagram of flow through a turbine blade passage. Retrieved from:  
  
[https://archive.nptel.ac.in/content/storage2/courses/112104117/chapter\\_5/4\\_19.html](https://archive.nptel.ac.in/content/storage2/courses/112104117/chapter_5/4_19.html).
- [14] Turbomachinery Education. (n.d.). Basic geometric and aerodynamic angles of profile cascade (Section 3.6). Retrieved from <https://turbomachinery.education/shapes-of-blades-and-flow-parts-of-turbomachines.html#264>.
- [15] Abbott, I., & Doenhoff, A. (1959). Theory of wing sections, including a summary of airfoil data. New York: Dover Publications, Inc.
- [16] Japikse D. (1997). Introduction to turbomachinery. Oxford: Oxford University Press.
- [17] Mattingly J., Heiser W., Pratt D. (2002). Aircraft Engine Design. Reston: American Institute of Aeronautics and Astronautics.
- [18] Pfleiderer C., Petermann H. (2005). Strömungsmaschinen. Berlin, Heidelberg, New York: Springer Verlag.
- [19] Breeze, P. (2016). Gas Turbine Power Generation. Chapter 4: pp. 31–42. Elsevier, Oxford.
- [20] Wikiversity. (n.d.). Jet engine Bernoulli's Equation [Image]. Retrieved March 2, 2025, at 19:32 from [https://en.wikiversity.org/wiki/File:Jet\\_engine\\_Bernoullis\\_Equation.svg](https://en.wikiversity.org/wiki/File:Jet_engine_Bernoullis_Equation.svg).
- [21] Linquip. (n.d.). Cross-section of an industrial gas turbine [Image]. Retrieved March 2, 2025, at 19:34 from <https://www.linquip.com/blog/gas-turbine-parts-components/>.
- [22] Taghavi Zenouz R., Abiri S.M.M. Aerodynamic design of a high-efficiency two-stage axial turbine, using streamline curvature method and performance optimization by clocking of stator blades. In: The Aeronautical Journal, 2024, 128, pp. 1814–1843.

- [23] Souverein, L., Veggi, L., Sudhof, S., Behr, R., & Haidn, O. (2017). On the effect of axial turbine rotor blade design on efficiency: A parametric study of the Baljé-diagram. 7th European Conference for Aeronautics and Space Sciences (EUCASS). DOI: 10.13009/EUCASS2017-241
- [24] Zhang C., Janeway M. Optimization of Turbine Blade Aerodynamic Designs Using CFD and Neural Network Models. In: Int. J. Turbomach. Propuls. Power, 2022, 7, 20.
- [25] ASGARSHAMSI, Abolhassan; HAJILOUY-BENISI, Ali; ASSEMPOUR, Ahmad; POURFARZANEH, Hossein. Multi-Point Optimization of Lean and Sweep Angles for Stator and Rotor Blades of an Axial Turbine. Proceedings of ASME Turbo Expo, 2014, vol. GT2014, pp. 1-10.
- [26] KLADOVASILAKIS, N.; EFSTATHIADIS, T.; ASLANIDOU, I.; KALFAS, A. Rotor Blade Design of an Axial Turbine using Non-Ideal Gases with Low Real-Flow Effects. Energy Procedia, 2017, vol. 142, pp. 1127–1132.
- [27] MONTEIRO, Vinícius Guimarães ; ZAPAROLI, Edson Luiz ; de ANDRADE, Cláudia Regina de ; LIMA, Rosiane Cristina de. Numerical Simulation of Performance of an Axial Turbine First Stage. Journal of Aerospace Technology and Management, 2012, vol. 4, no. 2, pp. 254-263. DOI: 10.5028/jatm.2012.04025411.
- [28] Yahya, S. M. (n.d.). Turbines, Compressors, and Fans. In Chapter 1, Section 1.16, p. 17.
- [29] Yahya, S. M. (n.d.). Turbines, Compressors, and Fans. In Chapter 9, pp. 345–424.
- [30] Reggio, M., & Trépanier, J.-Y. (n.d.). Théorie des Turbomachines. Paris (France) : Dunod, chapter 3, pp. 52–109.
- [31] Cengel, Y. A., & Cimbala, J. M. (2017). Fluid Mechanics: Fundamentals and Applications (4th ed., Chap. 6, pp. 243–276). New York (USA): McGraw-Hill Education.
- [32] Salih, A. (2011). Conservation Equations of Fluid Dynamics. Department of Aerospace Engineering, Indian Institute of Space Science and Technology, Thiruvananthapuram, February 2011.

## REFERENCES

---

- [33] Wassgren, M. L. – Continuity\_03 – Control Volume Continuity Example [PDF]. West Lafayette (USA): Purdue University, School of Mechanical Engineering. 5 pages. Available online: [https://engineering.purdue.edu/~wassgren/teaching/ME30800/Examples/continuity\\_03.pdf](https://engineering.purdue.edu/~wassgren/teaching/ME30800/Examples/continuity_03.pdf) (accessed April 18, 2025, at 12:43 PM).
- [34] White, Frank M. (2009). Fluid Mechanics (7th ed., Chap. 4, pp. 229–290). New York (USA): McGraw-Hill Education.
- [35] Reggio, M., & Trépanier, J.-Y. (n.d.). Théorie des Turbomachines. Paris (France) : Dunod, chapter 4, pp. 114–144.
- [36] Boyce, M. P. (n.d.). Gas Turbine Engineering Handbook (2nd ed.). New York (USA): McGraw-Hill Education, Chap. 9, Axial Flow Turbines, pp. 337–369.
- [37] Dixon, S. L., & Hall, C. A. (2010). Velocity Triangles and Efficiencies. In Fluid Mechanics and Thermodynamics of Turbomachinery (6th ed., pp. 39–67). Butterworth-Heinemann.
- [38] Lennman, E. (2020). Aerodynamic Design in Axial Turbine for Heavy Duty Applications (Master's thesis, Faculty of Engineering, Lund University, Sweden), p. 17.
- [39] Smith, S. F. (1965). "A Simple Correlation of Turbine Efficiency." *Journal of the Royal Aeronautical Society*, 69, 467–470.
- [40] Reggio, M., & Trépanier, J.-Y. (n.d.). Théorie des Turbomachines. Paris (France) : Dunod, chapter 2, pp. 21–49.
- [41] Anderson, J. D. (2003). Modern Compressible Flow: With Historical Perspective (4th ed.). McGraw-Hill Education.
- [42] Atkins, P., & de Paula, J. (2010). Physical Chemistry (9th ed., pp. 19–44). Oxford University Press.
- [43] Dixon, S. L., & Hall, C. A. (2010). Velocity Triangles and Efficiencies. In Fluid Mechanics and Thermodynamics of Turbomachinery (6th ed., pp. 119–167). Butterworth-Heinemann.
- [44] Cengel, Y. A., & Boles, M. A. (2019). Thermodynamics: An engineering approach (9th ed., pp. 301–332). New York (USA): McGraw-Hill Education.

## REFERENCES

---

- [45] Richardson, L. F. (1922). *Weather Prediction by Numerical Process*. Cambridge University Press.
- [46] Von Kármán, T., & Taylor, G. I. (1937). Some Remarks on the Statistical Theory of Turbulence. *Proceedings of the 5th International Congress of Applied Mechanics*, Cambridge, MA.
- [47] Chapman, G. T., & Tobak, M. (1985). Observations, Theoretical Ideas, and Modeling of Turbulent Flows Past, Present and Future. In Dwyer et al. (Eds.), *Theoretical Approaches to Turbulence*. Springer-Verlag.
- [48] Hinze, J. O. (1975). *Turbulence* (2nd Ed.). New York (USA): McGraw-Hill Publishing Co.
- [49] Laminar-turbulent transition [Image]. (n.d.). In Wikipedia. Retrieved March 26, 2025, at 4:46 PM, from [https://en.m.wikipedia.org/wiki/File:Laminar-turbulent\\_transition.jpg](https://en.m.wikipedia.org/wiki/File:Laminar-turbulent_transition.jpg)
- [50] Pope, S. B. (2000). The statistical description of turbulent flows. In *Turbulent Flows* (pp. 34–82). Cambridge University Press.
- [51] Deep Learning is Non-Equilibrium Information Dynamics [Image]. (n.d.). In *Medium*. Retrieved April 2, 2025, at 4:55 PM, from <https://medium.com/intuitionmachine/deep-learning-is-non-equilibrium-information-dynamics-b00baa16b135>
- [52] Guerrero (n.d.). CFD Turbulence Overview [PowerPoint presentation]. Genève (Suisse): DÍcat, Université de Genève. Consulted on 26 March 2025 at 13:02, available at [http://www.dicat.unige.it/guerrero/aero\\_numerical\\_labs/part3/3\\_aero3\\_CFD\\_turbulence\\_overview.pdf](http://www.dicat.unige.it/guerrero/aero_numerical_labs/part3/3_aero3_CFD_turbulence_overview.pdf)
- [53] Hadane, A. Turbulence Modeling: Comparison and Best Practices for Accurate Results. [Online] Available at: <https://www.linkedin.com/pulse/turbulence-modeling-comparison-best-practices-accurate-asmaa-hadane>. Consulted on 27/03/2025 at 1:02 PM.
- [54] ANSYS Inc. (2025). Chapter 4: Turbulence. In *ANSYS Theory Guide* (pp. 41–158). ANSYS Inc.
- [55] Blazek, J. (2005). Chapter 7: [Turbulence Modelling]. In *Computational Fluid Dynamics: Principles and Applications* (pp. 227–258). Elsevier.

- [56] Hinze, J. O. (1975). Turbulence (2nd Ed.). New York (USA): McGraw-Hill Publishing Co.
- [57] Spalart, P., Allmaras, S. (1992). A one-equation turbulence model for aerodynamic flows. Rapport Technique AIAA-92-0439. États-Unis: American Institute of Aeronautics and Astronautics, 1992.
- [58] B. E. Launder and D. B. Spalding. (1972). Lectures in Mathematical Models of Turbulence. London (England): Academic Press, 1972.
- [59] Yakhot, V., Orszag, S.A., Thangam, S., Gatski, T.B. & Speziale, C.G. (1992), "Development of turbulence models for shear flows by a double expansion technique", Physics of Fluids A, Vol. 4, No. 7, pp1510-1520.
- [60] S. A. Orszag, V. Yakhot, W. S. Flannery, F. Boysan, D. Choudhury, J. Maruzewski, and B. Patel. "Renormalization Group Modeling and Turbulence Simulations". In International Conference on Near-Wall Turbulent Flows, Tempe, Arizona. 1993
- [61] T.-H. Shih, W. W. Liou, A. Shabbir, Z. Yang, and J. Zhu. "A New - Eddy-Viscosity Model for High Reynolds Number Turbulent Flows - Model Development and Validation". Computers Fluids. 24(3). 227–238. 1995
- [62] D. C. Wilcox. Turbulence Modeling for CFD. DCW Industries, Inc. La Canada, California. 1998.
- [63] D. C. Wilcox. "Formulation of the  $k-\omega$  turbulence model revisited". 45th AIAA Aerospace Sciences Meeting. Reno, NV, USA. AIAA Paper 2007–1408. 2007
- [64] F. R. Menter. "Two-Equation Eddy-Viscosity Turbulence Models for Engineering Applications". AIAA Journal. 32(8). 1598–1605. August 1994
- [65] F. R. Menter. "Review of the SST Turbulence Model Experience from an Industrial Perspective". International Journal of Computational Fluid Dynamics. Volume 23, Issue 4. 2009.
- [66] Ali A. H., Jaber A. S., Yaseen M. T., Rasheed M., Bazighifan O., Nofal T. A. 2022. A Comparison of Finite Difference and Finite Volume Methods with Numerical Simulations: Burgers Equation Model. **Complexity**, vol. 2022, Article ID 9367638, 9 p.

## REFERENCES

---

- [67] Tu, J., Yeoh, G.-H. & Liu, C. 2018. Chapter 5: CFD Techniques: The Basics. In Computational Fluid Dynamics, 3rd ed. Oxford (UK): Butterworth-Heinemann, pp. 155–210. ISBN: 9780081011270.
- [68] Tu, J., Yeoh, G.-H. & Liu, C. 2018. Chapter 4 - CFD Mesh Generation: A Practical Guideline. In Computational Fluid Dynamics, 3rd ed. Oxford (UK): Butterworth-Heinemann, pp. 125-154. ISBN: 9780081011270.
- [69] How to Build Mesh in Moldex3D Studio with User-Specified Structure [Image]. (n.d.). In Moldex3D. Retrieved May 11, 2025, at 8:56 AM, from <https://www.moldex3d.com/blog/tips-and-tricks/how-to-build-mesh-in-moldex3d-studio-with-user-specified-structure/>
- [70] All There Is to Know About Different Mesh Types in CFD [Image]. (n.d.). In ManchesterCFD. Retrieved May 11, 2025, at 9:25 AM, from <https://www.manchestercfd.co.uk/post/all-there-is-to-know-about-different-mesh-types-in-cfd>
- [71] Acosta, J. M. 2001. Numerical Algorithms for Three-Dimensional Computational Fluid Dynamic Problems. **Thesis**. Departamento de Máquinas i Motores Térmicos, E.T.S.E.I.T., Universidad Politécnica de Catalunya, Terrassa, pp. 9–16.
- [72] ANSYS CFX - Advanced CFD Simulation Software [Online]. (n.d.). In ANSYS. Retrieved May 11, 2025, at 10:05 AM, from <https://www.ansys.com/products/fluids/ansys-cfx#tab1-2>
- [73] ANSYS. 2025. ANSYS CFX-Solver Theory Guide R2025. Canonsburg (PA): ANSYS Inc., Chapter 11, pp. 369–388.
- [74] Spectral/Algebraic/Geometric Multigrid [Online]. (n.d.). In Maurice Fabien. Retrieved May 12, 2025, at 9:50 AM, from <http://www.mauricefabien.com/research/>
- [75] The Deep Learning Ecosystem Inspired by the Human Brain [Image]. (n.d.). In Medium. Retrieved May 14, 2025, at 11:28 AM, from <https://medium.com/@saleema2002shaik/the-deep-learning-ecosystem-inspired-by-the-human-brain-ea780126d88e>
- [76] Kalogirou, S. A. 2013. Neural Network Modeling of Energy Systems. In Reference Module in Earth Systems and Environmental Sciences. Oxford (UK): Elsevier. DOI: 10.1016/B978-0-12-409548-9.01563-3



## REFERENCES

---

- [77] Celik, I. B., Ghia, U., Roache, P. J., Freitas, C. J., Coleman, H., Raad, P. E., “Procedure for Estimation and Reporting of Uncertainty Due to Discretization in CFD Applications,” *Journal of Fluids Engineering*, Vol. 130, July 2008, 078001.
- [78] Ec\_a, L. and Hoekstra, M., “Evaluation of Numerical Error Estimation Based on Grid Refinement Studies with the Method of Manufactured Solutions,” *Computers and Fluids*, Vol. 38, 2009, pp. 1580–1591.
- [79] Airfoil Tools – Airfoil Database and Polar Viewer [Online]. (n.d.). In Airfoil Tools. Retrieved May 13, 2025, at 2:45 PM, from <http://airfoiltools.com>
- [80] ASME. (2009). *Standard for Verification and Validation in Computational Fluid Dynamics and Heat Transfer (ASME V&V 20-2009)*. American Society of Mechanical Engineers.
- [81] ALJARALLAH, A., TIFOOTI, M., ALQADI, I. Comparative Analysis of Turbulence Models for Trailing Edge Separation Over NACA 4412 Airfoil Using CFD Simulations and Experimental Study. *AIAA Regional Student Conferences*, 2023. DOI: 10.2514/6.2023-77057.
- [82] NASA. 2D NACA 4412 Airfoil Trailing Edge Separation – Validation Case. Langley Research Center, Turbulence Modeling Resource. Updated November 18, 2021. [https://turbmodels.larc.nasa.gov/naca4412sep\\_val.html](https://turbmodels.larc.nasa.gov/naca4412sep_val.html) . Accessed May 16, 2025, 5:06 PM.
- [83] COLES, D., WADCOCK, A. J. Flying-Hot-Wire Study of Flow Past an NACA 4412 Airfoil at Maximum Lift. *AIAA Journal*, 1979, vol. 17, no. 4, pp. 321–329. DOI: 10.2514/3.61127.
- [84] Messai, T. (n.d.). *Fluid Dynamics* [PowerPoint presentation]. Consulted March 15, 2025, at 6:03 PM.